Dijets and Photon Remnant Studies in Photoproduction with the ZEUS Detector at HERA

Changyi Zhou

Department of Physics
McGill University, Montreal
March 2005

A thesis submitted to McGill University in partial fulfilment of the requirements of the degree of Master of Science

Your file Votre référence
ISBN: 978-0-494-22781-7
Our file Notre référence
ISBN: 978-0-494-22781-7

Abstract

At the HERA particle accelerator, 27.5 GeV electrons collide with 920 GeV protons. In the photoproduction mode, the quasi-real exchange photon emitted by the electron interacts with the proton at small momentum transfer. Such events are selected and investigated with the ZEUS detector in the photon proton center-of-mass range 130 GeV $< W_{\gamma p} <$ 270 GeV using the 55.1 pb^{-1} gated luminosity of the year 2000 data. The two typical photoproduction processes are studied separately: in the direct case photons can interact directly with the proton, while in the resolved case the photon is resolved into its hadronic components. An inclusive data sample of two parton jet events with each a minimum transverse energy of 6 GeV and a third jet with a minimum transverse energy of 2 GeV are reconstructed and selected using the inclusive k_T clustering algorithm. The third jet travelling in the electron propagation direction can be assumed to be the photon remnant jet. Jet transverse energy density distributions, which are also known as 'jet shapes' are calculated on the jet sample. The photon remnant jets are found to be broader than the parton jets.

Résumé

À l'accélérateur de particules HERA, des électrons de 27.5 GeV entrent en collision avec des protons de 920 GeV. Dans le mode de photoproduction, le photon d'échange émis par l'électron est quasi-réel et interagit avec le proton à faibles valeurs de transfert de quantité de mouvement. De tels événements ont été choisis et étudiés par le détecteur ZEUS dans le domaine 130 GeV $< W_{\gamma p} <$ 270 GeV de l'énergie du centre de masse du système photon-proton, utilisant les 55.1 pb^{-1} de luminosité pris dans l'année 2000. Les deux processus typiques de photoproduction sont étudiés séparément: dans le cas direct le photon interagit directement avec le proton, alors que dans le cas résolu le photon interagit en termes de ses composantes hadroniques. Un échantillon inclusif d'événements à deux jets partoniques avec chacun une énergie transversale minimum de 6 GeV, et une troisième jet avec une énergie transversale minimum de 2 GeV sont reconstruits et choisis en utilisant l'algorithme de jet par regroupement inclusif k_T des particules. Le troisième jet se déplaçant dans la direction de l'électron peut être considéré comme le jet des restes du photon. Les distributions de densité d'énergie transversale des jets, aussi connues sous le nom de 'formes des jets', sont calculee pour notre échantillon. Les jets des restes du photon s'avèrent être plus larges que les jets partoniques.

Contents

Chapter 1

Introduction

1.1 Motivation

At the HERA (Hadron Elektron Ring Anlage) accelerating ring, electrons[1] collide with protons. The full range momentum transfer from high to low can be classified as deep inelastic scattering (DIS) and photoproduction processes respectively. In DIS processes the electron is scattered at large momentum transfer. While in photoproduction process, the quasi-real photon emitted from the incoming electron interacts with the partons in the incoming proton at low momentum transfer rate. Right after the fragmentation of the partons, jets are formed from the hadronisation process. Jets are reconstructed in a clustering algorithm scheme by grouping up related particles travelling in almost the same kinematic direction. The jet internal transverse energy density, which is also called jet shape, can be calculated to reveal the jet internal structure. In photoproduction, mainly two types of jet production processes dominate when no secondary productions are considered: the direct process, in which the photon interacts directly with the parton (quark or gluon) in the proton, resulting into at least two jets; and the resolved process, where the photon fluctuates into a quark-antiquark pair, which then scatter with the partons in the proton, resulting into two high transverse energy parton initiated jets, and a low transverse energy photon remnant jet. The studies of photoproduction direct and resolved processes can be a good test of jet theories. Especially, interesting studies can be performed on

[1]Throughout this thesis, "electron" refers to both electrons and positrons.

the photon remnant jet, which mainly includes the isolation and identification of the photon remnant jet out of the two quark or gluon jets and the background jets. The jet shape studies on the reconstructed jets can give us more ideas on different internal particle energy distributions between quark or gluon jets and photon remnant jets. Those characteristic difference can help better separate the direct and the resolved photoproduction processes.

The collision interactions are carefully measured by the ZEUS detector, which is located at the HERA ring. The ZEUS detector measures the trajectory and energy of the particles, with as high resolution as possible. With the help of computer simulations of the detector, these jet studies can let us better understand the detector, its acceptance and efficiency for different physics processes.

1.2 Thesis Overview

To illustrate the principles behind this analysis, the basic theory, concepts, and variables will be introduced first in chapter 2, followed by the high energy physics experiment set-up introduction in chapter 3. How data is collected, processed and stored will be described in chapter 4. Chapter 5 presents how the event selection is carried out to select multi-jet events, keeping the photon remnant jet candidates. The Monte Carlo simulation concepts and energy corrections will be carefully described. Then the emphasis will be laid on the data analysis, more specifically on two or more jet studies, and our main topic, the photon remnant jet studies, with results on multi-jet events selection, jets selection, energy distribution, and the jet shape structure. The thesis will end with conclusion, acknowledgement, glossary and bibliography.

Chapter 2

Theory and Kinematics Overview

There are four types of forces in nature, known as gravitational, electromagnetic, weak and strong forces. High-energy physics, the study of the smallest components of matter, mainly involves three of them, the electromagnetic force, characterized by the photon (γ) as mediator, the weak force, with $W^{\pm}$ and Z bosons as mediators and the strong force, with gluons as force mediator.

2.1 Quantum Electrodynamics

Believed to be the most successful and accurate theory in physics, Quantum Electrodynamics (QED) describes the interaction of photons and charged fermions. The electromagnetic weak coupling constant is α_{em}. QED makes possible to use quantum field theory to obtain predictions on electromagnetic interactions, which is described by charged particle quantum field, and the electromagnetic (or photon) field.

The later developed Quantum Chromodynamics (QCD) describes the strong force. QED and QCD are quite similar on many points, but QED has positive and negative electric charges, while QCD, has color charges: red, green and blue.

2.2 Quantum Chromodynamics

QCD, a non-abelian gauge theory, describes the interaction of quarks, which only exist in red, blue or green colors, via the exchange of one of eight massless gluons. It explains the logarithmic dependence of the structure function F_2 on Q^2 and non-zero longitudinal structure function [6]. As the gluons also have color, interactions between gluons themselves are also possible. All these interactions are characterized by the strong coupling constant α_s [12].

2.2.1 Perturbative QCD

The calculations of QED and QCD are carried out by using perturbation theory [1]. The first step is to break the problem into an infinite sum of terms as matrix elements, which can be solved accurately, then group the terms together according to the increasing powers of α_s or α_{em} [11]. In the electromagnetic interaction, the coupling constant $\alpha_{em} = 1/137$. So the first order terms with the lowest powers of α_s or α_{em} tend to be the largest, and are thus called leading-order calculation. The next significant terms are known as Next-to-Leading-Order (NLO). Other higher order terms can be also carried out, according to the precision requirements in the analysis, and the limited CPU calculation power.

2.2.2 Non-perturbative QCD

When the higher order emissions in QCD are taken into calculation, the perturbative approaches are no longer suitable with higher α_s values. Non-perturbative methods are then used instead mainly with phenomenological hadronization models (e.g. the cluster model [4] and the string fragmentation model [5]), to convert the final state partons into hadrons.

2.3 QCD Analyses in ZEUS

In ZEUS, detailed dynamics of QCD and the hadronic properties of the virtual photon are studied in a wide Q^2 range. Analysis topics on jets, particle production and event shape are carried out. Especially the jet cross section measurements, rapidity studies, prompt photon studies, precise determination of α_s, the searching for pentaquarks can be very useful and interesting. They are good examples of QCD studies.

2.4 Kinematical Variables

First some most commonly used kinematical variables to describe the *ep* scattering processes are introduced as follows:

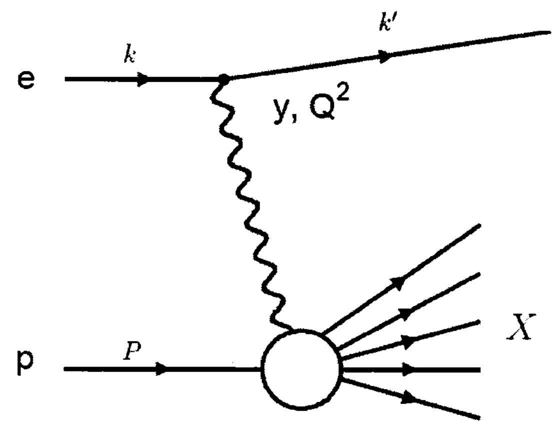

Figure 2.1: Electron-Proton Scattering

Just as it is shown in figure 2.1, an incoming electron with a momentum of k, collides with an incoming proton with a momentum P. The electron is scattered at an angle of θ_e with respect to the proton beam direction.

The negative squared four-momentum transfer Q^2, also known as the virtuality of the exchanged photon, is defined as the difference of the four-momenta of the incoming (k) and outgoing electron (k'):

$$Q^2 = -q^2 = -(k - k')^2 > 0 \tag{2.1}$$

The quantities k and k' are given by:

$$k = (E_e, 0, 0, -E_e) \tag{2.2}$$

and

$$k' = (E'_e, 0, E'_e \sin\theta_e, E'_e \cos\theta_e) \tag{2.3}$$

where E_e and E'_e are the energy of the incoming and scattered electron, respectively.

To describe the fractional energy transfer from electron to proton in the rest frame of the proton and the fractional momentum of the proton carried by the scattering particles, the two most commonly used variables y and x are used.

They are generally given in the rest frame of the proton by:

$$y = \frac{p \cdot q}{p \cdot k}. \tag{2.4}$$

and the Bjorken scaling variable x:

$$x = \frac{Q^2}{2Pq} \tag{2.5}$$

The relationship between Q^2, x and y is generally given by:

$$Q^2 = x \cdot y \cdot s \tag{2.6}$$

The s is the square of the electron proton center of mass energy, which is given by:

$$s = (k + P)^2 \approx 4 \cdot E_e \cdot E_p = 101,200\ GeV^2 \tag{2.7}$$

$$\sqrt{s} \approx 318\ GeV \tag{2.8}$$

where in this analysis $E_e = 27.5$ GeV and $E_p = 920$ GeV.

There are at least three approaches to calculate Q^2 and the kinematic variables. They are the electron method, the hadronic method and the double angle method, described below. Q^2 is an important variable in DIS analysis. But Q^2 is not really an interesting variable for photoproduction analysis, as Q^2 is equal to zero (or very low) by definition. In photoproduction process, the scattered electrons are lost in the beam pipe, and thus not detected. So the electron and double angle method cannot be used. Even the Q^2 calculated from the Jacquet-Blondel hadronic method is not well described for photoproduction either, due to the sizable loss of hadrons down the beam pipe. Instead, the photon proton center of mass energy W is used more to describe photoproduction.

2.4.1 The Electron Method

The first method is the so-called electron method, which only relies on the precise measurement of the scattered electron. In this method, one gets for Q^2:

$$Q_e^2 = 4E_eE_e'\cos^2\frac{\theta_e}{2} = 2E_eE_e'(1+\cos\theta_e) \tag{2.9}$$

It can easily be seen that the Q^2 is directly calculated from equation 2.1, 2.2 and 2.3, provided that the momentum of the scattered electron can be precisely measured.

Correspondingly, the inelasticity y_e and the Bjorken scaling variable x_e are given by:

$$y_e = 1 - \frac{E_e'}{2E_e}(1-\cos\theta_e) \tag{2.10}$$

$$x_e = \frac{E_e'(1+\cos\theta_e)}{2E_py_e} \tag{2.11}$$

The electron method is a very useful method for DIS analysis, but it is also useful in photoproduction analysis, as one can use this method to reject DIS events to preserve photoproduction event.

2.4.2 The Hadronic Method

The second method is the so-called hadron method, also known as the Jacquet-Blondel [44] method. Q^2 is extracted from the hadronic final state, and no scattered electron information is needed, which is a great advantage in photoproduction or CC DIS[1] analysis, where scattered electron is mostly lost in the beam pipe or there is no electron.

[1]CC DIS will be introduced in section 2.6.2

In the hadronic final state, the transverse momentum $P_{T,h}$, the variable Σ, and the inclusive hadron angle γ_h are defined as:

$$P_{T,h} = \sqrt{(\sum P_{x,i})^2 + (\sum P_{y,i})^2} \tag{2.12}$$

where $P_{x,i}$ and $P_{y,i}$ are the transversal components of the ith particle momentum.

$$\Sigma = \sum (E_i - P_{z,i}) \tag{2.13}$$

where E_i and $P_{z,i}$ are the energy and longitudinal momentum component of particle i, respectively.

The inelasticity y is given by:

$$y_{JB} = \frac{\Sigma}{2E_e} \tag{2.14}$$

$$\tan\frac{\gamma_h}{2} = \frac{\Sigma}{P_{T,h}} \tag{2.15}$$

Thus, the Q^2 and the x_{JB} can be calculated by:

$$Q^2_{JB} = \frac{P^2_{T,h}}{1 - (\frac{\Sigma}{2E_e})} = \frac{(\sum P_x)^2 + (\sum P_y)^2}{1 - y_{JB}} \tag{2.16}$$

$$x_{JB} = \frac{Q^2_{JB}}{s \cdot y_{JB}} \tag{2.17}$$

The photon proton center of mass energy is given by:

$$W_{\gamma p} = \sqrt{4E_\gamma E_p} = \sqrt{s \cdot y_{JB}} \tag{2.18}$$

and W is an important variable to evaluate the momentum transfer from the electron to the photon, in another word, how real this emitted photon is. So this variable can be used to select photoproduction processes.

2.4.3 The Double-Angle-method

The fourth method is the Double-Angle-method, which is very useful in medium to high Q^2 NC DIS events[2], as only the angles of the electron and the hadronic final

[2]This will be introduced in section 2.6.2

states are used [6].

The Q^2, y and x are given by:

$$Q^2_{DA} = \frac{4E_e^2 \sin\gamma_h (1+\cos\theta_e)}{\sin\gamma_h + \sin\theta_e - \sin(\gamma_h + \theta_e)} \tag{2.19}$$

$$y_{DA} = \frac{\sin\theta_e \cdot (1-\cos\gamma_h)}{\sin\gamma_h + \sin\theta_e - \sin(\theta_e + \gamma_h)} \tag{2.20}$$

$$x_{DA} = \frac{Q^2}{s \cdot y_{DA}} \tag{2.21}$$

The advantage of this method is that the scattered electron energy is not required in the calculation, which makes this method more energy scale independent. But it is not used in this analysis as it is irrelevant for photoproduction.

2.5 Analysis Frame

The choice of different coordinating frame set-ups used in the analysis is very important. The analysis frame serves as the 'base' on which all the kinematic variables are measured, constructed and compared. To meet various analysis purposes, for example photoproduction and DIS analyses, different frames can be used to achieve better resolution and performance. But meanwhile, the definitions of the frames should also be standard, especially for those frame dependent variables, so that comparisons between analysis results from different persons or in different experiment can be possible.

2.5.1 Laboratory Frame

The laboratory frame is the most widely used analysis frame, and is set up as the following:

The ZEUS coordinate system is a right-handed Cartesian system, with the coordinate origin at the *ep* interaction point (IP), the Z axis pointing in the proton beam direction, also referred to as the "forward direction", the X axis pointing left towards the center of the HERA ring, and the Y axis pointing vertically upward.

The polar angle with respect to the Z-axis is defined as θ, in the range of $0° \leq \theta \leq 180°$. Particles with $\theta \approx 0°$ *or* $180°$ are totally lost in the beam pipe in the laboratory frame, as they are travelling right in the direction of the proton beam or the electron beam.

The pseudorapidity η is defined as $\eta = -\ln(\tan\frac{\theta}{2})$, in the range of $-\infty < \eta < +\infty$. This transfer from the polar angle θ, which is dependent on the frame setup, to the pseudorapidity makes the direction relations longitudinal Z-boost independent. In fact, the pseudorapidity comes from a theoretical variable, which is called rapidity y[3]. The rapidity of a particle with energy E and momentum p with respect to a vector r is given by:

$$y_r = \frac{1}{2}\ln(\frac{E+p_r}{E-p_r}) \tag{2.22}$$

where p_r is the momentum component in the r direction.

In the experimental case, the rapidity with respect to the longitudinal axis (r is the beam direction) is calculated with the θ by formula 2.23, given that $p_r = p\cos\theta$.

$$y_r = \frac{1}{2}\ln(\frac{E+p\cos\theta}{E-p\cos\theta}) \tag{2.23}$$

Taking the particles to be massless, E is equal to p. So the pseudorapidity is given by:

$$\eta = \frac{1}{2}\ln(\frac{1+\cos\theta}{1-\cos\theta}) = -\ln(\tan(\frac{\theta}{2})) \tag{2.24}$$

Another useful variable is the azimuthal angle ϕ, defined as the angle with respect to the X-axis in the X-Y plane, in the range of $0 \leq \phi < 2\pi$.

[3]Rapidity is also symbolized with letter 'y', but is different from inelasticity.

2.5.2 Breit Frame

At HERA, due to the overwhelming ratio of the proton beam energy to the electron beam energy, the hadronic final state particles are not easily identified among the proton remnant. So another reference frame is created, the Breit frame [11]. The coordinates in the Breit frame moves with the center of mass of the quark from the proton and the electron, so that the incoming quark momentum is $Q/2$, the outgoing quark momentum is $-Q/2$, and the proton remnant momentum is $\frac{(1-x)Q}{2x}$. The Breit frame can help better identify hadronic final state particle showers, and to distinguish the struck quark and the proton remnant.

Lorentz boost methods are used to transform the kinematics from the laboratory frame to the Breit frame [15].

The key factor to a successful boost to the Breit frame is a good measurement of the scattered electron. So the Breit frame turns to be more useful in DIS analysis, not in photoproduction processes, where the scattered electron is lost in the beam pipe and thus likely not well measured. In this analysis, the laboratory frame is used instead of the Breit frame due to those reasons.

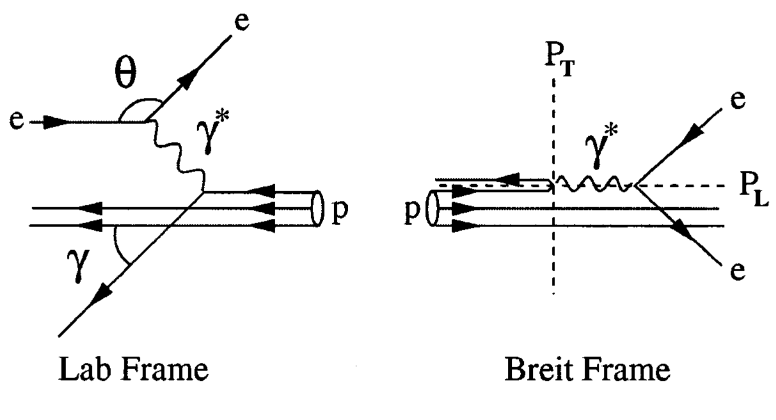

Figure 2.2: Lab and Breit Frame Diagrams

Figure 2.2 illustrates the basic diagrams of gamma-proton scattering in both the laboratory frame and the Breit frames.

2.6 Physics Processes

2.6.1 Photoproduction

HERA is a very good place to study photoproduction processes in ep collision. For low Q^2 values, the electron-proton scattering can be viewed as the emission of a quasi-real photon from the electron interacting with the proton. This kinematic domain of the photon-proton scattering is usually referred to as photoproduction [19], also can be described as the production of hadrons by the inelastic scattering of real photons on a nucleon target. The ep collision cross section via virtual photon exchange is proportional to $(\frac{1}{Q^2})^2$. The photoproduction event is characterized by very low Q^2 values ($Q^2 < 1$ GeV^2) [10]. The electron scatters at very small angles, when Q^2 is quite small. The photoproduction events actually dominate among all types of interactions in rate.

The Photon Flux

In the $ep \to eX$ process, as shown in the figure 2.1, the hadronic cross section σ_{ep}, can be calculated from the photon-proton scattering cross-section, $\sigma_{\gamma p}$, by

$$\sigma_{ep\to eX} = \int dy f_{\gamma,e}(y)\sigma_{\gamma p}(y). \tag{2.25}$$

The photon flux [20] out of the electron is calculated in the Weizsäcker-Williams approximation [43, 45]:

$$f_{\gamma,e}(y) = \frac{\alpha}{2\pi}\left(\frac{1+(1-y)^2}{y}\log\frac{Q^2(1-y)}{m_e^2y^2} + 2m_e^2y\left(\frac{1}{Q^2} - \frac{1-y}{m_e^2y^2}\right)\right) \tag{2.26}$$

in which Q^2 is the photon virtuality, E_e is the incoming electron energy, E'_e is the scattered electron energy, and θ_e is the scattering angle. (One can refer to the variable definitions in section 2.4)

Direct and Resolved Processes

In LO QCD scattering (shown in figure 2.3) between a photon and a proton, two different types of processes could occur, namely the direct and the resolved processes. The photon may interact directly with a quark or gluon from the proton in the direct

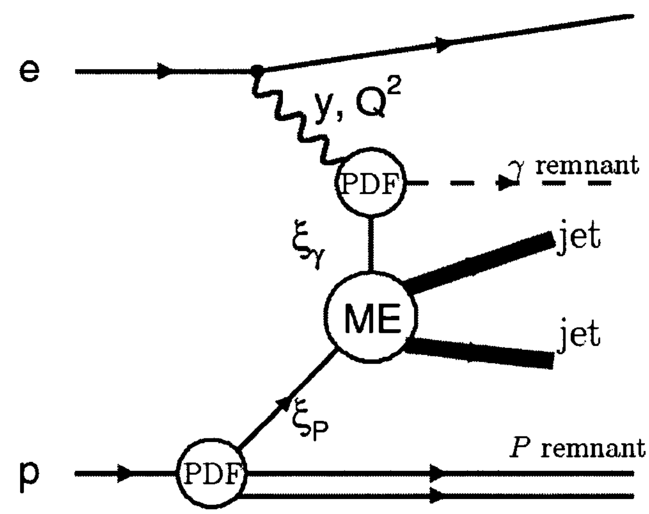

Figure 2.3: The diagram illustrates a leading order jet production in electron proton scattering interaction. Generally the PDF refers to the Parton Density Function. The PDF above in the diagram refers to the quark-antiquark pair, fluctuated from the photon. The PDF below addresses the quarks and gluons in the proton. ξ_γ and ξ_P are the longitudinal scaled parton momenta of the photon and the proton, and ME are the Matrix Elements.

process, or resolve into its constituent quarks and gluons which then interact with a parton from the proton in the resolved process. [21]

For a direct process, it is easy to understand that after the photon directly interacts with quark or gluon in the proton, which can be illustrated as $\gamma q \Rightarrow qg$ and $\gamma g \Rightarrow qq$, two outgoing jets will be observed.

The resolved process is especially interesting. The high energy photon fluctuates into a quark-antiquark pair, and then one of the photon-originating partons interacts with a parton from the proton, resulting in two high transverse energy parton jets, together with the photon remnant. This photon remnant is actually the part of the fluctuated partons that does not interact with the proton partons, carrying the remaining photon momentum. So the difference between the resolved and the direct processes is that only a fraction of the original photon's momentum is involved in the collision in resolved process. This fraction is given a variable named x_γ, which will be carefully introduced in section 2.7.1. For direct process $x_\gamma = 1.0$, while for resolved process, $x_\gamma < 1.0$ [18].

Figure 2.4 illustrates direct and resolved processes in photoproduction in leading order.

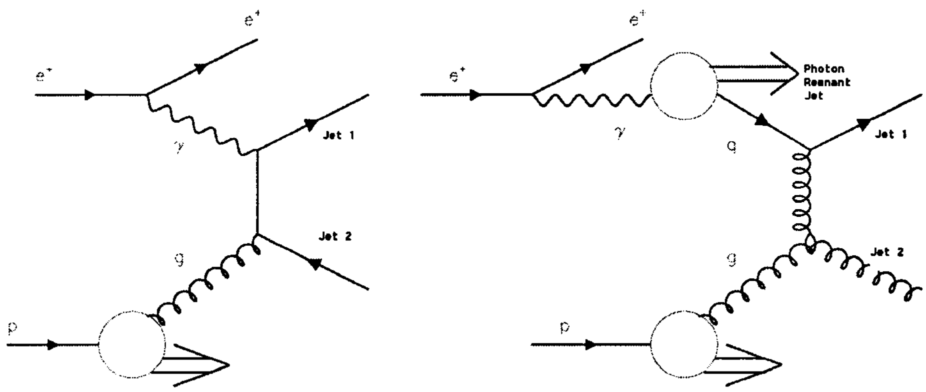

Figure 2.4: Direct (left) and resolved process (right) diagrams in LO photoproduction

2.6.2 Deep Inelastic Scattering

Deep Inelastic Scattering (DIS) [7] is a very interesting branch of studies in high energy physics, which is characterized by high momentum transfers.

An inelastic reaction is caused when a high energetic electron is scattered with large momentum transfer, in which the nucleon will break up, followed by large amount of strongly interacting particles produced as hadronic final states, the photons, electrons, neutrinos, muons, and other secondary decay products.

In DIS processes, the interaction between the incoming lepton, which is the electron or the positron in the case of HERA, and the proton, is mediated by gauge bosons.

When the exchanged boson is a neutral particle, i.e. photon or the neutral vector boson Z^0, and the final state is a scattered electron and other hadronic final state particles, this process is noted as neutral current (NC) DIS.

When the exchanged boson is a charged boson, i.e. $W^{\pm}$, and the outgoing lepton is a neutrino or an anti-neutrino and other final state particles, this process is referred to as charged current (CC) DIS. [16]

The Feynman diagram to illustrate the NC and CC is shown in figure 2.5.

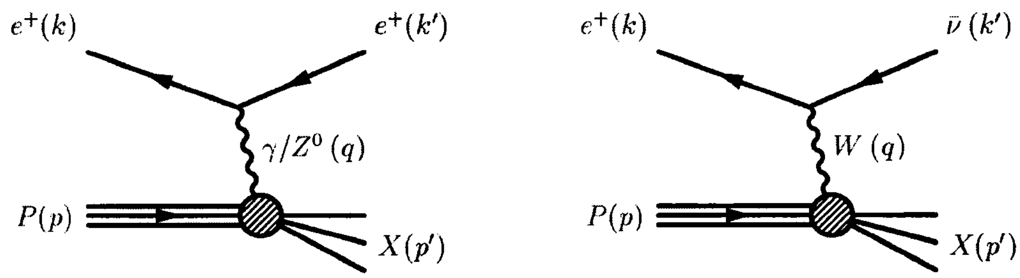

Figure 2.5: The Feynman diagrams to illustrate neutral (left) and charged (right) current DIS interactions in proton positron scattering.

2.7 Jet Descriptions in Photoproduction

In hard scattering processes, partons interact via a quark or gluon propagator, resulting in jet production. According to color confinement, the final state has to be color singlet. Single quarks or gluons cannot exist by themselves. They radiate other partons, which is called fragmentation process, and finally form a color-singlet jet states, with the outgoing particles gathering around the direction of propagation of the parton to form a flowing jet. This formation of particles is called hadronization process. Jets allow the study of short distance aspects of QCD, e.g. color dynamics, the strong coupling constant, and the reconstruction of heavy particles [13]. It should be noted that the transverse energy considered in this hadronization process is basically above 300 MeV [8], and this is because that 300 MeV is approximately the noise level in the calorimeter, which means that energies below 300 MeV is hard to be detected. The range between 300 MeV to several GeV is called soft scattering process, and when it comes to several GeV, it is called hard scattering process.

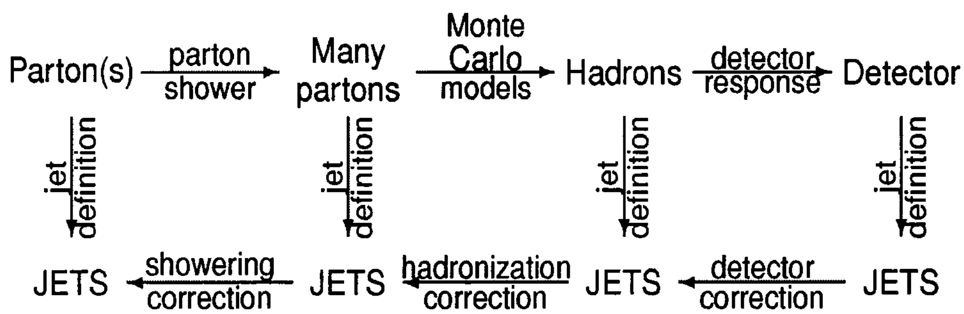

Figure 2.6: A typical schematic diagram of jet analysis.

A basic jet analysis schematic diagram is illustrated in figure 2.6[4]. Each jet definition is a jet reconstruction process, which will be introduced below.

2.7.1 x_γ

In leading order QCD calculation, the x_γ [17] variable is involved to parameterize direct photoproduction process and resolved photoproduction process by calculating the fraction of the photon energy in the hard scattering.

$$x_\gamma^{LO} = \frac{E_{T1}^{parton} e^{-\eta_1^{parton}} + E_{T2}^{parton} e^{-\eta_2^{parton}}}{2yE_e} \tag{2.27}$$

Since partons cannot be measured directly, the jets observed in the detector are used for the x_γ calculation, in an analogous way. [3]

$$x_\gamma^{obs} = \frac{E_{T1}^{jet} e^{-\eta_1^{jet}} + E_{T2}^{jet} e^{-\eta_2^{jet}}}{2yE_e} \tag{2.28}$$

At leading order, x_γ will be equal to one for direct processes, and less than one for resolved processes. But when x_γ goes to low values close to one, smearing effects will

[4]The Monte Carlo model simulation will be introduced in chapter 6.

be more obvious due to higher order processes effects.

Similarly to the above, the fractional energy of proton involved in interaction can be given by:

$$x_p^{LO} = \frac{E_{T1}^{parton} e^{\eta_1^{parton}} + E_{T2}^{parton} e^{\eta_2^{parton}}}{2E_p} \tag{2.29}$$

$$x_p^{obs} = \frac{E_{T1}^{jet} e^{\eta_1^{jet}} + E_{T2}^{jet} e^{\eta_2^{jet}}}{2E_p} \tag{2.30}$$

The x_γ^{obs} and x_p^{obs} can refer to the ξ_r and ξ_p in figure 2.3.

2.7.2 Jet Algorithms

In this ZEUS jet analysis, two distinct types of jet finding algorithms are used.

CONE Algorithm

Each calorimeter cell with $E_T > 300$ MeV is taken as seed, then seeds that satisfy $R = \sqrt{(\Delta\eta)^2 + (\Delta\phi)^2} \leq 1$ unit are combined together as groups. The pre-clusters are formed by sliding a 3 cells by 3 cells scanning 'window', over the $\eta - \phi$ space, and each window with a minimum transverse energy is noted as a pre-cluster. The axis of the pre-cluster (pseudorapidity and azimuthal angle of the jet) is defined by Snowmass convention[5], i.e. $\eta^{pre-cluster}$ and $\phi^{pre-cluster}$ are the E_T weighted mean pseudorapidity and azimuth of all seeds in the pre-clusters. Then within a cone (R=1) around each pre-cluster, all calorimeter cells in that cone are combined to form clusters, i.e. all other calorimeter cells which are within this cone radius are added into this jet, as long as it satisfies:

$$\triangle R_i = \sqrt{(\eta_i - \eta_{pre-cluster})^2 + (\phi_i - \phi_{pre-cluster})^2} < R\ (= 1) \tag{2.31}$$

k_T Algorithm

This analysis uses the inclusive k_T algorithm, which is believed to be one of the algorithms best suited to minimize hadronization effects [6], to overcome the jet

[5] The Snowmass convention will be introduced in section 2.7.3 below.

overlapping problem in the CONE algorithm. Therefore the k_T algorithm is the most extended algorithm in HERA jet analysis, and used in this analysis also.

To reconstruct the jet, basic steps are performed as follows:

The first step is to calculate the closeness between every pair of particles (d_{ij}), and the closeness for each particle (d_i):

$$d_{ij} = min(E_T^i, E_T^j)^2 \cdot (\Delta\eta_{ij}^2 + \Delta\phi_{ij}^2) \tag{2.32}$$

$$d_i = E_T^i \cdot R^2 \tag{2.33}$$

where E_T^i, and E_T^j are the transverse energy of each particle, and $\Delta\eta_{ij}$ and $\Delta\phi_{ij}$ are the pseudorapidity and azimuthal angle distance between particles in a pair.

The same parameter R acts as a jet radius parameter in the $\eta - \phi$ plane, and is usually set to one unit as preferred value [13].

Then all pair elements $\{d_{ij}, d_i\}$ are compared. If the smallest is one of the d_{ij}, then the two particles i and j are merged into a new one. Otherwise if the smallest is one of the d_i, then the cluster is regarded as a finished jet. The above procedure is repeated until all particles have been assigned to a jet and no more is left out. [2]

The major difference between the two algorithms lies in how each particle is assigned to a particular jet [23]. The k_T algorithm gives more attention to the jet core, and the cone algorithm may take in too many soft gluons at the edges. [13, 14]

2.7.3 Snowmass Conventions

To build up a jet, some questions need to be answered, such as how particles can be grouped into one jet, and how the jet kinematic variables are calculated from particle kinematic variables. The formation of a jet should be done in a universal way so that world wide jet analysis results can be compared under a standard scheme. So came the Snowmass convention into being [22].

The transverse energy of the jet E_T^{jet} is calculated by combining all the particles inside this jet with their transverse energy E_T^i, where 'n' is the total number of particles inside the jet:

$$E_T^{jet} = \sum_i^n E_T^i \tag{2.34}$$

The pseudorapidity of the jet η^{jet} and the azimuthal angle ϕ^{jet} are correspondingly the sum of all particles inside the jet weighted with their *transverse energy* E_T^i.

$$\eta^{jet} = \frac{\sum_i \eta^i E_T^i}{\sum_i E_T^i} \tag{2.35}$$

$$\phi^{jet} = \frac{\sum_i \phi^i E_T^i}{\sum_i E_T^i} \tag{2.36}$$

2.7.4 Jet Shape ψ

Another important jet variable in this analysis is the jet 'shape' variable $\psi(r)$ [17]. When particles are correlated together to form jets in the inclusive k_T clustering algorithm, which has been discussed above, one unit of radius parameter R is defined for jet finding. After the jet finding is completed, the information about which particle belongs to which jet will be known, so different radii concentric to the axis of the jet are used to form 'cone's in the $\eta - \phi$ plane, and those particles inside this stepping 'cone' are summed up with their transverse energy. Then the ratio of this sum to the total transverse energy of this jet is called ψ:

$$\psi(r) = \frac{1}{E_T^{jet}} \sum_i^n E_T^i(r) \tag{2.37}$$

where ψ is summed over all particles inside a given 'cone' r.

In fact, ψ samples the transverse energy density distribution inside the jet and it is therefore used here to describe the E_T distribution inside this jet is concentrated around the axis or more evenly distributed by telling the jet is narrow or broad.

Since for any analysis, a single event cannot reveal much, a sufficient numbers of jets should be statistically studied. In such case, the mean integrated jet shape is defined as the averaged fraction of the jet transverse energy distribution by:

$$\langle\psi(r)\rangle = \frac{1}{N_{jet}} \sum_{j}^{N_{jet}} \psi_j(r) \tag{2.38}$$

2.8 Photon Remnant Jet

Insight study of the photon structure is a very interesting topic. The photon, up to now understood as a truly elementary particle, were not expected to have any internal or extended physical size.

The photon can however couple to charged particles like quarks and their corresponding antiquarks, and the life-time of this quark-antiquark pair is determined by the well-known Heisenberg uncertainty principle:

$$\triangle t \leq \frac{h}{\triangle E} \tag{2.39}$$

where $\triangle E$ is the energy difference of the incoming photon and the quark-antiquark pair.

In the photoproduction direct processes, the quasi-real photon emitted from the electron participates entirely in the scattering processes with the partons from the incoming proton, resulting in essentially two jets. But in the resolved process, the quasi-real photon fluctuates into a quark-antiquark pair. Then one parton from this quark-antiquark pair interacts with the parton from the incoming proton, while the other one fragments into a photon remnant jet which would be expected to be going in the original photon direction. This means that in the resolved processes, only a fraction of the momentum of the photon is involved and the remaining momentum is carried by the spectator partons. The photon may be regarded as a source of partons to interact with the partons in the incoming proton. Above all, the presence of the photon remnant jet can be used in the identification of the resolved process. [10].

The properties of the photon remnant jet can reveal the structure of the quasi-real photon. In another word, the photon is being probed by partons from the proton.

Chapter 3

Experimental Setup

3.1 HERA

The HERA collider (Hadron Electron Ring Anlage) is located in the suburb area of West Hamburg, in Germany. Proton and electron beams are accelerated in the 6.3 km HERA ring, stored, and used simultaneously by four major different experiments: ZEUS, H1, HERA-B (experiment terminated already) and HERMES.

In ZEUS and H1, 920 GeV[1] proton beams and 27.5 GeV electron beams are made to collide head on, since year 1998, with a center of mass energy of 318 GeV. HERA-B used only the proton beam to aim at B-system CP-violation studies while HERMES uses only the polarized lepton beam, to perform beam-target experiments to study the spin properties of the nucleons.

The HERA ring tunnel is located 10 - 25 m under ground with magnets to constraint and guide the proton and electron beams. The beams are stored in two separate storage rings, with the proton beam above. For the electron ring, normal conductors at room temperature are used to bend the electrons. For the proton storage ring, due to the proton's high momentum and its mass, 4.7 Tesla magnets are required to bend the proton beam momentum. Therefore, superconducting magnets are used at a temperature of $4.4°K$, which is equal to $-269°C$.

[1]The units of momentum, GeV/c, are abbreviated as GeV throughout this thesis.

It should be noted here that positrons were more preferred beam particles for collision, mainly due to the positively-charged dust in the pipe, which would neutralize with the negative charged electrons. So electron beam lifetime was observed to be much shorter than for positron. But since 1998, with the improvement of vacuum conditions, electrons are also used for collision.

Figure 3.1 shows the scheme of the HERA ring and the pre-accelerators.

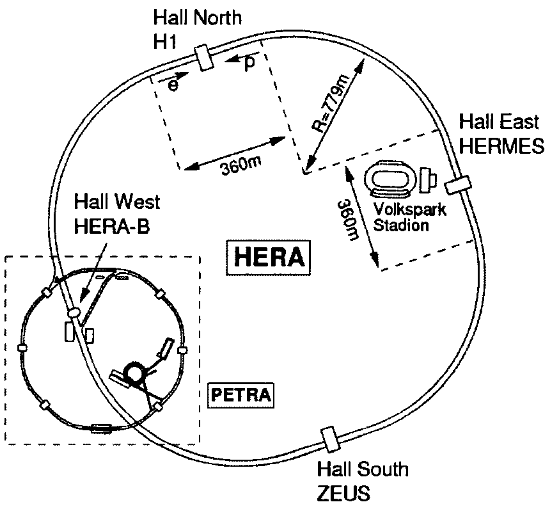

Figure 3.1: The electron-proton collider HERA (left) and the pre-accelerators (right).

The protons are created with the negative hydrogen ions (H^-) from the 50 MeV LINAC. Then the proton beams are injected into the synchrotron DESY III for further acceleration to 7.5 GeV, and injected into the Positron Electron Tandem Ring Accelerator (PETRA). After the acceleration in PETRA, the energy will reach 14 GeV and the proton beams are injected into the HERA ring.

Electron or positrons are started in electron generators, and directly injected into the LINAC I and LINAC II, which are linear pre-accelerators and accelerate the electron beam with relatively lower momentum from 220 MeV (for electrons) and 450 MeV (for positrons). Then the leptons are injected into the DESY II synchrotron and accelerated to 7.5 GeV. After that, the leptons go into the PETRA and HERA ring.

This PETRA ring also provides synchrotron radiation source light for biology experiment, such as European Molecular Biology Laboratory (EMBL).

Leptons predominantly align their spins in the vertical direction, as lepton beams are transversely polarized by the Sokolov-Ternov effect [32] through the emission of synchrotron radiation. But in order to study helicity structure of the nucleon, a longitudinally polarized beam (spin aligned parallel to the beam direction) is required, thus three pairs of Spin Rotators have been installed in front and behind the ZEUS, H1 and HERMES experiments.

The particle beams in the HERA ring consist of particle bunches which are separated by 96 ns. A maximum of 210 bunches can be stored at the same time in the HERA ring. Most of the proton and electron bunches are paired for collision, while some of them are not paired and kept for background studies. The proton electron bunch structure in HERA is shown in figure 3.2.

3.2 Physics of ZEUS

The electron being so tiny, it can act as a probe to explore the inner structure of hadrons. After the collision, the positions, the momenta, the energies of the hadronic final state particles, the jets that are formed by those particles, and the scattered electron should be measured with the highest possible precision and speed. The goal of the ZEUS detector is to meet those requirements, and also to meet the requirements from a variety of physics processes that are studied in high energy physic [33]. For example, to have accurate momenta information, i.e. the outgoing trajectories (direction) of the particles and their absolute momenta, the particles tracks which are very close to each other should be distinguishable. Both low and high momentum particles should be measurable with high resolution. In addition to particle tracks, energies should be measured which can mostly reflect the 'true' values. Both hadronic

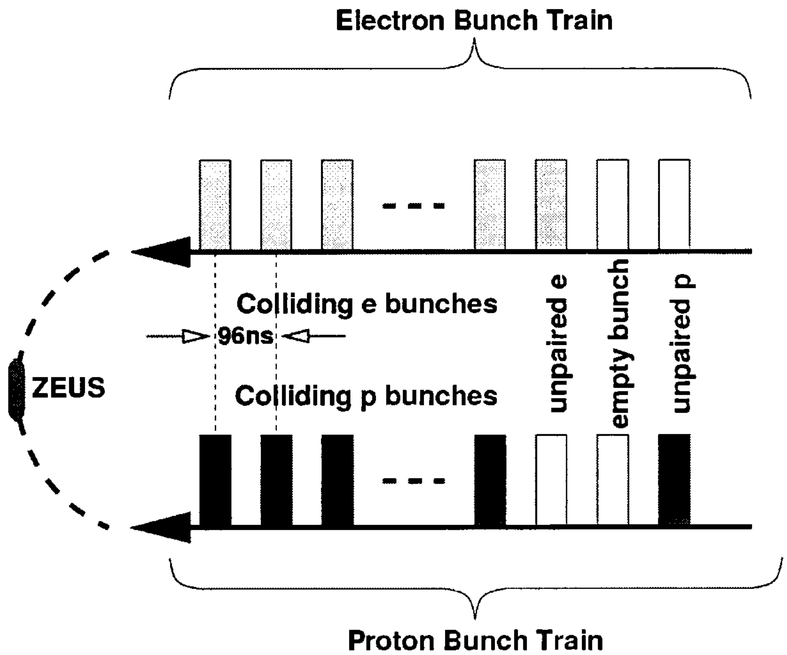

Figure 3.2: Proton electron bunch structure in HERA ring.

particles and leptons should be measured with equal accuracy without any bias. In overall, as full as possible angular coverage should be achieved, so that as small as possible number of particle information is lost. Those ideas described above should be reflected in the design of the detector components, which will be introduced below.

Since the proton beam (920 GeV) has much higher energy than the electron beam (27.5 GeV), the imbalance in the collision energy should be reflected in the construction of the detector, with higher particle flux expected in the proton direction.

3.3 Structure of ZEUS Detectors

Located in the South hall of the HERA, the ZEUS detector is a huge and very complex machine with many components. The main detector is located around the nominal interaction point, while there are some relatively smaller auxiliary detector components located along the beam line at both sides of the main detector. The overall detector dimensions are 12 m $\times$ 10 m $\times$ 9 m and its total weight is 3600 tons [26].

3.3.1 VETO

Located 7 meters on the side where the proton is injected, starting from the outmost of the interaction point, the veto wall (VETO) is a protective iron shield to protect the center detector against particles from the beam halo. There are two scintillator hodoscopes on both sides of the wall to provide signals from the beam background condition.

3.3.2 C5 Counter

To reject beam-gas interactions, the C5 counter (C5) measures the timing of the proton and electron bunches, and can be used to remove those events which do not match the crossing time of the proton and electron. This scintillator counter is located about 3 meters from the interaction point on the same side of the VETO, and very close to the beam.

3.3.3 LPS and FNC

At about 20 to 90 meters in the electron injection direction, there is the Leading Proton Spectrometer (LPS) which measures the proton energy and the Forward Neutron Calorimeter (FNC), which measures the small angle scattered proton and neutron energy. In the neutron calorimeter, two layers of scintillator strips are located at a depth of one interaction length to enhance the position measurement of hadronic showers. Information from these detectors can be helpful to the diffractive physics, but is not relevant to this analysis.

3.3.4 Luminosity Monitor

On the side where the electron is injected, one can also find the luminosity monitor (LUMI), which in fact mainly consists of two lead-scintillator electromagnetic calorimeters (LUMIE and LUMIG). The luminosity is measured by observing the rate of hard bremsstrahlung photons from the Bethe-Heitler process $ep \rightarrow e\gamma p$ [35, 27]. As the cross section of the bremsstrahlung process is already known, one can have the luminosity by dividing the rate by the bremsstrahlung process cross section. The detector LUMIE is located at $Z = -34\ m$ and the other one LUMIG is located at $Z = -107\ m$. They measure the energies of the bremsstrahlung electron and photon, respectively and in coincidence. With the luminosity (L) measured, and the cross section (σ) of the interaction, the number of events (N) taken place can be approximately calculated by $N_{event} = L \cdot \sigma$. The luminosity delivered by HERA from year 1994 to 2000 is shown on figure 3.3.

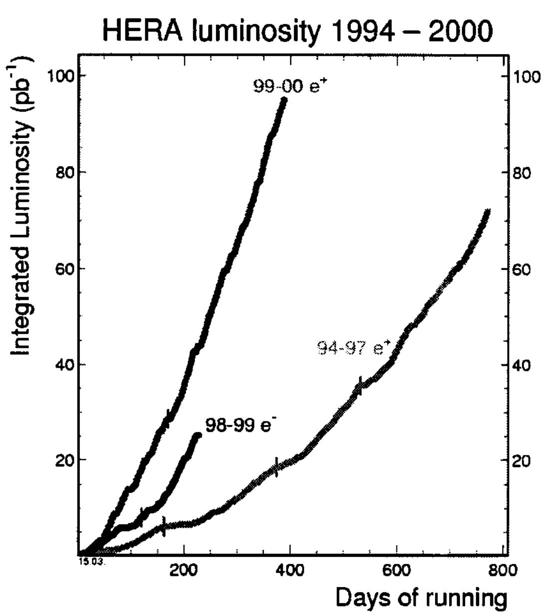

Figure 3.3: Integrated luminosity delivered by HERA from year 1994 to 2000.

3.3.5 Overview of ZEUS Main Detector

Figures 3.4 and 3.5 give an overview layout of the ZEUS detector in X-Z and X-Y projection.

In order to measure the trajectories of outcoming particles right after the collision interaction, the innermost component is the cylinder-shaped high-resolution silicon Micro Vertex Detector (MVD) [34], which covers the beam pipe closely. It was installed during the 2000-2001 HERA upgrade to replace the former broken Vertex Detector (VXD), provides more precise tracking near the main vertex, and makes it possible to identify events with secondary vertices from long-lived particles decay, like hadrons with c-charm, b-bottom quarks or τ leptons, [34] with minimal background.

The tracking detectors are located right outside of the MVD [34] to detect charged particle momenta and trajectories covering all the polar angles. The tracking detectors consist of the Central Tracking Detector (CTD) [37], which is a large cylindrical drift chamber detector, the Forward Tracking Detector (FTD), which is a set of three planar drift chambers (FTD1, 2, 3), and the Rear Tracking Detector (RTD). The Forward Tracking Detector (FTD) consists of 3 disk-like chambers, while the RTD is constructed similar to the FTD, only that, it is much thinner, due to longitudinal imbalance of the energy deposition in the detector.

The tracking system is enclosed by a 2.46 m long barrel superconducting solenoid which provides a magnetic field of 1.43 T.

The ZEUS high-resolution uranium-scintillator calorimeters (CAL) are located right outside of the tracking systems, which can be divided into three components: the forward (FCAL), the barrel (BCAL) and the rear (RCAL) with some overlapping regions. The calorimeter system totally covers 99.7% of the solid angle, and respectively cover the polar angles as shown in the table 3.1. A more detailed description will be in section 3.3.7 below.

Outside of the calorimeter system are the yoke and the Backing Calorimeter (BAC).

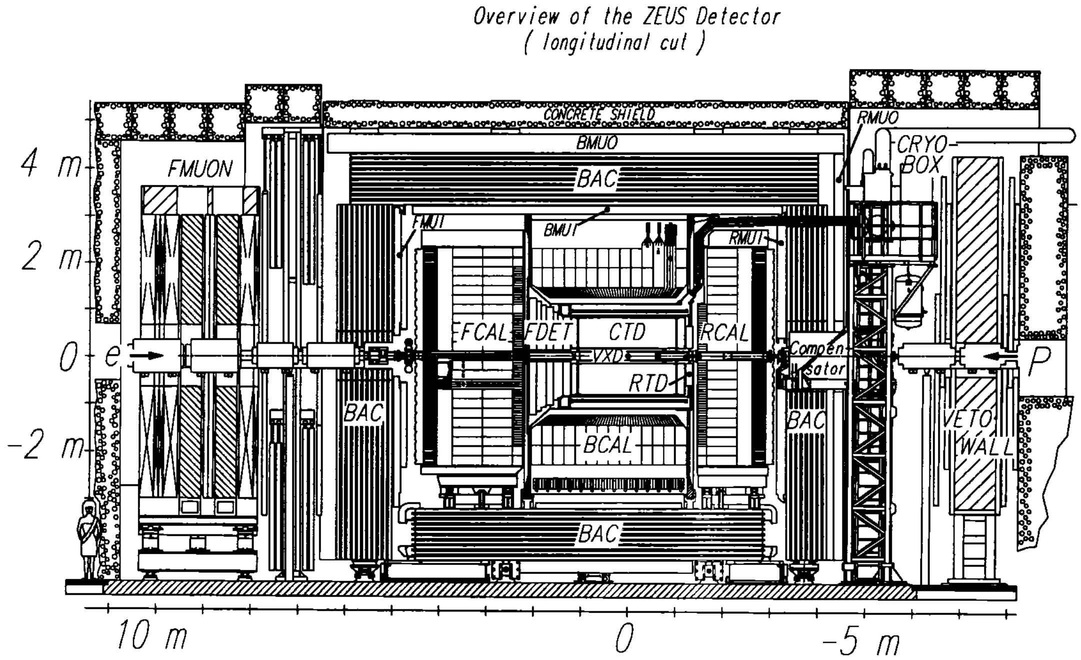

Figure 3.4: Longitudinal view of the ZEUS main detector. The Micro Vertex Detector (MVD) was installed in year 2000-2001 replacing the broken Vertex Detector (VXD), but neither is used in this analysis.

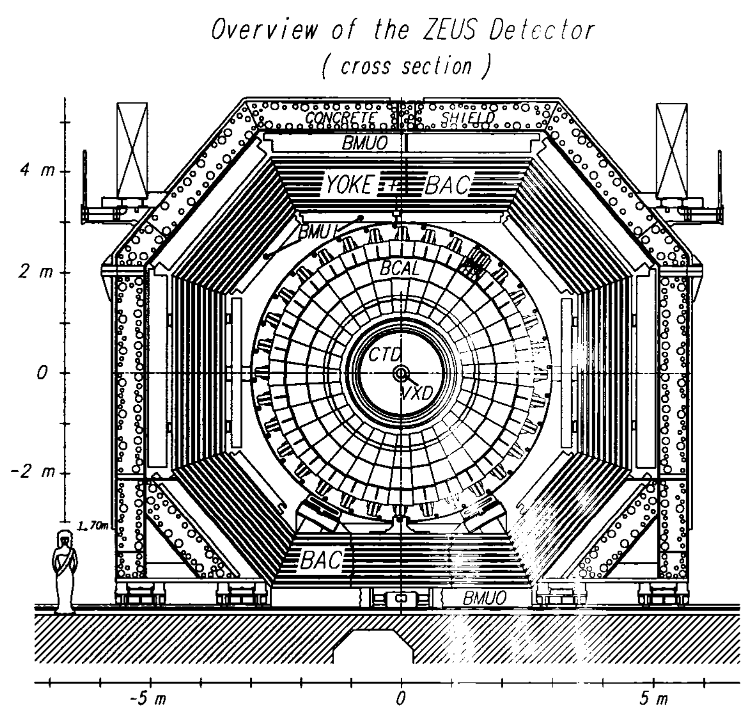

Figure 3.5: Cross section of the ZEUS detector.

The purpose of the iron yoke is to serve as the return of the magnetic field, and it is magnetised by copper coils, which furthermore provide magnetic field for the muon momentum measurement. The purpose of the low-resolution BAC is to measure the energy leakage out of the CAL and detect muons from *ep* interactions and cosmics [29]. To measure the momenta of muons, the Barrel Muon Detectors (BMUI, BMUO) are constructed inside and outside the yoke with streamer tubes. The same kind of muon detectors are also constructed in the forward (FMUI, FMUO) and rear (RMUI, RMUO) regions.

It should be mentioned that the Small-angle Rear Tracking Detector (SRTD), consisting of narrow scintillator strips, is located behind the RTD. It surrounds the beam pipe and is used to measure charged particles scattered at small angle. The Hadron-Electron Separator (HES) consists of silicon diode detectors, and is located inside the RCAL and the FCAL at three radiation lengths deep to help better discriminate electromagnetic and hadronic showers.

More emphasis of introduction will be put on CTD and CAL in the following, as they are more involved in this analysis.

3.3.6 The Central Tracking Detector

The CTD [42] consists of nine superlayers, out of which five are equipped with parallel wires, and four with wires having a small stereo angle to the beam axis. Each superlayer consists of drift chamber cells. The cell design is consisted of inner/outer cylinders, wires, and the end plates at both ends functioning as structure support. Besides eight sense wires, each cell has other wires: ground wires, field wires, and shaper wires. The main purpose of these wires (other than the sense wires) is to provide equal surface field, which should be uniform around the sense wire, to maintain parallel drift trajectories in magnetic field. The shaper wires between superlayers are the shielding to prevent pulse height from altering as the relative alignment between superlayers changes with z and cell azimuth. The cell number increases from 32 in the innermost superlayer to 96 cells in the outermost superlayer, and all together there are 576 cells. The inner cylinder and the end plates are made as thin as possible to avoid particle deflection and energy losses. Furthermore, the inner cylinder has to be strong enough to provide structural support for part of the end-load coming from the wires. So the cylinder has two aluminium-made skins each 0.7 mm thick, with a 9 mm gap between, filled with structural foam. The layout of a CTD octant is shown in figure 3.6. It should be noted that the stereo angles used in the CTD is to achieve a z-measurement. Since the directions of the sense wires are parallel to the beam axis, the z-measurement can be done by taking the time difference between the signal travelling to both ends of the wires. But this measurement is not very precise, as the signal is travelling at the speed of light in the short sense wires. The time difference becomes very small. Therefore, these sense wires in even number of superlayers are tilted, so that the z-measurement can be readout by telling the signals from different stereo sense wires. This is also the reason why the CTD z resolution in stereo is 1.0 to 1.4 mm, while in z-timing it is of the order of 3 cm.

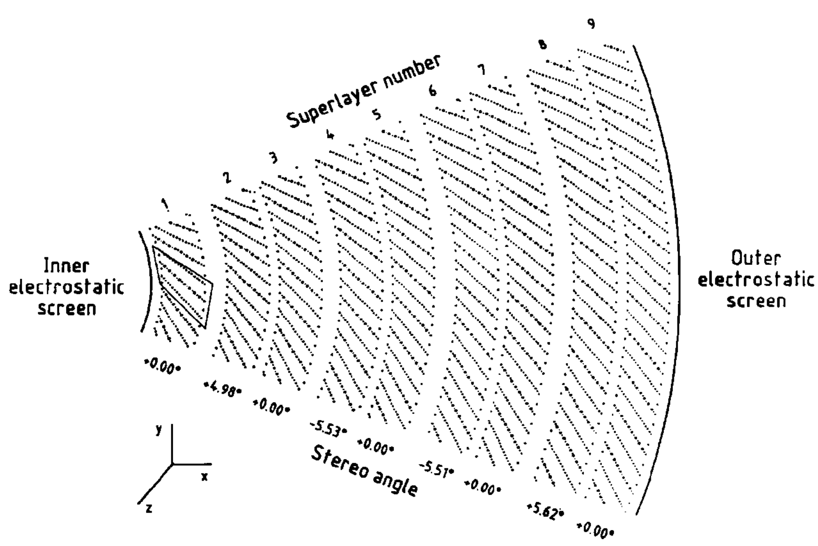

Figure 3.6: The layout of a CTD octant with nine superlayers, numbered from 1 to 9. The angles shown below are the stereo angles at which the even numbered superlayers are tilted.

The CTD is filled with a mixture of argon, CO_2, and ethane, in the ratio of 83:5:12.

When a charged particle penetrates the drift cylinders, the gas is ionized into electron-ion pairs. The positive ions drift towards the negative field wires while the free electrons drift towards the positive sense wires, and trigger an avalanche-like multiplication of electrons. So the hit signal is multiplied to a factor of about 10^4 and thus read out and recorded.

As introduced in section 3.3.5, the CTD operates in a magnetic field of 1.43 T, provided by a barrel superconducting solenoid, which covers the CTD from the outside.

The whole tracking system gives high resolution measurements of the interaction vertex, the trajectories of outgoing charged particles, and cross-checks the energy scale with the calorimeters, which will be introduced below.

The CTD covers a polar angle of $15° < \theta < 164°$ and the full range of the azimuthal angle. The typical transverse momentum P_T resolution for the CTD is $\sigma(P_T)/P_T = 0.0058P_T \oplus 0.0065 \oplus 0.0014/P_T$, where the first term refers to the hit position geometrical resolution, the second one to statistical smearing from multiple scattering, and the last one to multiple Coulomb scattering [42].

3.3.7 The Uranium-Scintillator Calorimeter (CAL)

The ZEUS sampling calorimeters (CAL) [24] are located outside of the tracking system and the solenoid. They measure the energy of the outcoming particles and jets, and are regarded as the key components of the detector.

The Principles of Calorimetry

The idea behind calorimetry is based on how differently particles penetrate the materials and deposit energy in the calorimeter. The calorimeter measures the whole or the fraction of the energy. The calorimeters serve as the material intercepting the particles, followed by the showering process, in which the incoming energy of the particle is dissipated by a cascade of lower energy particles. The showering processes can be generally classified either as the electromagnetic showers, characterized by electrons, positrons and photons, or as hadronic showers, characterized by protons, neutrons, pions and other hadrons.

Heavy charged particles lose energy mainly by ionization effects or excitation with the atoms in inelastic collisions. For any charged particle passing through a material, if the velocity of the particle is more than the velocity at which light travels inside this material, light is emitted, and this effect is called Cherenkov Radiation. Otherwise the dipole radiation interferes destructively with no light emitted.

High energy electrons lose energy mainly similarly to heavy charged particles, but they also lose energy by photon radiation when the electron is scattered in the electromagnetic field of the nuclei. This phenomenon is called bremsstrahlung. Basically, ionization energy loss dominates for low energy electrons, which is characterized by the decreased number of showering particles, while bremsstrahlung dominates for high energy electrons, in which the particle number increases. The transition between the two types of energy losses is the critical energy E_c, which is in inverse proportional to the atomic number of the absorbing material Z. A scaling variable should be introduced here called radiation length X_0, which is the mean distance for an initial electron loses its energy by a factor of $1/e$ to bremsstrahlung, and it is approximately given by equation 3.1:

$$X_0 \simeq \frac{180A}{Z^2}\ [g/cm^2] \tag{3.1}$$

where 'A' is the number of protons and neutrons in the nuclei.

For $E > E_c$, the energy during the radiation after length X is given by equation 3.2:

$$< E_{after} >= E_{before} \cdot e^{-\frac{X}{X_0}} \tag{3.2}$$

The energy is predominantly dissipated by ionization and nuclear excitation. For high energy photons, they mainly interact with matter in three types of processes: pair production, the photoelectric effect, and Compton scattering. For the low energy photons, other physics effects will take place, such as Compton scattering, Raleigh scattering and photonuclear absorption.

Hadronic particles lose energy in a slightly different way and at much larger scales than electromagnetic ones. Hadronic particles may interact with the nuclei from the calorimeter absorber material, and thus a large variety of different interactions can take place with the production of secondary particles within the shower. After the inelastic scattering with nuclei from the absorbing material, some of the nuclei may be in excited states, and will further decay by emitting a photon or other forms of emission as vaporisation, nucleus fission and neutral pions [29]. Electromagnetic shower processes can also take place in hadronic showers.

Basically most energy is lost due to observable ionisation process. But the rest is lost in nuclear interaction, or disruption of the nuclei,. Processes like the breaking of the binding energies, or the production of neutrinos, also make this part of energy 'invisible' to the detector.

Similar to electromagnetic shower process, the scaling variable to parameterize the average energy loss in the hadronic shower is the nuclear interaction length λ, which is given by:

$$\lambda = 35 \cdot \frac{A^{1/3}}{\rho}\ [cm] \tag{3.3}$$

where ρ is the density of the absorbing material in units of $[g/cm^3]$.

The ZEUS Calorimeter Design and Structure

The primary task of the calorimeter is to measure the deposited energy with as high resolution as possible, when either charged or neutral particles penetrate the calorimeter. The calorimeter should be built as compact as possible, to achieve good measurements close to the interaction point, and to reduce costs as well. Granularity and longitudinal segmentations should also provide position information. An as large as possible angle coverage should be achieved. The calorimeter response to different type of particles should enable some particle identification. The response rate should be as high as possible, which also means a fast readout. Due to the different behaviors between electromagnetic and hadronic energy depositions, the difference in the ratio of electromagnetic to hadronic components can dramatically increase the uncertainty of the ZEUS calorimeter measurement. So special attention should be brought in to balance the calorimeter reaction to electron and hadronic particles. Furthermore, on-line trigger should be enabled to reject unwanted events, e.g. good calorimeter time resolution can help reject those background events. In addition, good calibration should be carried out within 1% level.

Based on the requirement described above, the ZEUS calorimeter chooses 3.3 mm thick depleted uranium (DU) U^{238} plates[2] as absorbing material, interleaved with 2.6 mm hydrogenous plastic scintillating plates (SCSN-38). The compensation system works by choosing the thickness of the absorber and scintillator plates, so that the energy from neutron-proton scattering processes and the energy from fast neutrons in uranium fission processes can compensate the energy lost in nuclear breakups, nuclear excitation and neutron evaporation. So the e/h ratio[3] can be brought back close to 1, which is 1.00 ± 0.03 [30] for energies greater than 3 GeV.

The high value of Z of uranium can reduce the critical energy, radiation length and make the detector compact. In addition the natural radioactivity of uranium can provides a means of calibrating the calorimeter.

Just as already described in section 3.3.5, the ZEUS calorimeter is made up of three main parts. The parts are designed in similar ways, except for design concerns on different particle densities and energies. The FCAL is thicker than the RCAL due to the overwhelming particle flux in the forward direction. In addition, the choices of the depths and polar coverages take into account the Lorentz boost and maximum energy deposition of scattered particles. FCAL, BCAL and RCAL are made up of single modules, and all 78 modules are transversally separated into towers, which are longitudinally segmented into electromagnetic (EMC) and hadronic (HAC) sections, as shown in figure 3.7. Those sections are furthermore segmented into cells. FCAL,

[2] In fact, it has a composition of 98.1% U^{238}, 1.7% Nb and less than 0.2% U^{235}

[3] $\frac{e}{h} = \frac{\textit{detector's electromagnetic response}}{\textit{detector's hadronic response}}$

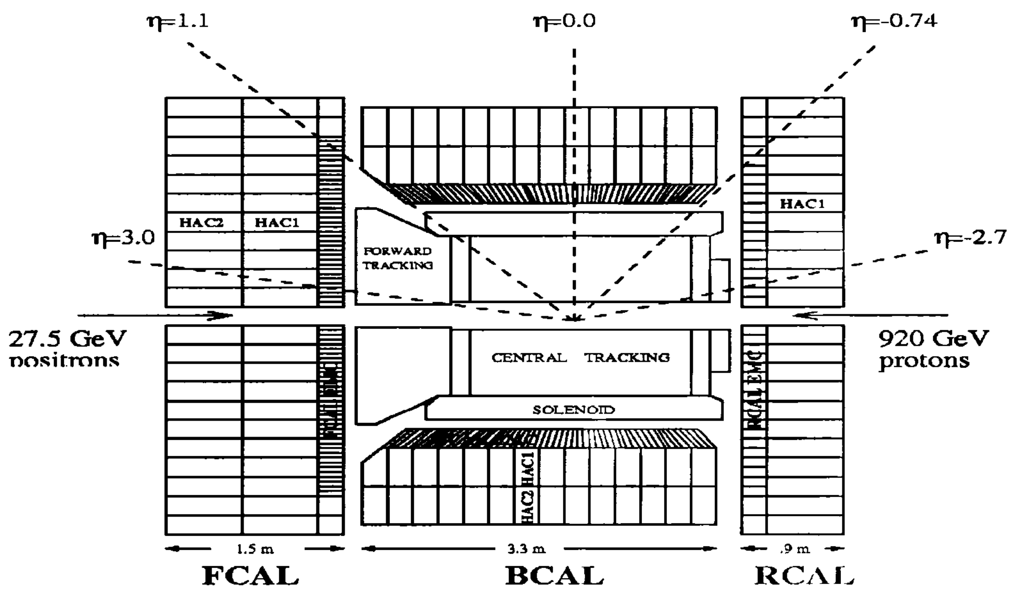

Figure 3.7: Layout of the ZEUS calorimeters. The EMC and HAC cell allocations are displayed in FCAL, BCAL and RCAL. The pseudorapity coverage is also shown.

BCAL and RCAL each has one EMC section, which is made up of four (2 in RCAL) cells in the transverse direction. The HAC section is divided into two hadronic cells (HAC1 and HAC2) in the longitudinal direction in FCAL and BCAL, but only one HAC section is in RCAL. Each cell is connected with plastic wavelength shifters to photomultiplier tubes (PMT) on each side to collect and multiply light coming from the scintillators. This structure is shown in figure 3.8. The typical cell area is 5×20 cm^2 for EMC and 20×20 cm^2 for HAC. The $\approx 1\lambda$ ($25X_0$) [31] depth EMC cells can essentially contain electromagnetical interacting particle energies deposited, while the HAC cell depth varies in FCAL, BCAL and RCAL. The energy resolution is $\sigma/E = 18\%/\sqrt{E}$ for electrons and $\sigma/E = 35\%/\sqrt{E}$ for hadrons, from the result in test beams. The time resolution is 1 ns for minimal energy deposition, and the position resolutions are 1.3 cm vertically and 0.8 cm horizontally [31]. The polar angle, the corresponding pseudorapidity coverage, the maximum depth of FCAL, BCAL and RCAL, the number of EMC sections and HAC sections, their cell area, and depth are summarized in table 3.1.

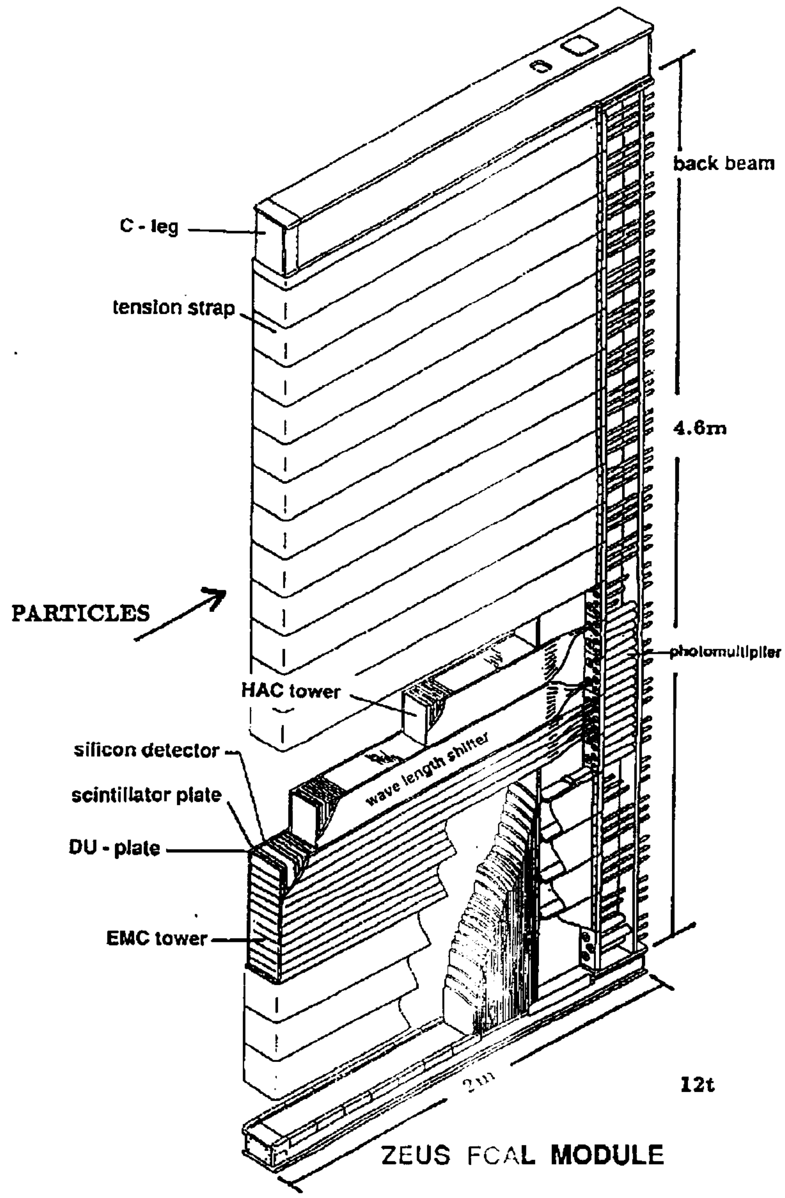

Figure 3.8: The close-up FCAL Layout. EMC towers are sub-divided into cells

A cross section view of the FCAL and RCAL tower and module structure is shown in figure 3.9. The numbering of the modules are also shown on the top. One can notice that module number 12 is divided into two halves, with a square hole in the middle, allowing the beam pipe access into the detector.

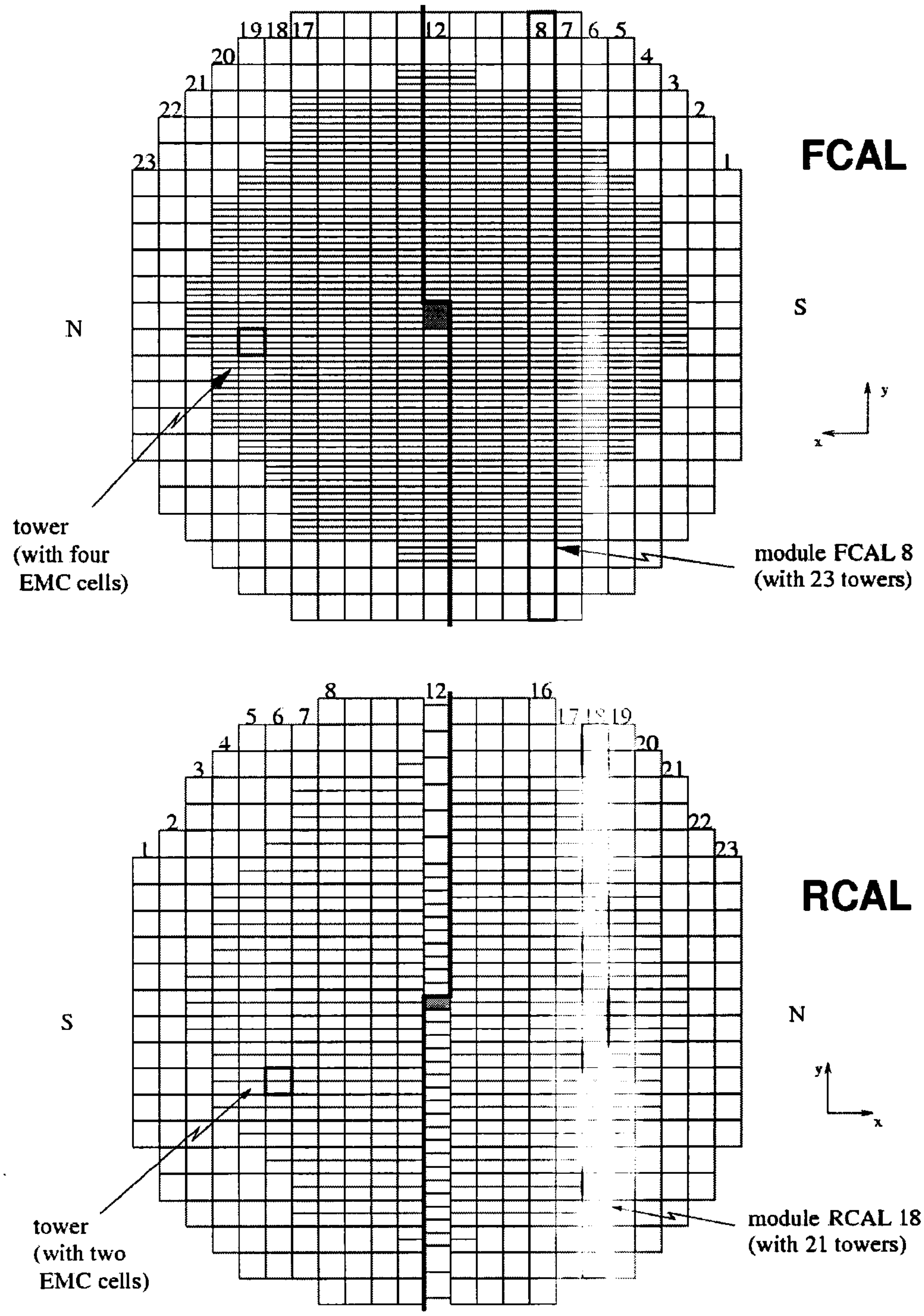

Figure 3.9: Cross section of FCAL and RCAL tower and module structure.

	FCAL	BCAL	RCAL
θ	$2.6° < \theta_{FCAL} < 39.9°$	$36.7° < \theta_{BCAL} < 129.1°$	$128.1° < \theta_{RCAL} < 176.5°$
η	$3.95 < \eta_{FCAL} < 1.01$	$1.10 < \eta_{BCAL} < -0.70$	$-0.72 < \eta_{RCAL} < -3.49$
depth	7.14 λ	5.32 λ	4.04λ
modules	23	32	23
EMC	1	1	1
Cell area	5×20 cm^2	5×24 cm^2	10×20 cm^2
depth	0.96λ	1.10λ	0.95λ
HAC	HAC1+HAC2	HAC1+HAC2	HAC
Cell area	20×20 cm^2	20×20 cm^2	20×20 cm^2
depth	3.09λ + 3.09λ	2.11λ + 2.11λ	3.09λ

Table 3.1: FAL, BCAL and RCAL specifications.

To calibrate or check the calorimeter, 16 modules have been carefully examined in the test beams based on the uniformity and the natural uranium radioactivity. The calibration constants are then transported from the test beam to the ZEUS detector. Many approaches still have be carried out to monitor the calibration stability:

1. Uranium noise (UNO) runs: This tool uses the natural uranium radioactivity. The uranium sends off a low background current in the photomultiplier, and this stable signal can be used to correct the calibration of the calorimeter, by checking the slow drifts from the expected value.

2. Charge injection (Qinj) runs: This method uses the charge injector to simulate the signal coming from the photomultiplier, and thus to check the electronic system.

3. Pedestal (Ped) runs: The method monitors the noise level of the calorimeter cells, so that the whole readout chain can be checked.

4. LED runs and Laser runs: These two methods measure the light and laser pulse injected in the wavelength shifter to check the photomultiplier response, the high voltage system and the electronic readout. [31]

Chapter 4

Data Acquisition and Trigger

When the ZEUS detector is taking data, all data taking components can generate enormous amount of data, but not all those data information necessarily contains the physics that we are interested in. So in the Data Acquisition system, a three-level trigger system is used, to distinguish wanted physics events from background events, such as beam-gas interaction events, cosmic ray initiated events, synchrotron radiation by the electron beams or even simply fake events from detector electronic noise.

It is a very important task to remove the 99% unwanted events out of all observed events, and the real challenges are the speed and efficiency. As collisions may take place every 96 ns, the trigger must be quite capable of making event selection quickly enough to keep up with the data taking rate. The three level trigger system is constructed to make sure of the high efficiency, which means that as many physics events as possible are recorded from all detector components.

4.1 First Level Trigger

Major detector components, such as the Calorimeter (CAL) and the Central Tracking Detector (CTD), have their own local first level trigger, to reduce the overall processing time.

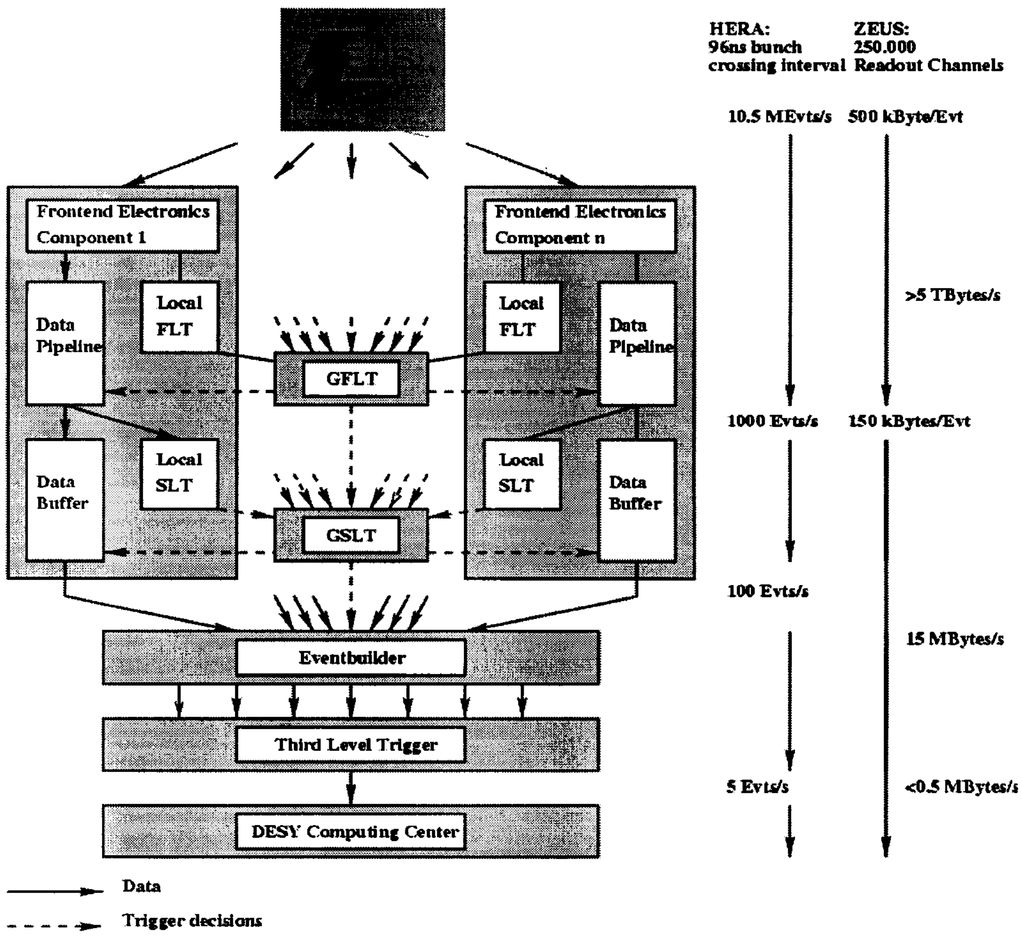

Figure 4.1: ZEUS trigger and Data Acquisition System

The readout times of the individual components are much longer than the 96 ns bunch crossing time, so cannot determine the trigger decision within these 96 ns. The solution is the pipeline system, which is a buffer where data is temporarily stored, while the trigger can have time to make decision.

For example, CFLT [25] is the Calorimeter First Level Trigger, which utilizes a pipelined architecture to provide trigger data information. Four EMC cells and two HAC cells make up the trigger tower EMC and HAC sums. The readout information gathered from those towers are used for pattern recognition, to provide sources of trigger decision, e.g. to require a minimum energy deposition threshold in each CAL

component.
After passing through those first level trigger on local components, data rate is reduced dramatically from 10 MHz to less than 1kHz, by the Global First Level Trigger (GFLT).

GFLT combines pipelined trigger information from each component first level trigger, assembles them into a variety of trigger bits, and make a first trigger decision every 96 ns. A fraction of the data for each event is processed by each component FLT and the GFLT.

4.2 Second Level Trigger

A Second-Level-Trigger (SLT) is set up to achieve greater precision. Its setup is quite similar to FLT's, as each major component also has its own individual second level trigger processors, and a Global Second Level Trigger (GSLT) gathers all local second level trigger information and GFLT tags, as well. GSLT makes trigger decisions, and event rate can be reduced further to less than 100 Hz.

4.3 Third Level Trigger

After the second level trigger, the third Level Trigger (TLT) is the final trigger stage in the on-line event selection. Digitized data from all detector components are now read into the event builder (EVB), which combines information together and send them to TLT, where a PC farm applies more sophisticated trigger event selection cuts, aimed at different off-line analysis purposes, such as jet finding, particle identification and so on. In ZEUS, the TLT trigger is managed by different physics groups.Many TLT filter bits are defined for different analysis requirements. Taking QCD 2000 runs for example, 27 TLT bits are configured for QCD analysis, named HPP01 to HPP27, which are listed in the table below (Table 4.1).

HPP01	High E_T	HPP10	Dijet LRG	HPP19	High P_T track 5
HPP02	Inclusive jet	HPP11	Incl. Jet LPS	HPP20	DIS Forward Jet
HPP03	High P_T track 1	HPP12	Dijet LPS	HPP21	DIS Dijet High Q^2
HPP04	High P_T track 2	HPP13	LRI	HPP22	DIS Dijet
HPP05	FNC Incl. Jet	*HPP14*	*Dijet Low E_T*	HPP23	DIS Dijet Low Q^2
HPP06	Dijet FNC	HPP15	Dijet High E_T	HPP24	DIS Forward Jet Kt
HPP07	Incl. Jet BPC	HPP16	Prompt Photon	HPP25	DIS Dijet kt high Q^2
HPP08	Dijet BPC	HPP17	Multijet	HPP26	DIS dijet kt α_s
HPP09	High LRG	HPP18	High P_T track 4	HPP27	DIS Dijet kt Low Q^2

Table 4.1: Year 2000 TLT bits set ups. HPP 14, dijet low E_T is the one used for this analysis.

In this analysis, the HPP14 TLT filter was used to select low E_T dijet photoproduction event, which can preserve the photon remnant jet concerning its low transverse energy property. This will be further discussed in the next chapter.

4.4 Computing Environment and Off-line Analysis

A layout of the ZEUS computing environment is shown in figure 4.2, including the off-line computing software and the Monte Carlo event simulation software[1].

ZDIS: ZDIS is a software environment, where Monte Carlo[1] programs generate artificial events.

MOZART: It is a GEANT [46] based detector simulation software. The events generated from ZDIS pass through MOZART.

ZGANA: The ZGANA program simulates the ZEUS trigger chain.

ZEPHYR: It is a program to reconstruct events from raw data, taking signals (calorimeter, tracking detectors ...) from the ZEUS detector, or simulation programs.

[1]The Monte Carlo will be introduced in the next chapter.

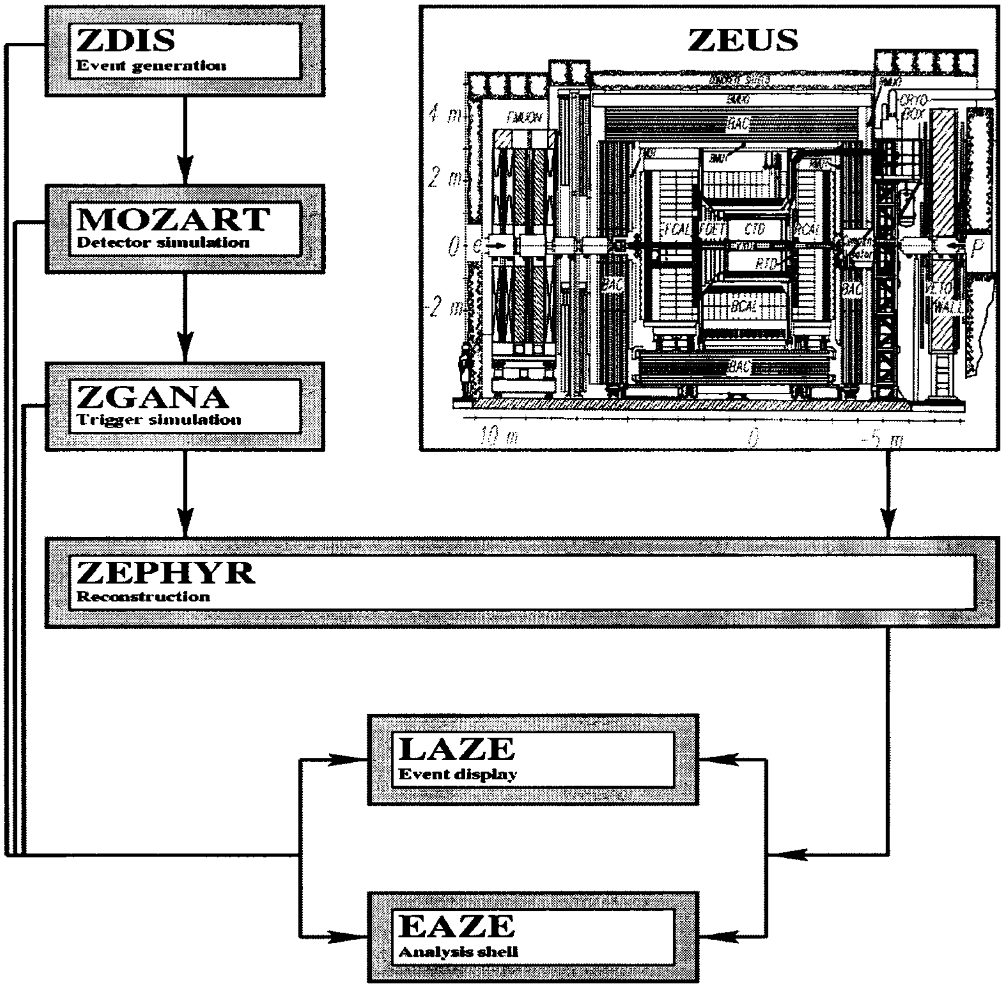

Figure 4.2: The ZEUS computing environment: simulation vs experimental branches.

EAZE: EAZE provides an interface to the user to devise individual event selections, to meet his/her own analysis purpose.

ORANGE: It is an EAZE based ZEUS software package for off-line analysis, which will be introduced below.

LAZE: LAZE is an event display which provides graphical viewing of events signals in the detector, e.g. the tracks in the CTD, and the energy deposited in the CAL cells.

ZARAH: This main ZEUS analysis facility consists of 20 Intel Pentium III 1 GHz clock rate processors, and 20 Xeon 2.2 GHz processors[2]. It gives full support to the ZEUS computing infrastructure, batch data analysis, and event data storage as well.

ZES: The ZEUS Event Store is an object-oriented database. Configured as a tag database, it provides a fast and flexible way of selecting the events which are used in analysis.

4.4.1 ORANGE

A useful software package built on EAZE should be introduced here which greatly helps in a large part of this analysis. To collect together the standard and similar preliminary parts of any physics analysis in ZEUS, such as the basic physics particle identification, jet finding and selection routines, the FORTRAN software package ORANGE was set up.

Advanced reconstruction code, correction routines, and so on are implemented as generally stable 'official' library routines. One only has to call the routines to perform specific parts of an analysis. The routine and variable common block sections can be turned on and off according to the requirements of the analysis. Experience has shown ORANGE to be very reliable. ORANGE provides a good pre-selection of analysis samples, and it provides a common ground, on which analyses can be more easily compared with each other. One can refer to the ZEUS webpage [28] for more details.

4.4.2 ZUFOs

As described in chapter 3, the ZEUS tracking system mainly measures the position and momentum of charged particles, while the calorimeter can sample a fraction of both charged and neutral particle energies. The fact is that the tracking detectors often achieve higher accuracy on the measurement of the momentum of the charged

[2]http://www-zeus.desy.de/components/offline/offline.html

particles [38]. So in the final state reconstruction, information from both the tracking and the calorimeter should be combined to achieve better performance. This is done in the reconstruction process known as ZEUS Unidentified Flow Objects (ZUFOs)[3].

The combination of the tracking and calorimeter information can be illustrated as the following:

- If there is energy from an object deposited in the calorimeter, but there is no tracks associated, this object is counted as the energy of a neutral particle and the calorimeter information is used.
- If there are good tracks detected in the tracking detectors, but there is no energy deposited in the calorimeter associated, this object is counted as energy of charge particles, and assumed to be a pion.
- If there are both matched tracks measured in the tracking detectors, and energy deposited in the calorimeter, the object is counted as the energy of a charge particle. But the decision on which of the track momentum or the calorimeter energy should be used is based on the relative uncertainties of the two measurements. The one with the smaller uncertainty is favored.

In the analysis, the ZUFOs are always used to provide corrected tracking and energy information. The advantage of using the ZUFOs is demonstrated later in section 6.2.1.

[3]The ZUFOs are also called Energy Flow Objects (EFOs) in ZEUS publications

Chapter 5

Event Selection and Reconstruction

In this thesis, the data from the year 2000 with positron-proton scattering was analyzed, whereby one had protons energy $E_p = 920$ GeV, positrons energy $E_e = 27.5$ GeV and an integrated ZEUS gated luminosity 55.1 pb^{-1} (HERA delivered 66.4 pb^{-1}). That year's data sample has already provided enough statistics for this analysis, and even more events would not improve the result significantly. This is the reason behind the choice of year 2000 data. The photoproduction events are selected by requiring that the electron is scattered at very small angle and lost in the beam pipe. A cut on W is applied off-line. Also in the trigger configuration, hard scattering events at low Q^2 are selected from background events by cutting on the transverse energy of the jets. The details of the cuts follow. Some of the cuts values are taken from relative reference analysis, while others are tuned in this particular analysis.

From here on in this thesis, the analysis and the studies performed on the observed jets and photon remnants are the author's own unique work.

5.1 Trigger Selection

As described in the previous chapter, a three level on-line trigger system is used in ZEUS. The first level trigger takes events that have a minimum transverse energy deposit in the calorimeter, and at least one track in the CTD pointing to the interaction point. In the second level trigger, more dedicated cuts are applied to the calorimeter energy and timing to remove beam gas interaction. The first and second level trigger mainly remove non-physics events, while in the third level, photoproduction event selection setups are designed in the trigger system, to fit in physics analysis requirement that two or more low E_T jets are kept.

As described in the previous chapter, there is more time in the on-line third level trigger to perform dedicated selection cuts, particularly the k_T algorithm jet reconstruction can also be performed to apply cut on jets. In this analysis, TLT-HPP14 (one can refer to table 4.1) is used to select low E_T dijet photoproduction events in the laboratory frame. In this jet algorithm regime, jets are reconstructed by using the information from the ZUFOs. The TLT-HPP14 trigger requires at least two jets with $E_{T,jet}^{1,2} > 4.5$ GeV, $\eta_{jet}^{1,2} < 2.5$ as loose cuts.

It should be mentioned here that when the off-line reconstruction is performed, some additional requirements are stored in a bit structure (DST bits). Those DST bits are associated with TLT trigger branches. TLT-HPP14 is associated one on one with DST-b77. Table 5.1 shows the corresponding trigger selections used in this analysis.

Trigger:	FLT	SLT	TLT	DST
configuration:	*slot* – 42	*branch* HPP01	*branch* HPP14	DST *bit* 77

Table 5.1: Trigger configuration used in this analysis

5.2 Event Selection

After those on-line triggers to extract photoproduction physics events from beam-induced interactions, cosmic-ray events, and other background interference, off-line cuts are applied on the kinematic variables as the following.

To select only photoproduction events, just as discussed in section 2.6.1, means that the exchanged photon should be close to real and the momentum transfer small. The cut requires y to be within the range 0.2 to 0.85 [10]. According to equation 2.18, it is equivalent to a cut on the photon-proton center of mass energy, 142.3 GeV $< W <$ 323.1 GeV.

In photoproduction events, the incoming electron is scattered at very small angle, which means that it will be lost in the beam pipe without being detected. The neural network SINISTRA is used to identify those of the scattered outgoing electrons which are detected in the calorimeter. But an event in which an electron candidate is found by the SINISTRA electron finder cannot be arbitrarily removed with a mark of DIS events, as the electron found by SINISTRA might not be the outgoing scattered electron, but an incoming non-interacting electron, or even might not be an electron at all. So, provided an electron candidate is detected, the inelasticity of the events y_e is calculated by the formula 2.5. With the help of the Monte Carlo simulations[1], the values of the selection cut can be justified. It can easily be seen in figure 5.1 [2] that a cut $y_e > 0.75$ [10] should be applied to remove neutral current DIS event. It should be noted that each electron candidate found by the electron finder also comes with a *probability* variable, which shows how likely this electron candidate found is really an outgoing electron. So *probability* should also be cut on at a high value to ensure the correct cut on y_e. But in this analysis, it can be seen from the control plots 5.1 that a *probability* over 90% [10] is already sufficient.

[1]The Monte Carlo simulation will be introduced in Chapter 6. The physics be hind the MC plots used in this analysis will be introduced in section 6.1.1 with HERWIG.

[2]In control plots throughout this analysis, the MC is normalized to the DATA with their event numbers.

In order to remove electron beam-gas and DIS events, and just as already introduced in chapter 2, the inelasticity Bjorken-y_{JB} can also be calculated by using the Jacquet-Blondel method [44], representing the fraction of the incoming electron energy that is carried away by the almost real photon. So to remove beam-gas interaction events, $y_{JB} > 0.2$ [36] is required. Meanwhile, in order to remove Neutral Current DIS events, in which case the electron is not properly identified but energy is still deposited in the calorimeter (whereby y_{JB} would be close to one) y_{JB} should also be required to be less than 0.85 [36]. Also it should be noted that based on equation 2.13 and 2.14, cutting on y_{JB} with $0.2 < y_{JB} < 0.85$ is equivalent to cut on $E^{ZUFO} - p_z^{ZUFO}$ with 11.00 GeV$< E^{ZUFO} - p_z^{ZUFO} <$ 46.75 GeV.

In order to remove proton beam-gas interaction or cosmic background, The Z position of the interaction vertex is required to be inside the region $|Z_{vertex}| < 60$ cm [36]. This can assure the events selected are in the geometry region where the detector has good acceptance and efficiency.

Another source of non-photoproduction events are the charged current deep inelastic scattering (CC DIS) events, which have been introduced in section 2.6.2. In this case electron would also not be detected, and this can fake a photoproduction event. But in CC DIS events, the outgoing neutrino (or anti-neutrino) cannot be detected in the detector. So the total momentum in the transverse plane cannot be conserved any more, which give a clue to identify such CC DIS events and thus to remove them. To take into account the calorimeter resolution factor, the ratio of the total missing transverse momentum to the square root of the total deposited energy should be cut by: [36]

$$\frac{P_T^{missing}}{\sqrt{E_t}} < 1.5\ \sqrt{GeV} \tag{5.1}$$

In the control plot of figure 5.1, the DATA is compared with the MC. The selection cuts have been marked with shadow or lines. It should be noted that in the plot of y_e, a large difference between DATA and MC occurs when y_e is below 0.75, so a cut $y_e > 0.75$ should be applied. Plots of electron candidate and electron probability are presented. In vertex tracking, and $\frac{P_T^{missing}}{\sqrt{E_t}}$, a good agreement already

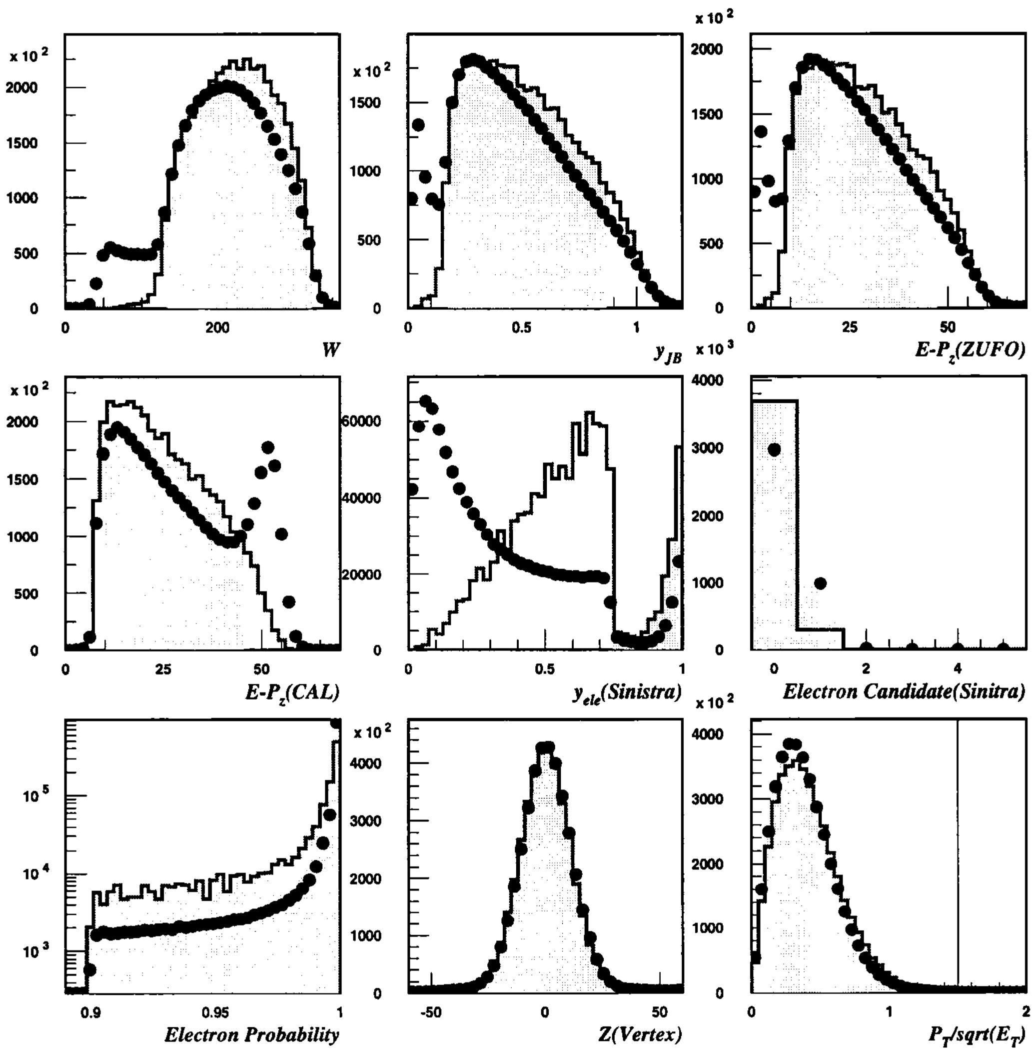

Figure 5.1: These control plots give the relation of DATA and MC after the TLT trigger selection. Solid dots are DATA, while lines are MC. The shadowed areas are the part of events taken by applying the selection cuts described in section 5.2.

exists between DATA and MC. But the cut of Z(vertex) with $|Z_{vertex}| < 60$ cm, and $\frac{P_T^{missing}}{\sqrt{E_t}} < 1.5\ \sqrt{GeV}$ can only slightly enhance photoproduction event selections, as they cut off only 0.00025% and 0.0037% of the events, respectively.

In figure 5.2, all related kinematic variable distributions are shown both on DATA and MC, after all the cuts discussed above have been applied. One can see in general that much better agreement is achieved between DATA and MC after the cuts. In this series of control plots, solid black dots are DATA, while lines are MC. Describing from the top in the left to right, the first plot shows W, then followed by y, $E - P_Z$ calculated both from ZUFO and CAL, then the momentum plot shows the momenta measured in CAL in Z direction. The y value from SINISTRA is shown in the next plot, followed by 'Electron Candidate Number', its probability, and the corresponding y value calculated from the electron method. The next plot shows the vertex track hit in Z direction. Then the followed plot shows number of tracks in CTD and the corresponding momenta in Z direction. $E_T(CAL)$ shows the transverse energy distribution in CAL. Then the 5 next plots are the jet kinematic variable distributions from the k_T algorithm, showing the number of jets in each event, the transverse energy, pseudorapidity, and azimuthal angle distribution of each jet. The last plot in the right bottom corner is x_γ, where there seems to be an disagreement between DATA and MC. The source of the discrepancy might be the low cutting edge of the jet transverse energy, in which case DATA takes in much more background jets that the MC. So more dedicated cuts on the jet kinematic variables will be applied in the following section, where the reasons for these cuts will also be described.

5.3 Jet Selection

The pure photoproduction events have been selected by the above cuts. Jets are now searched for in the reconstruction process with an inclusive k_T algorithm, which has been described in section 2.7.2, using a radius $R = 1$ in the pseudorapidity (η) - azimuth (ϕ) space. Jets are selected with those configuration options or cuts in the table 5.2:

In figure 5.2, the results of the jet reconstruction described above had been shown with number of jets, pseudorapidity, azimuthal angle distribution and x_γ. In the jet reconstruction process, the E_T cut is however set at 2 GeV [10] to preserve the photon remnant candidate, but it also lets in a lot of background jets. This side effect is reflected in the plot of jet numbers, in which a lot events contains more than 3 jets. Another indication is from x_γ, which can separate direct and resolved process nor-

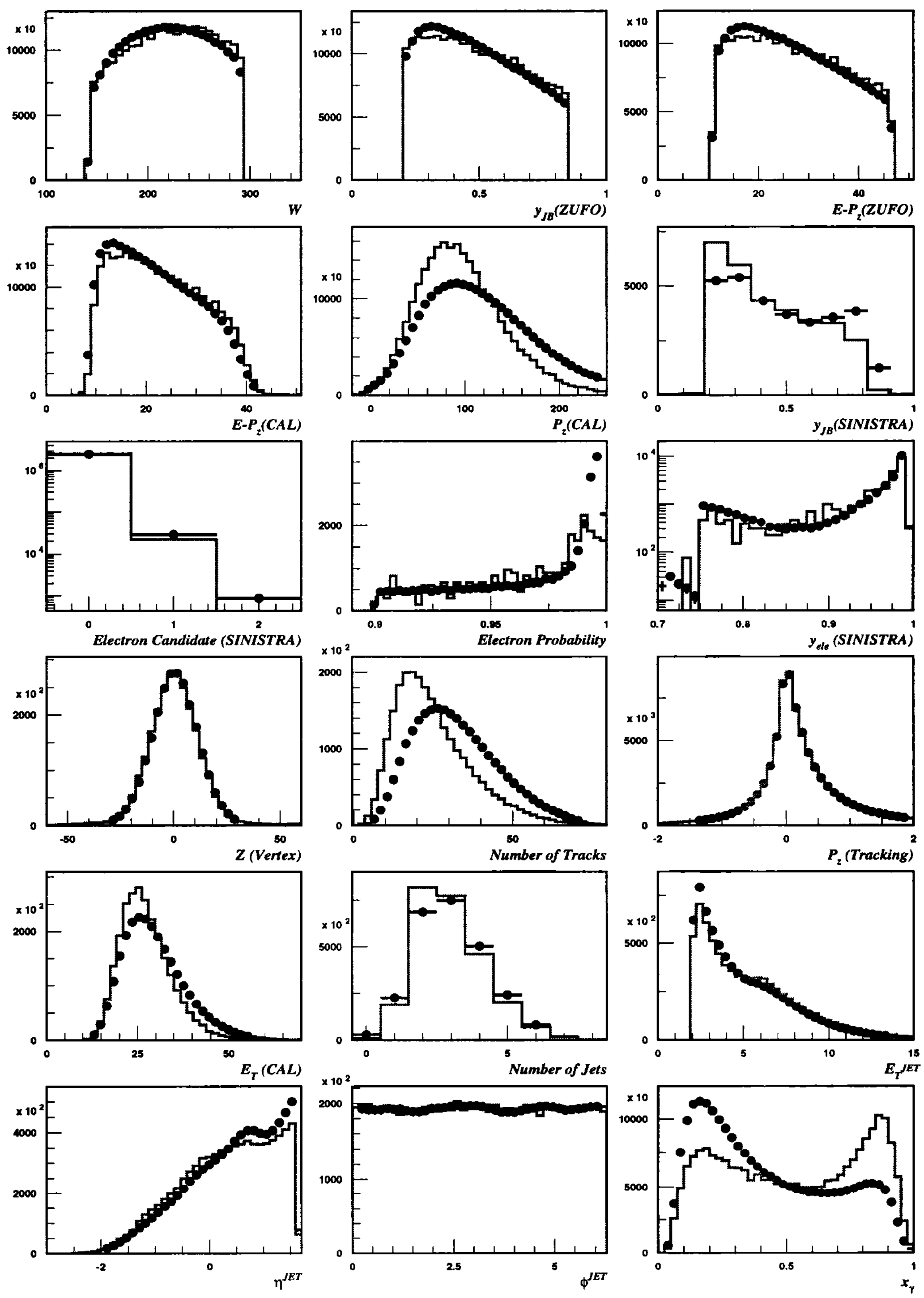

Figure 5.2: Control plots after cuts. Dots are DATA and lines are MC.

Option	Parameters	Description
Jet Mode	ZUFOs	use ZUFOs information
k_T Mode	3212	3=pe collision type, 2= ΔR used, 1= derive relative pseudoparticles angles from jets, 2= P_T scheme used
Scheme	2	E scheme in ep collision
e Rejection	no	To determine if e excluded, electron still taken
Frame	Lab Frame	No boost
Scale	Inclusive mode	determines what reconstruction algorithm to use and sets the scale for jet finding
SCVARA	0.8	correspondence to Q_{DA}
Ycut	0	KTCLUS jet resolution parameter
Resolution	0	KTCLUS jet resolution parameter
E_T Cut (GeV)	2.0	Minimum E_T of returned jets
η_{min} Cut	-4.0	Minimum η of returned jets
η_{max} Cut	1.6	Maximum η of returned jets

Table 5.2: The k_T algorithm jet finder parameters in this analysis.

mally with two or three jets only. In plot 5.3, obvious differences still exist between DATA and MC.

To further improve the jet selection, i.e. to select only hard dijet events, while preserving the photon remnant candidate jets, more dedicated selection cuts must be carried out on the jets themselves. Thus, the dedicated cuts are performed on transverse energy, $E_T^1(jet) > 8.0$ GeV, $E_T^2(jet) > 6.0$ GeV and on pseudorapidity, $\eta_{jet}^{all} < 1.6$, $\eta_{jet}^{Photon\ Remnant\ Candidate} < -1.0$. [10]

In each event, jets are sorted with their transverse energy from highest to lowest. Events with less than 2 jets are rejected. For those events with only 2 jets, those ones which cannot satisfy the $E_T^1(jet) > 8.0$ GeV, $E_T^2(jet) > 6.0$ GeV, $\eta_{jet}^{1,2} < 1.6$ are rejected. For those events which contains more than 2 jets, the same cut as for two-jet events is also applied, moreover starting from the third highest E_T jet, the pseudorapidity is required to be less than -1.0 [10], otherwise, this particular jet is abandoned, but the whole event is not rejected. This way, a large number of background jet, which might have been misidentified as the photon remnant jets inside the event, especially those, for example, from the proton remnant jet and travelling in the forward direction, can be rejected.

5.4 Jet Selection Control Plot

In figure 5.3 and 5.4, the improving effect of the dedicated selection cut described in the previous section is shown such that all the plots in the left column describe the jet kinematics from the jet reconstruction, while the plots in the right column are the corresponding ones after the dedicated cuts.

In figure 5.3, the basic kinematics for jet, number of jets in the events, the transverse momentum, pseudorapidity and azimuthal angle distributions are shown before and after the cuts. It can be seen that the number of events with more than 3 jets have been reduced dramatically, and also that the pseudorapidity and x_γ distributions achieve considerably better agreement between DATA and MC.

The plots in figure 5.4 give more detailed kinematic distributions on highest, second highest, and third E_T jet. Better agreement between DATA and MC can also been seen after the dedicated cuts.

After all the selection cuts have been applied to the data, the number of events taken, how many jets are contained in events are shown in table 5.3.

5.5 Event Transverse Momentum Conservation

In the X-Y plane, which is also referred to as the transverse plane, the total momentum of the event should be conserved, i.e. the total momentum components on the

	all jet events	1-jet events	2-jet events	3-jet events	4-jet events	5-jet events	6+ jet events
after TLT	3589587	276564	1140021	990298	611017	281223	290464
after all cuts	466483	0	427738	37589	1146	10	0
percent kept	13.0%	0%	37.5%	3.8%	0.19%	0.036%	0%

Table 5.3: Event numbers and percent of events kept after selection.

X and Y axes should also be conserved. In figure 5.5, there are 12 plots. The 8 plots on top are the total energies in X, and Y directions, by summing up all the jets in the multi-jet-event (the top two plots are for all jets in all events). The distributions peak at zero, which clearly proves the momentum conservation in X-Y plane, although the peaks for four-jet-events are not so obvious around zero due to the lack of statistics. The four plots at the bottom are the sums for only the first two and three jets in multi-jet events. The purpose for these four plots is to evaluate how much impact the lack of the jets other than the first two and three could have on the conservation of transverse momentum. It can be seen that the conservation is not very much disturbed, which indicates that a cut on the total momenta on X or Y direction to select momentum conserved di-jets can not be significant.

5.6 Jets Event Display Examples

How the events look like (e.g. the tracks in the CTD and the energy deposition in the CAL) in the detector is visualized by a client-server display called ZeVis, which is based on the Root package.

An example of a direct photoproduction process event is shown in figure 5.6. One can see that there are two jets energy depositions in the CAL (BCAL and FCAL), and they are back-to-back in the X-Y plane view.

An example of a resolved photoproduction process event is shown in figure 5.7. One

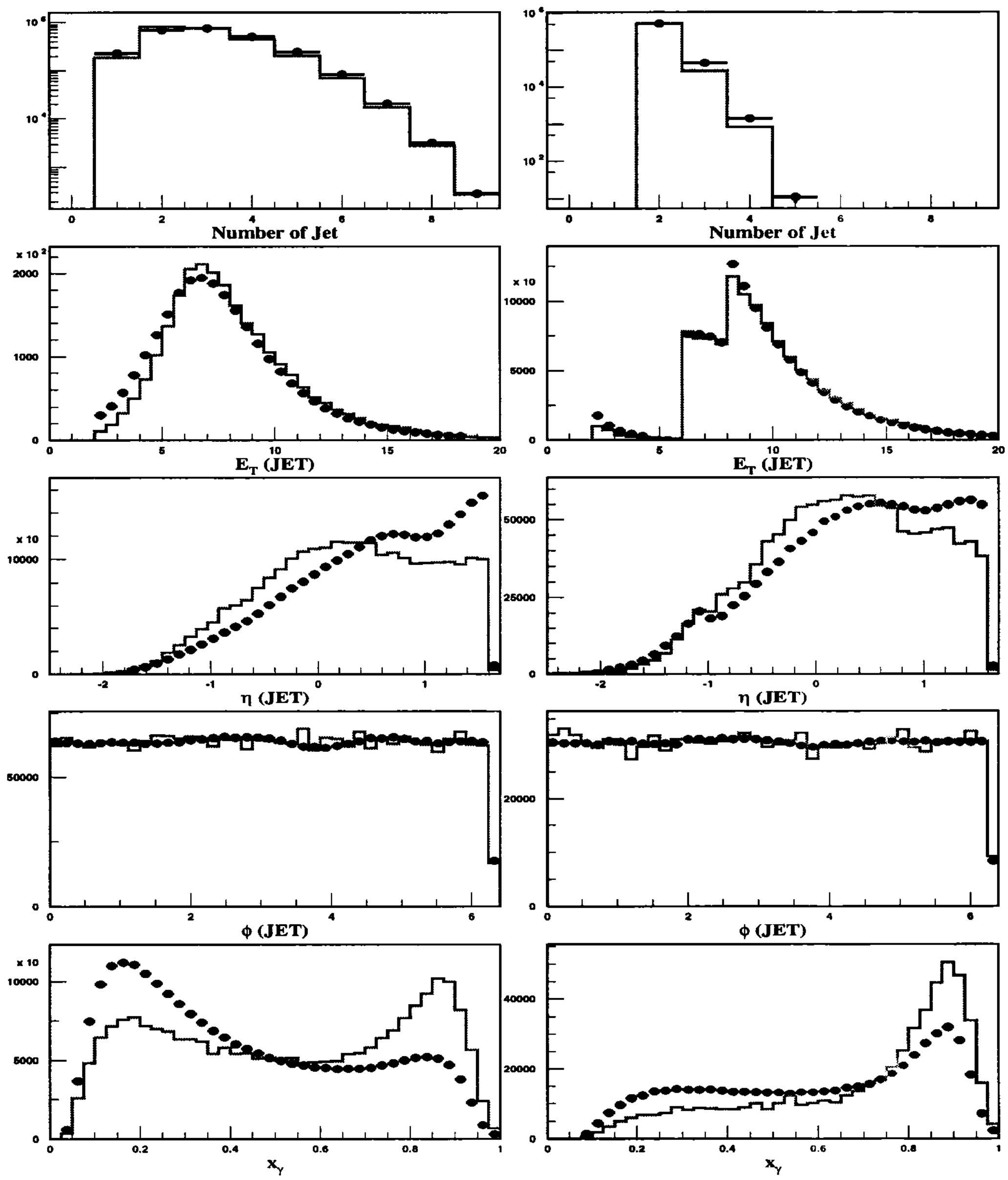

Figure 5.3: Jet selection improvement control plot in kinematic variables. Dots are DATA, and lines are MC. All plots in the left column are after jet reconstruction, and those in the right column are the corresponding variables after the cut $E_T^1(jet) > 8.0$ GeV, $E_T^2(jet) > 6.0$ GeV, $-5 < \eta_{jet}^{1,2} < 1.6$, $\eta_{jet}^{Photon\ Remnant} < -1.0$ are applied.

can see that there are three jets energy depositions in the CAL. Two of them deposited energy in the BCAL and FCAL, while the one deposited energy in RCAL

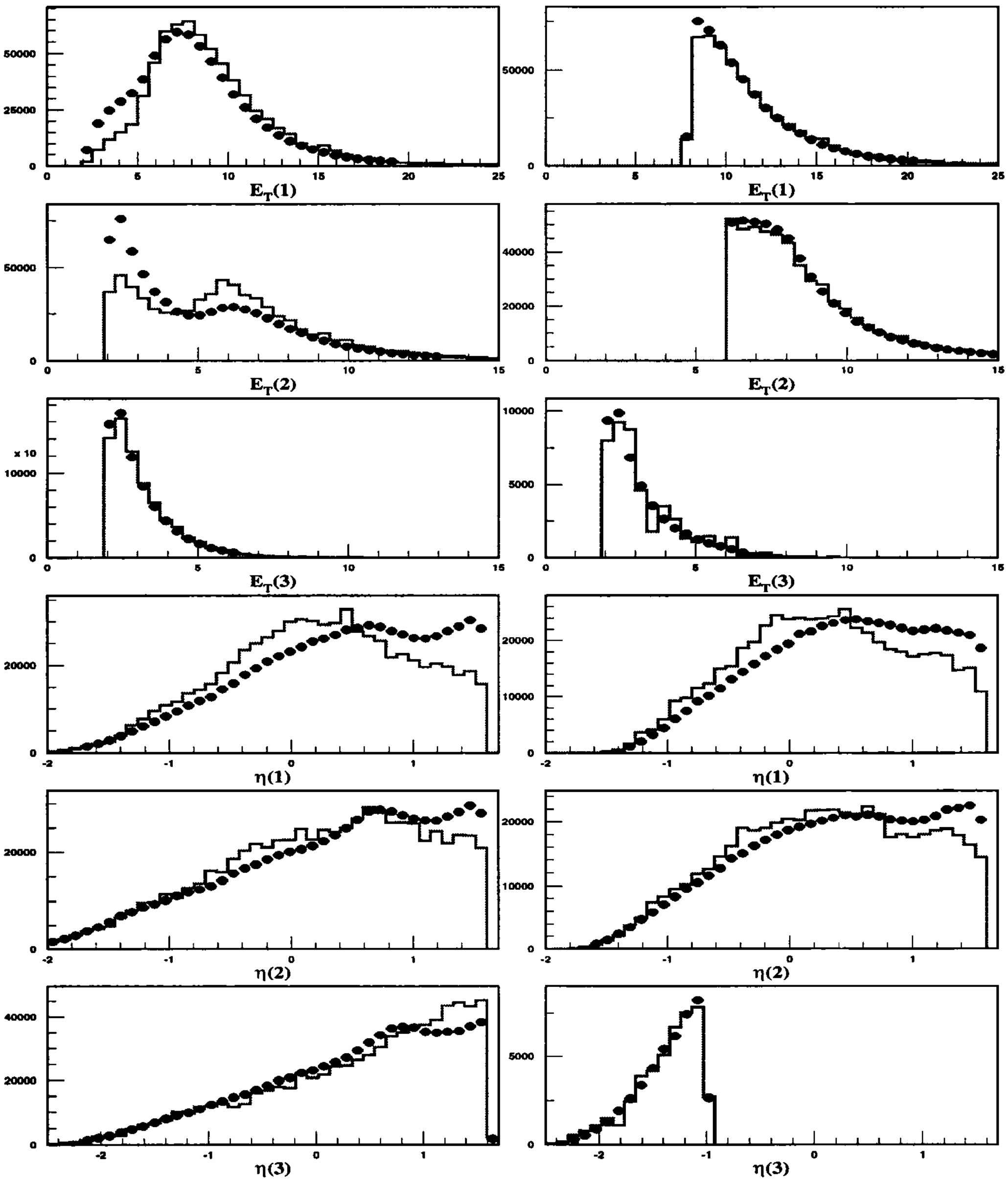

Figure 5.4: Jet selection improvement control plot. Dots are DATA, and lines are MC. All plots in the left column are the first, second and third jet transverse energies, and the pseudorapidity after jet reconstruction, and those in the right column are the corresponding kinematic variables after the cut $E_T^1(jet) > 8.0$ GeV, $E_T^2(jet) > 6.0$ GeV, $-5 < \eta_{jet}^{1,2} < 1.6$, $\eta_{jet}^{Photon\ Remnant} < -1.0$ are applied.

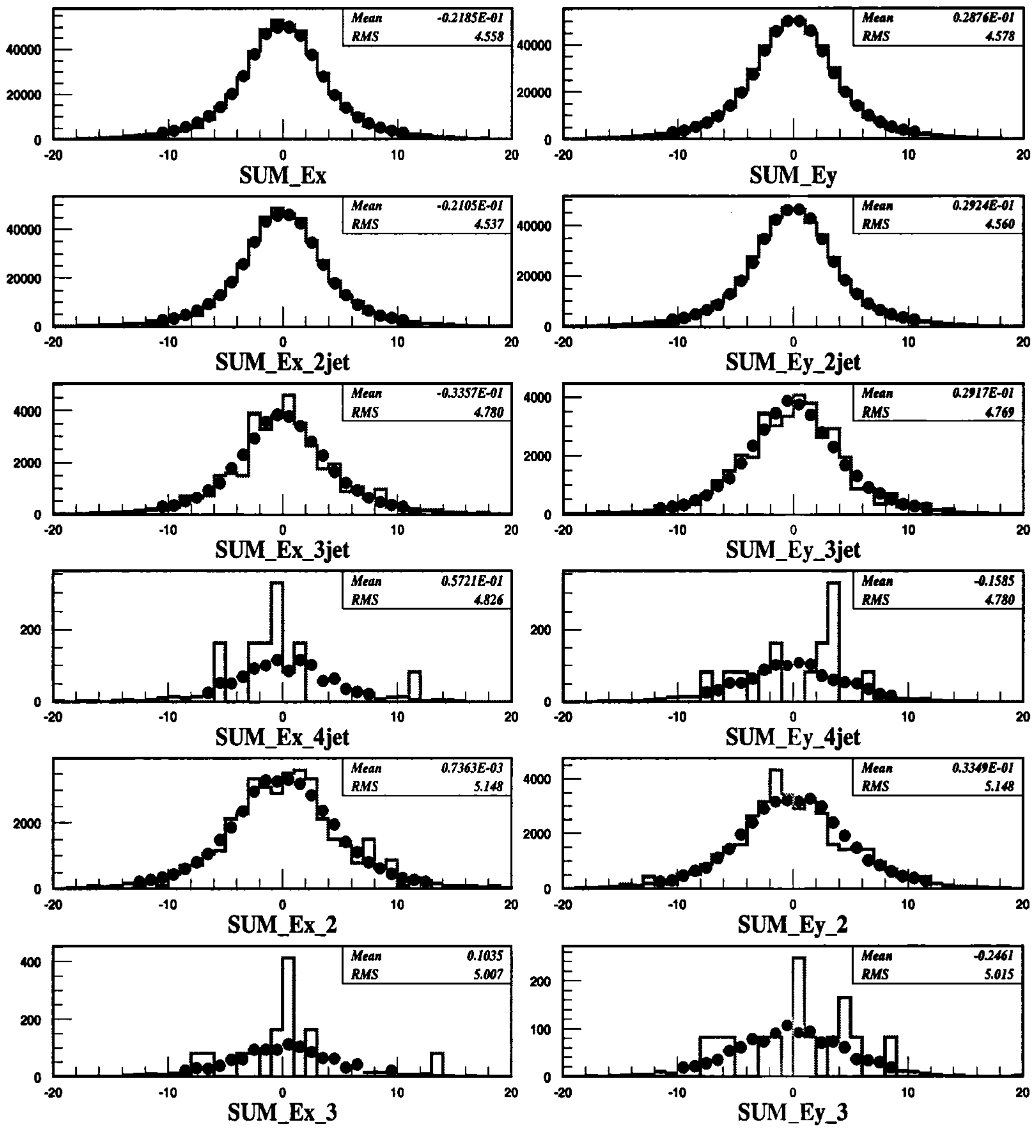

Figure 5.5: SUM_Ex, and SUM_Ey are the total energy summed up in X and Y direction. SUM_Ex_2jet, SUM_Ey_2jet, SUM_Ex_3jet, SUM_Ey_3jet, SUM_Ex_4jet, SUM_Ey_4jet are respectively, the two-jet, three-jet, and four-jet events total energies in X, Y direction. The worse disagreement occurs for four-jet events, due to the lack of statistics. SUM_Ex_2 and SUM_Ey_2 are the sum of the first two E_T jets from three and more jet events, while SUM_Ex_2 and SUM_Ey_3 are the sum of the first three E_T jets from four and more jets events. Dots are DATA, and lines are MC.

(above the beam) indicates a photon remnant jet candidate.

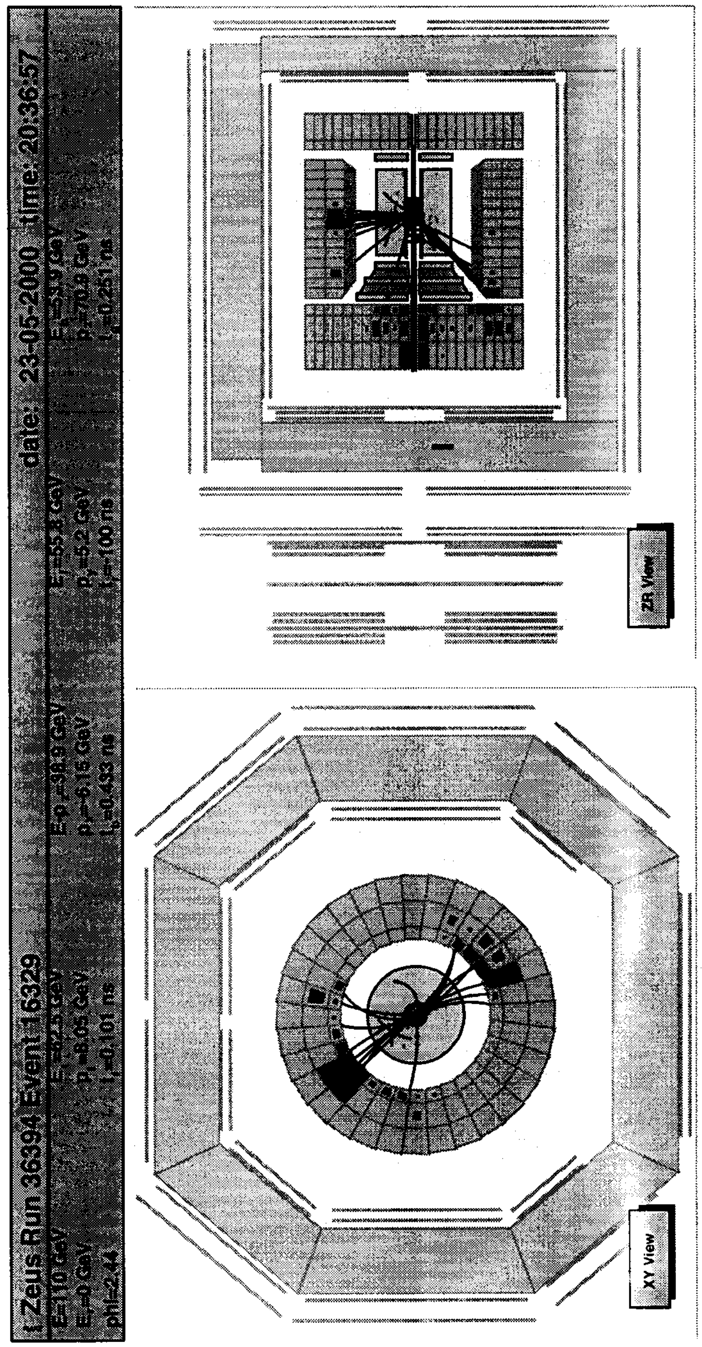

Figure 5.6: A two-jet direct photoproduction event shown on ZEUS event display(ZeVis).

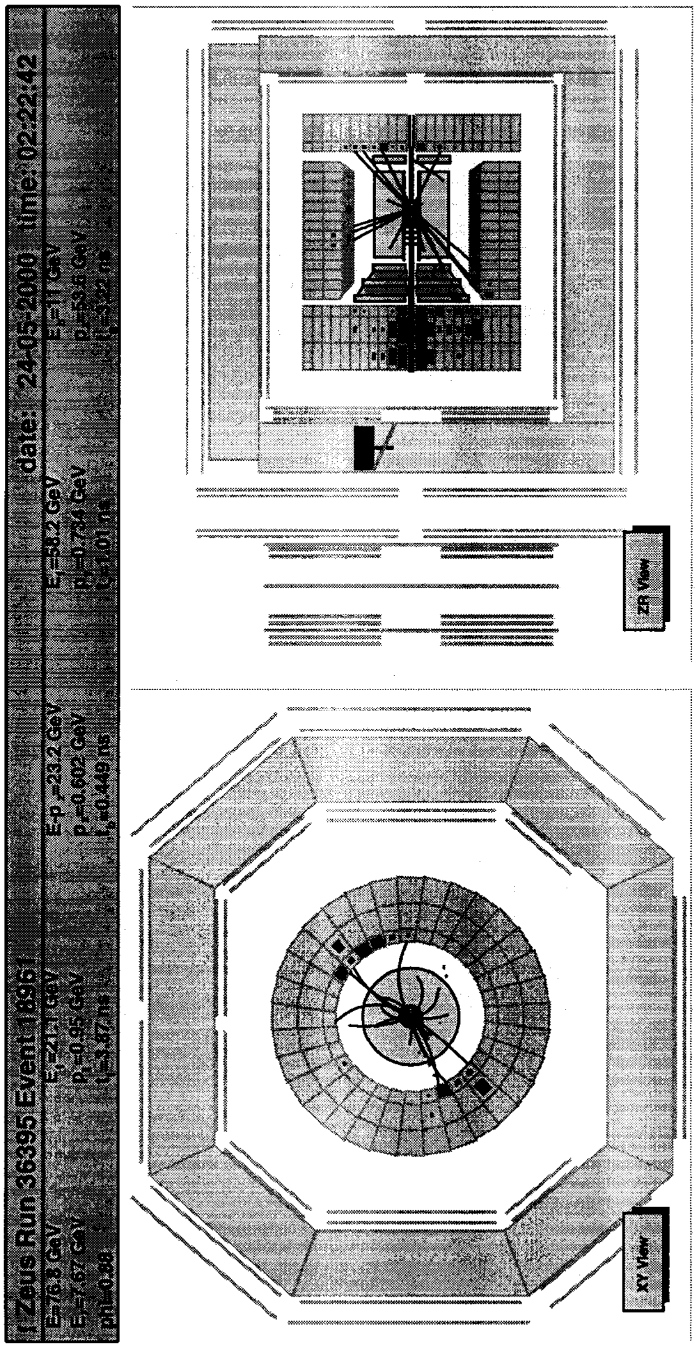

Figure 5.7: A three-jet resolved photoproduction event shown on ZEUS event display (ZeVis), with a photon remnant candidate.

Chapter 6

Monte Carlo Simulation and Energy Correction

6.1 Monte Carlo Simulation Overview

After any detector is set up, it must be known how well the detected data information is the reflection and measurement of real interacting particles and events. So if possible, test beams had been set up beforehand to make measurements and improve the detector and its performance. In test setups, the input conditions are well known, so that the expected outcome of the detector read-out can be predicted and calculated and thus, the detector can be calibrated and the data corrected. In practice, it is impossible to put the whole ZEUS detector itself in test beams to check its response. Monte Carlo simulations are tools containing relatively all we know about the physics and the detector. One can then use the test beam information, develop Monte Carlo simulations from them and apply these back on to the ZEUS detector.

Monte Carlo simulations generate artificial events considering the lower order interaction processes, and simulating the beam remnants hadronization and other possible properties. The created events are passed through a detailed detector simulation performed by GEANT [46], which contains all geometries of the detector, so that the acceptance for each class of events can be determined and studied. Those simulated events are also useful to determine whether different physical models, such as different parton distribution functions, really agree with the data or not.

As illustrated in the figure 6.1 below, three steps are carried out to create Monte Carlo events.

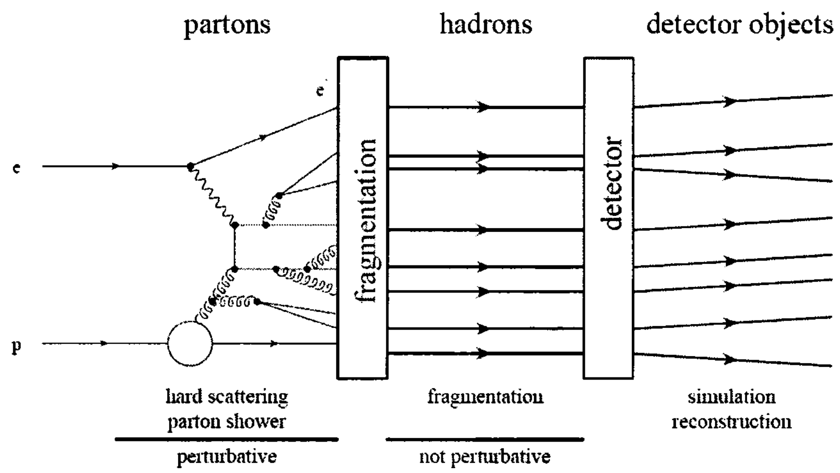

Figure 6.1: Schematic view of the Monte Carlo simulation method

The first step is to simulate the hard scattering of the partons, as understood from the theory. The outgoing parton level events are then passed through a hadronization model which fragments the color-charged partons into color-neutral hadrons, together with the decay of unstable hadrons. The fragmentation process is just modelled phenomenologically as the physics behind it is not well understood yet. This level is called 'hadronic level final states' simulation. It should be noted that among the particles taken for the hadronic final states, not only hadrons are included, as decayed products like leptons and photons may also appear in this final state level. The last step is to pass the hadron level events through the simulated detector and trigger, and store the resulting events in the same format as the raw data, which is called 'detector level' Monte Carlo events. The events can be taken out and used in the off-line analysis to be compared directly with the data. [39]

6.1.1 HERWIG Generator

HERWIG (Hadron Emission Reactions With Interfering Gluons) is one of the most commonly used Monte Carlo simulation packages for general purposes [40]. It can simulate hard lepton-lepton, lepton-hadron and hadron-hadron scatterings. The HERWIG dijet low E_T photoproduction MC sample used in this analysis comes from the following set-ups (Table 6.1). The MC sample is passed through all the selection cut exactly like the DATA.

Generator HERWIG version 6.100
Inclusive Photoproduction (IPROC=19130)
E_p = 920 GeV
E_{e+} = 27.52 GeV
PDF p = CTEQ4 LO
Charmed Quark Mass = 1.5500 GeV
Bottom Quark Mass = 4.9500 GeV
Max Q^2 = 4.0 GeV^2
Min P_t = 2.5 GeV (in QCD 2 $\rightarrow$ 2 processes)
Dijet demands Min E_T = 3.0 GeV and $\eta = -3.0 \rightarrow 3.0$
Jet finder = KTCLUS (mode 3212), running on final state
Integrated Luminosity = 1.07507153 pb^{-1}
Number of events generated: 3,600,000

Table 6.1: The HERWIG Monte Carlo event sample is generated with the set ups in this table.

6.1.2 PYTHIA Generator

The PYTHIA generator is a Monte Carlo events generator, emphasized on multi-particle production in collisions between elementary particles, such as e^+e^-, pp, ep interactions. The name PYTHIA is adopted from the historical Pythia the priestess of the oracle of Delphi [41]. Simulation performed in PYTHIA is based on LO matrix elements, parton showers and Lund hadronization. The positron-photon vertex was modelled according to the Weizsäcker-Williams approximation. Details will be given in section 7.2.

6.1.3 Detector Simulation

The detector level simulation is performed in a program MOZART [47] in ZEUS, which is based on the GEANT simulating package [46], as introduced before. MOZART constructs a virtual ZEUS detector that can simulate the magnetic field, different detector component response, particle decays, multiple scattering, energy loss in dead material, and any other physical processes. Naturally the output of the simulated events are stored in the same format as the raw data.

Trigger simulation is done by another program called ZGANA, which works in the same way as the real detector trigger.

6.2 Monte Carlo Correction

Due to the limited detector acceptance, event migration, or resolution smearing, the outcome of the detector cannot truly describe the pure interaction process. So the convoluted detector level data must be corrected back to the hadronic final state level for comparison with theory. One would ask why not correct it back to parton level, and the reason is to minimize the data dependence on the fragmentation model, as different specific parton fragmentation models have to be used from parton level to hadronic final state level.

6.2.1 W and y Corrections

To select photoproduction events, just as described in the previous chapter, cuts have been applied with the help of Monte Carlo event simulations. But whether the selection variables should be corrected to overcome detector limitations, their hadron level and detector level value relations should be evaluated. The important selection variables used in chapter 5 are the center of mass energy W and inelasticity y. They can be calculated from both the CAL and the ZUFOs. The scatter plots of detector level $W(DET)$ against hadron level $W(HAD)$ by using the ZUFOs are shown in figure 6.2. One can see that the scatter distributions are centered around the reference line with slope of one. The resolution distributions peak very closely at zero, with very small root mean squared values, which indicates that the peak is quite sharp. This plot can tell that the W and y values do not need to be corrected. The reason behind this is the use of the ZUFOs, which has already corrected the signals in the detector. As a comparison, the similar scatter plots and the resolution plots of W and y values taken from only the CAL are shown in figure 6.3. One can see that a dramatic offset can be observed from the true values to detector values both on scattered plots and the resolution plots.

6.2.2 Jet Energy Correction

Jets energies however need to be corrected to hadron level, as the final state particles will interact with the detector components. Energy measurements from the calorimeter are also affected by the detector resolution and many other factors, such as the intervening dead materials, so that the reconstructed energy will generally be different from the original one.

The idea of the correction is as follows. The generated Monte Carlo events in both hadronic final state level and detector level are totally understood as regards their detailed kinematic information. So one can compare the corresponding Monte Carlo jets at both hadron and detector levels, to get their energy correlation, e.g. a 'correlation' factor, in different kinematic regions. Then one can apply the same correlation factor on the detector data energy values, so that the data can be corrected back to the hadronic final state level.

In this analysis, the standard bin-by-bin correction method is used briefly in the

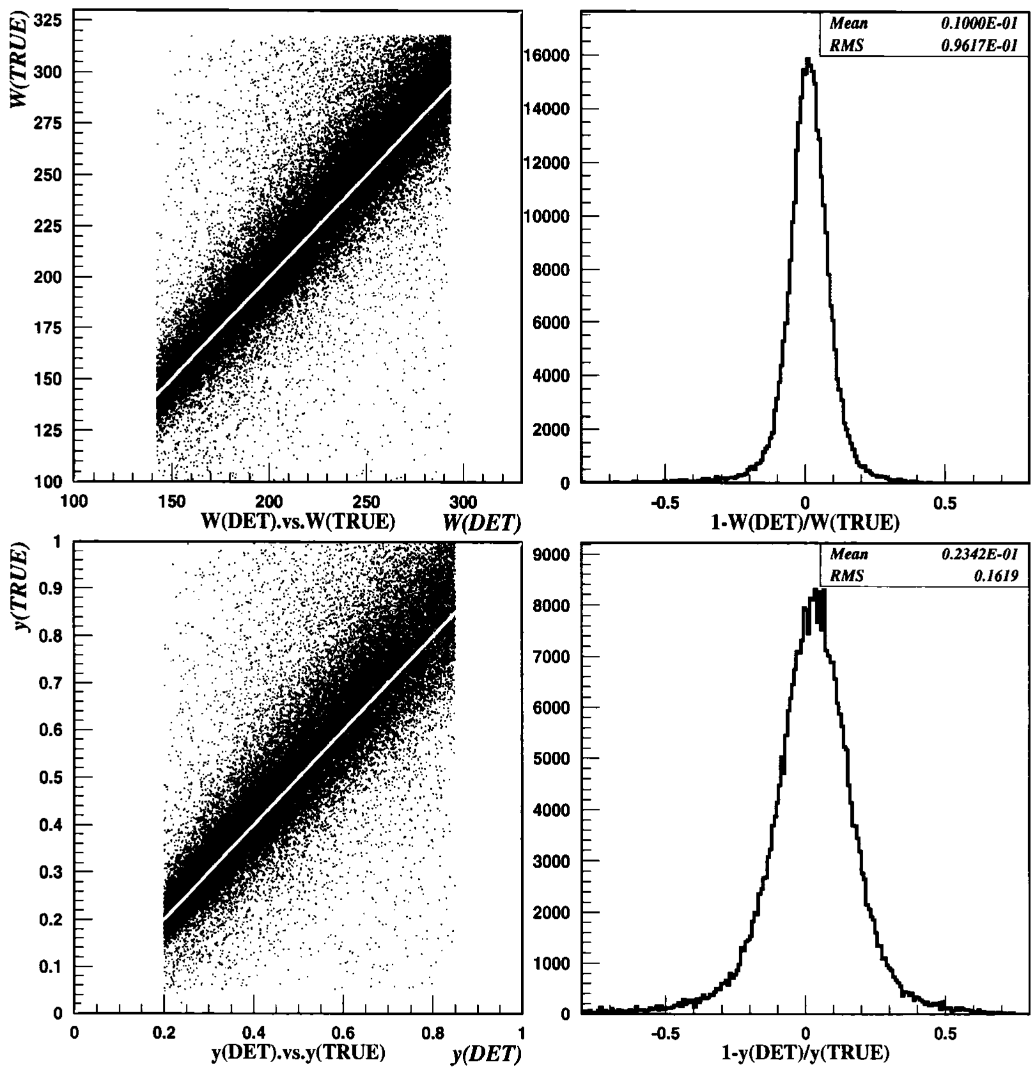

Figure 6.2: W and y scattered plots and resolution plots between detector level and hadron level (TRUE) with ZUFOs information. The white lines in left plots are slope=1 ideal reference lines, on which the detector level values are equal to hadron level (TRUE) values.

following steps:

1. The same cuts as for DATA are applied at both the hadron level MC and detector level MC. Jets are reconstructed using the k_T clustering algorithm with the following cuts: (See section 5.2)

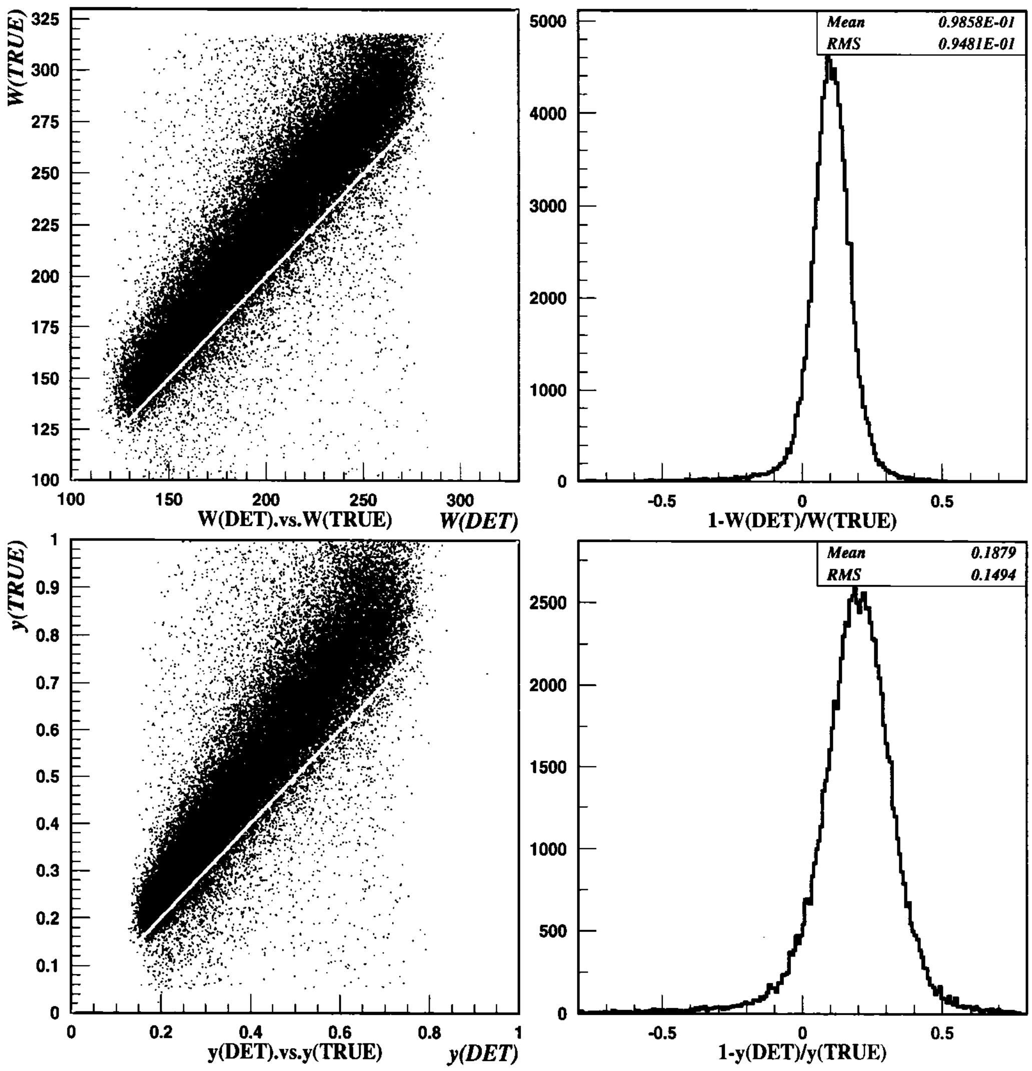

Figure 6.3: W and y scattered plots and resolution plots between detector level and hadron level (TRUE) with only CAL information. The white lines in left plots are slope=1 ideal reference lines, on which the detector level values are equal to hadron level (TRUE) values.

- $0.2 < y < 0.85$
- Two highest E_T jets: $E_T^1 \geq 8.0$ GeV, $E_T^2 \geq 6.0$ GeV, $\eta^{1,2} \leq 1.6$
- Photon remnant jet candidates: $E_T^3 \geq 2.0$ GeV, $\eta^{\gamma\ Remnant\ Candidate} \leq -1.0$

2. The reconstructed jets are sorted with respect to their E_T. Due to the detector

resolution, acceptance and event migration effect, the hadronic jets may also be lost at the detector level. One has to be sure that any pair of jets under comparison is correlated at both levels. In other words, one requires that the detected jet is really the one simulated in hadron final state level. So a matching between hadron level and detector level jets must be carried out by measuring the distance in the $\eta - \phi$ plane in the lab frame as:

$$\Delta R = \sqrt{(\eta_d - \eta_h)^2 + (\phi_d - \phi_h)^2} \tag{6.1}$$

ΔR is calculated on all combinations between hadron level jets and detector level jets in the same events, and the minimum distance pairs are taken as "matched pair", if this distance is smaller than 1. This matching procedure is carried through each event.

3. For each matched jets pairs, correlation between their E_T should be found out (figure 6.4 shows the overall correlation distribution between them). The E_T of the jet at the hadron level is taken as the original one and that of the jet at detector level as the reconstructed one.

The jets are distributed along the whole E_T range, which makes it impossible to fit with all jet pairs. So one has to divide the energy range into 18 E_T bins with the following boundaries in the hadron level.
2, 3, 4, 5, 6, 7, 8, 9, 10, 11, 12, 13, 14, 15, 16, 18, 20, 24, ∞ (GeV)

It should be noted that the bin size is not smaller than the detector resolution, otherwise the bins would have been meaningless. However, the bin size cannot be too small, otherwise the migration effect across neighboring bins can become significant. At the same time, small bin sizes can better represent all the jets inside this bin with higher resolution, and thus give better results on the fitting.

The mean values are then computed for the jets belonging to each group at both levels, and each bin is represented by one point in the correlation plot, which is coordinated by the mean $\langle E_T^{hadron} \rangle$ on the X-axis at hadron level, and the mean

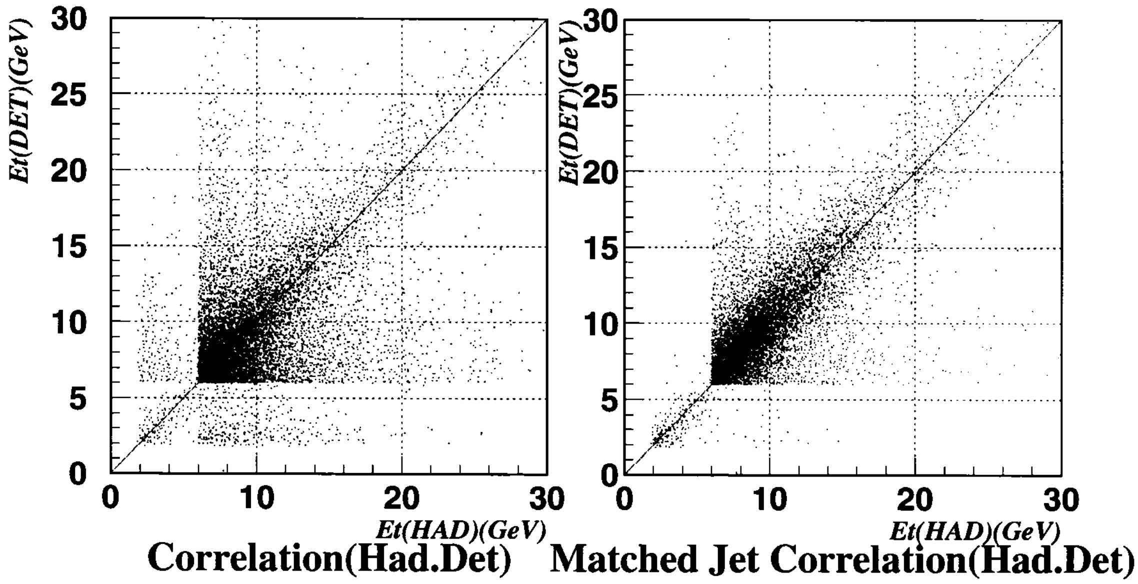

Figure 6.4: Correlation between E_T^{HAD}(X-axis) and E_T^{DET}(Y-axis) over the whole pseudorapidity range. The diagonal line is a slope unity reference line. The left plot is the correlation between all hadron and detector level jets. The right plot is the correlation only between matched jets. A large number of unrelated jets pairs far from the reference line has been removed in the matching procedure.

$\langle E_T^{detector} \rangle$ at detector on the Y-axis, as shown in figure 6.5. The correlation between the matched jets is parameterized with a linear function by fitting the distribution of the detector level E_T as a function of the hadron level energy. The fitted function is:

$$E_{T,jet}^{DETECTOR} = b + m \cdot E_{T,jet}^{HADRON}. \tag{6.2}$$

4. Because different pseudorapidity regions can have very different energy loss effect, the previous step must be done inside 11 different η_{jet} bins, which have the following boundaries:

   -2.80, -1.35, -0.90, -0.60, -0.25, 0.00, 0.25, 0.50, 0.75, 1.00, 1.25, 1.50

   The boundaries are determined by the requirement that jets should be in comparable numbers in order to minimize the statistical error, and at the same

time, the accuracy per pseudorapidity bin should also be satisfied.
In table 6.2, slope and offset values of the fitted line are shown for each η bin.

η_{jet} *region*	minimum E_T region (GeV)	offset: b (GeV)	slope: m
]-2.80,-1.35]	2 -	0.22	0.87
]-1.35,-0.90]	2 -	0.81	0.86
]-0.90,-0.60]	6 -	2.56	0.72
]-0.60,-0.25]	6 -	2.15	0.78
]-0.25,0.00]	6 -	1.37	0.89
]0.00,0.25]	6 -	1.19	0.90
]0.25,0.50]	6 -	1.11	0.93
]0.50,0.75]	6 -	1.10	0.93
]0.75,1.00]	6 -	0.52	0.98
]1.00,1.25]	6 -	0.94	0.94
]1.25,1.50]	6 -	1.14	0.91

Table 6.2: Correlation fit parameters in different pseudorapidity ranges. The Et region column gives the lower thresholds on the jet transverse energy.

Figure 6.5 shows the correlation between $\langle E_T^{detector} \rangle$ and $\langle E_T^{hadron} \rangle$ matched jets in different pseudorapidity bins. The dashed line is a slope one, offset zero reference line. The solid line is the results of the linear fits.

The figure 6.6 gives the slopes and offsets distributions for different pseudorapidity bins. One can see that the fitting parameters (slope and offset) for pseudorapidity below -1 are quite different from the others. This is mainly affected by the $\eta_{jet}^{3,4,5} < -1$ cut.

5. The last step is to apply those linear functions onto data, so as to correct the data back to its hadronic final state level.

$$E_{T,jet}(corrected) = \frac{E_{T,jet}(rec) - b(\eta_{jet}, E_{T,jet}(rec))}{m(\eta_{jet}, E_{T,jet}(rec))} \tag{6.3}$$

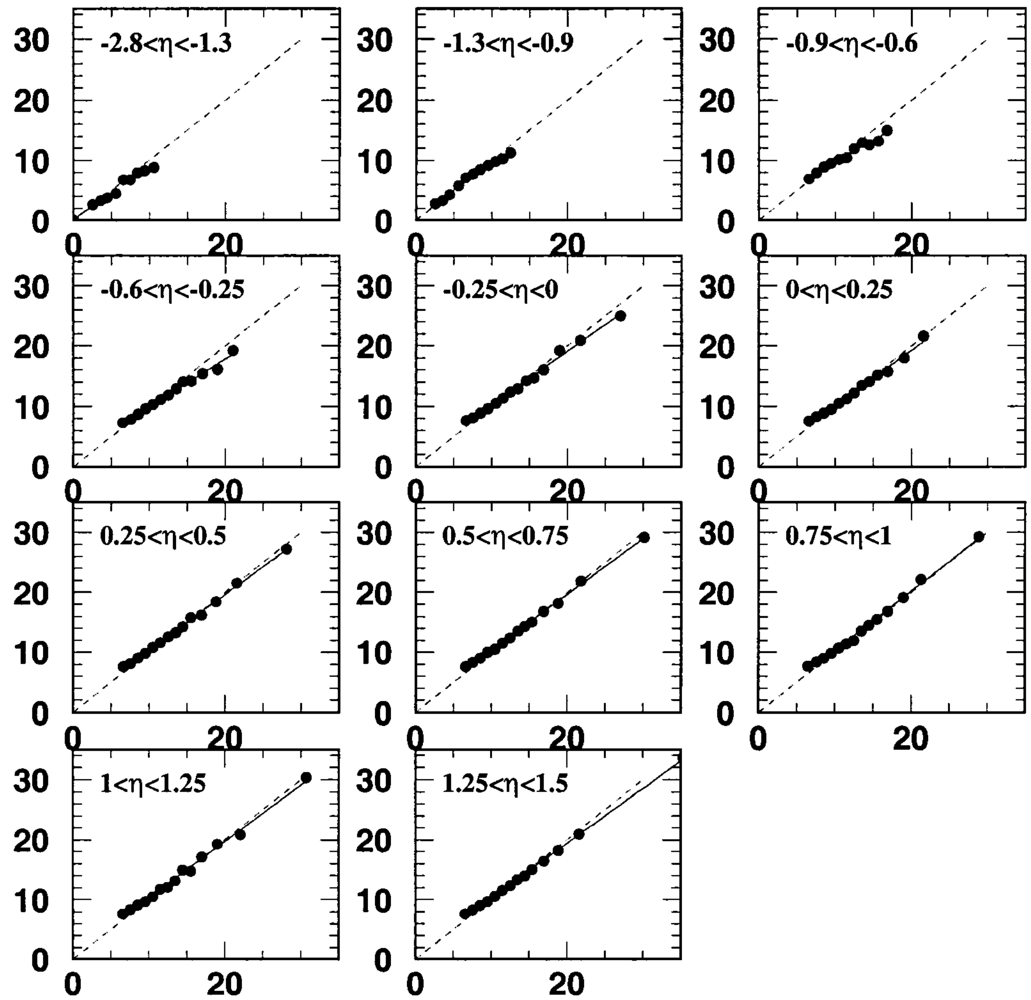

Figure 6.5: $\langle E_T^{DET} \rangle$ as a function of $\langle E_T^{HAD} \rangle$ using the matched jets in the MC sample. The solid black dots are matched correlation MC jets, with their x-coordinate being 'Hadron level', and y-coordinate 'Detector level'. The solid line is the fitted straight line to describe the dots. The dashed line is a nominal diagonal ideal reference line, where the detector values are equal to the hadron level values. It shows reasonable distributions. At low pseudorapidity ranges, only low E_T jets are observed, while at higher pseudorapidities, it is more evenly spread. Almost all dots are below or on the reference line, which, as expected, indicates that jets will generally lose some energy from hadron level to detector level.

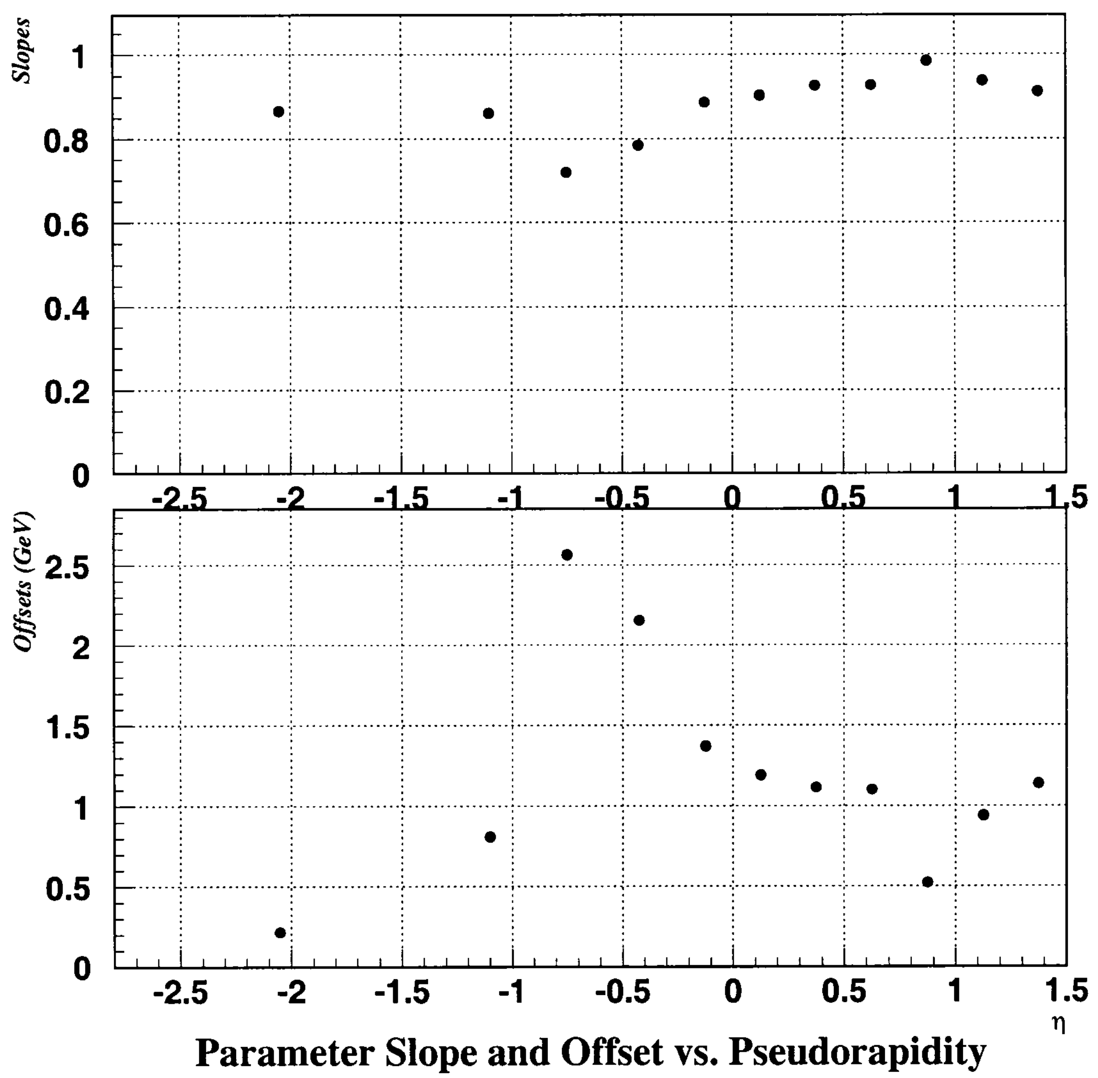

Figure 6.6: Fitted parameters m (slope) and b (offset) as function of the pseudorapidity η for HERWIG.

where the parameters b and m are the values taken from the linear fit, in the corresponding η bin, "rec" means "reconstructed".

6.2.3 Detector Efficiency, Purity and Correction Factor

To evaluate how well the corrections are performed, and to have an overview of the detector efficiency for these particular physics events, the purity of the sample selection and the efficiency of the detector can be calculated. The detector acceptance, also known as the correction factor in cross section calculations, is the ratio of the efficiency to the purity. Since no cross-section is calculated in this thesis, they are not used in the analysis, but they show levels generally above 80%.

Efficiency

The efficiency is the ratio of jets which are found at detector level to the corresponding event at hadron level in the same bin, which in another word, describe how must percent of jets is taken by the detector.

$$\varepsilon = \frac{n_{jet}^{generated\ \mathbf{AND}\ reconstructed}}{n_{jet}^{reconstructed}} \tag{6.4}$$

Purity

The purity is the ratio of the jets which are found at detector level to the corresponding jet at hadron level in the same bin.

$$P = \frac{n_{jet}^{generated\ \mathbf{AND}\ reconstructed}}{n_{jet}^{generated}} \tag{6.5}$$

Detector Acceptance

The detector effect (correction factor) can be calculated by using the detector acceptance with the help of Monte Carlo samples. It is the ratio of the jets result at hadron level over detector level, in different pseudorapidity and energy bins.

$$F_C = \frac{\langle n_{jet}\rangle|_{M.C}^{hadron}}{\langle n_{jet}\rangle|_{M.C}^{detector}} \tag{6.6}$$

The efficiency, purity and correction factor, for different pseudorapidity bins are shown in figure 6.7.

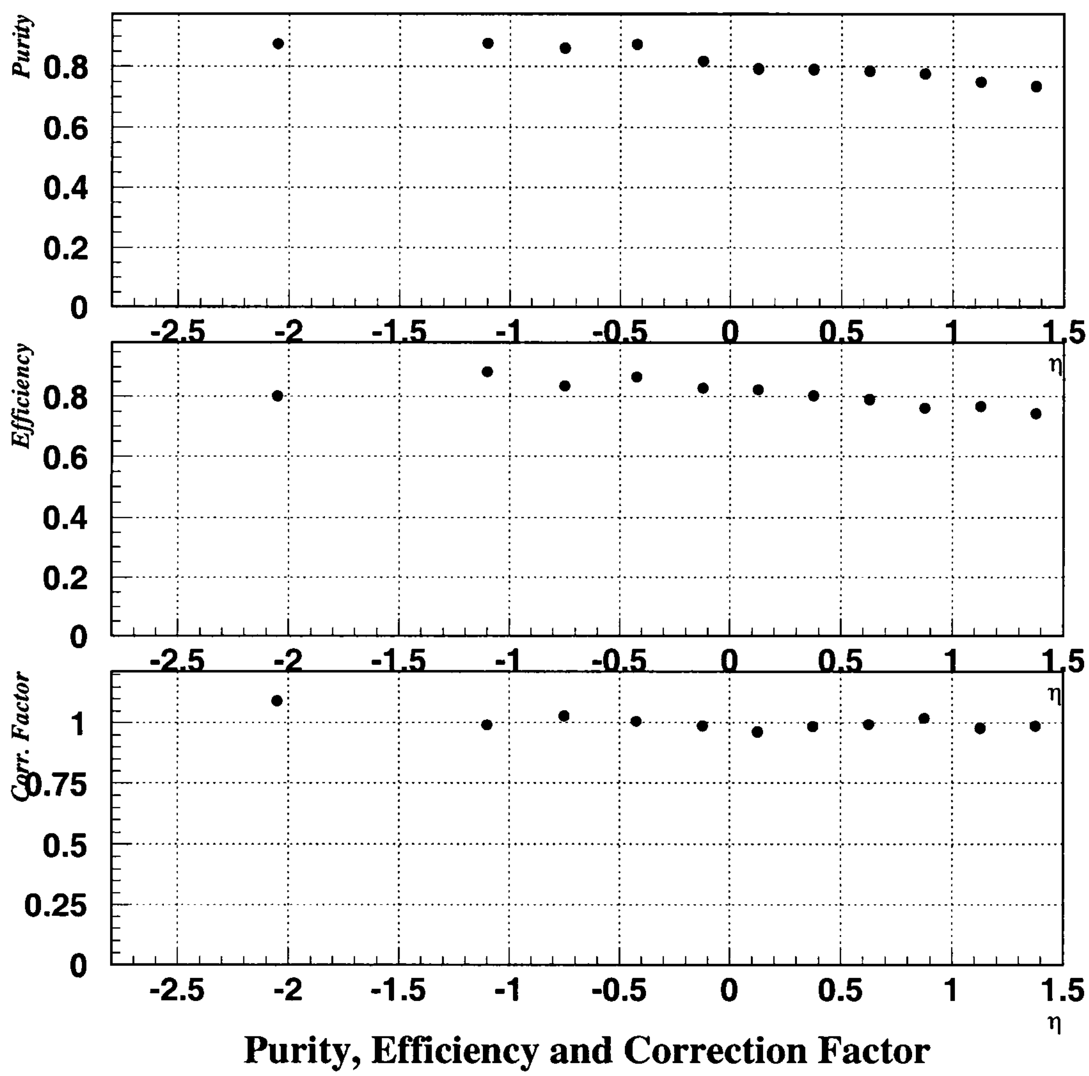

Figure 6.7: Purity, Efficiency and Correlation Factor as a function of η_{jet} using the HERWIG event samples

Chapter 7

Dijets and Photon Remnant Studies

As described in Chapter 5, the first step in this analysis was to select a sample of photoproduction events and to try to identify the photon remnant jet, which is expected to have very low transverse momentum $P_t \approx 2$ GeV [10], out of a complex background.

Properties of the selected dijet and tri-jet events were studied and compared to the HERWIG Monte Carlo predictions (see chapter 6). It should be noted here that, due to the small statistics of the four-and five-jet event sample compared to two-and three-jet event samples, the photon remnant candidate is always assumed to be the third highest transverse energy jet.

The sorting of all the jets in the event is according to their transverse energy from the highest to the lowest, which means that the numbering of the jets is directly related to their transverse energies. The number one and number two jets, which are also called *jet1* and *jet2*, are regarded as the parton jets, while the third jet (*jet3*) is thus assumed to be the photon remnant jet. One would ask if it is possible that one of the *jet1* and *jet2* would actually be a photon remnant jet, but mistakenly identified as a parton jet, only because that it is slightly higher in transverse energy than the actual parton jet.

To evaluate which fraction of the *jet3* has transverse energies closed to that of *jet1* and *jet2*, the ratio E_T^3/E_T^1 and E_T^2/E_T^1 are calculated and plotted in figure 7.1. It clearly shows that a very small part of distribution is close to one, which means that there is only very few percents (0.0021% and 0.0875%, respectively, for ratios over 0.9 in DATA) of *jet3* that have transverse energy close to *jet1* and *jet2*. As the parton jets go toward the forward direction, while the photon remnant backward, the pseudorapidity gaps between *jet1*, *jet2* and *jet3*, which are symbolized as $\eta(2) - \eta(3)$ and $\eta(1) - \eta(3)$ in figure 7.1, should not be very close to zero. One can see that it is really the case in the histograms with mostly at least one unit of difference.

To further clear this issue out, the correlation between the transverse energy ratios and the pseudorapidity gaps are shown in the scatter plots in figure 7.1 both for DATA and MC. One can see that in those 'dangerous' regions (the left-up region in the plot), where the E_T ratio is close to one and the pseudorapidity gap is close to one, there are very few percents (0% and 0.0085%, respectively, for the E_T ratios over 0.9 and the pseudorapidity gap within 0.5) of event left both for *jet3* with respect to *jet1* and *jet2*. So basically we can conclude safely that the two parton jets candidates and the photon remnant jet candidate are well selected by their transverse energies. It can be recalled that the two parton jets candidate were also nicely back-to-back in the X-Y plane (see section 5.5), which is in good agreement with the transverse momentum conservation.

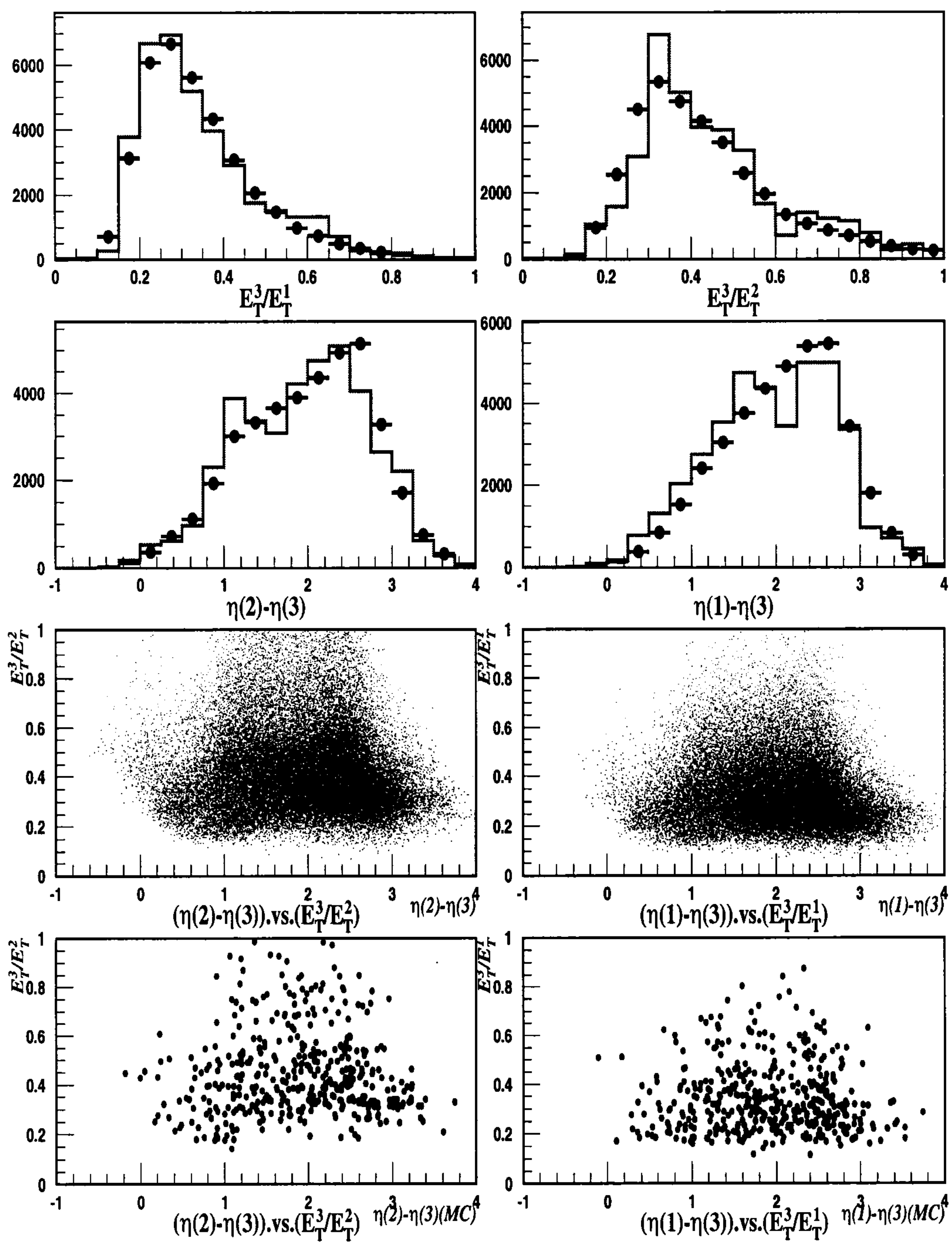

Figure 7.1: The four histograms on the top show the E_t ratios and pseudorapidity gaps of *jet3* with respect to *jet1* and *jet2*, with dots as DATA and lines as MC. The lower four scattered plots show the correlated E_T ratio vs the pseudorapidity gap, with two plots for DATA and two plots for MC (bottom).

7.1 Transverse Energy Correction

The detector level transverse energy of the jets was corrected back to the hadronic final state level, in different pseudorapidity ranges, as described in chapter 6. The detailed procedure on how the correction factors are calculated and thus applied to the detector data is described in section 6.2.2. The result of the transverse energy distribution for *jet1* through *jet5* is shown in the figure 7.2.

One can see that the corrected jet transverse energies (dashed lines) are higher than the detector level jet transverse energies by 10.3% in average. This is the result of detector effects, such as particle energy loses in 'dead' materials, such as the tracking detectors which are enclosed by the calorimeters. Other issues, such as detector acceptance (see section 6.2.3) and resolution limitations, also contribute to the energy difference.

7.2 Photon Remnant Identification and Properties

The main task of this analysis is to successfully isolate the photon remnants in the multi-jet photoproduction. Photon remnants are expected to be isolated by requiring low transverse energies, and the pseudorapidity distribution should be located in the backward region $\eta_{jet}^{Photon\ Remnant\ Candidate} < -1$ [48]. After the application of the selection cuts, the pseudorapidity distributions are shown in figure 7.3.

As described in section 2.7.4, jet transverse energy density, which is known as the jet shape $\psi(r)$, can give insight information on the internal jet structure. According to the QCD theory and jet kinematics, a photon remnant jet is expected to be broader than parton jets [49]. So it might reversely provide a way to identify the photon remnant jet by its jet shape behavior, or at least assign a probability to it.

It should be noted that *jet3* is always assumed to be the photon remnant jet can-

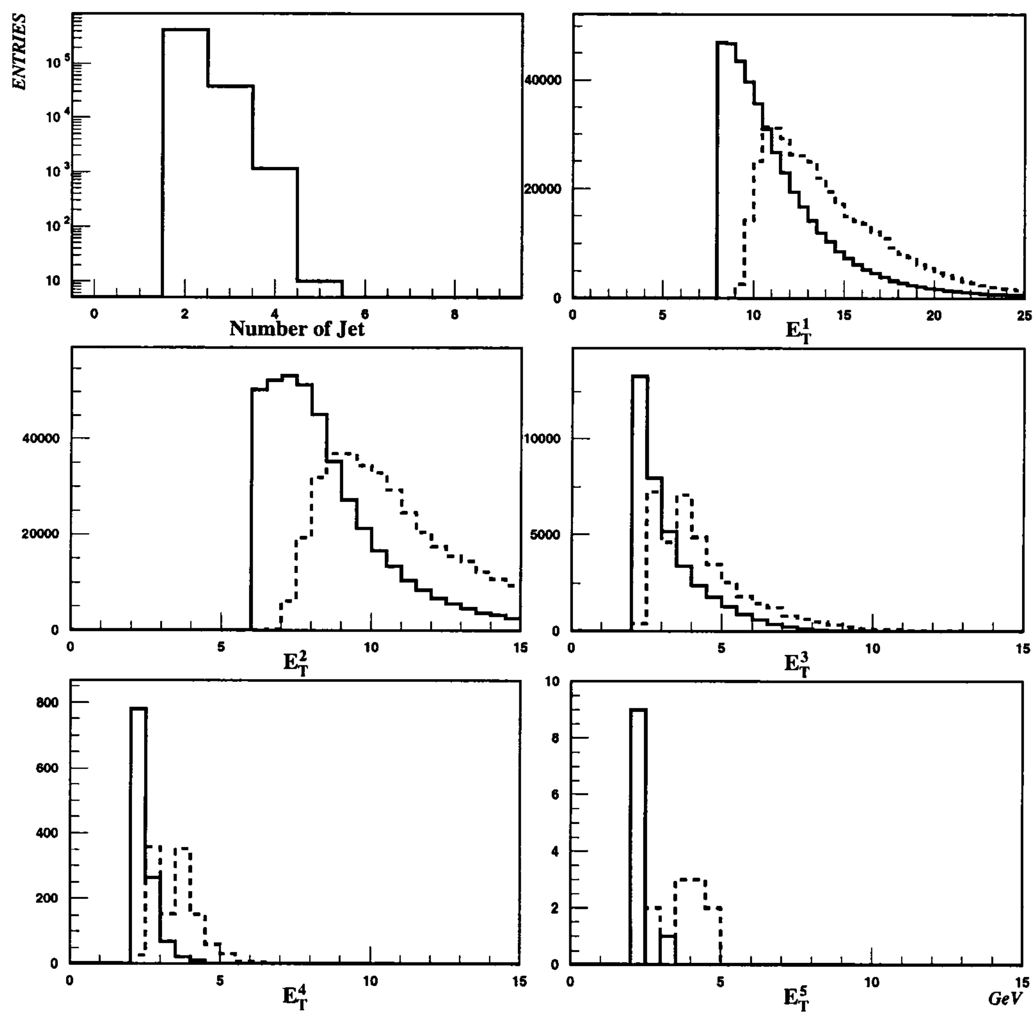

Figure 7.2: The DATA transverse energy distributions after correction. The 'Number of Jet' plot shows the overall distribution of the events. The E_T^1, E_T^2, E_T^3, E_T^4, E_T^5 are the transverse energy distribution of the jets, sorted by their transverse energies. Solid lines are the uncorrected DATA, while dashed lines are the corrected transverse energy distribution.

didate throughout this analysis. The *jet4*, *jet5*, etc. are discarded due to their low numbers and small E_T's, which can not provide very convincing information.

The final result of the average three-jet event jet shape distribution is presented in figure 7.4 both for DATA and MC. The *jet1* and *jet2* are the two highest E_T jets for

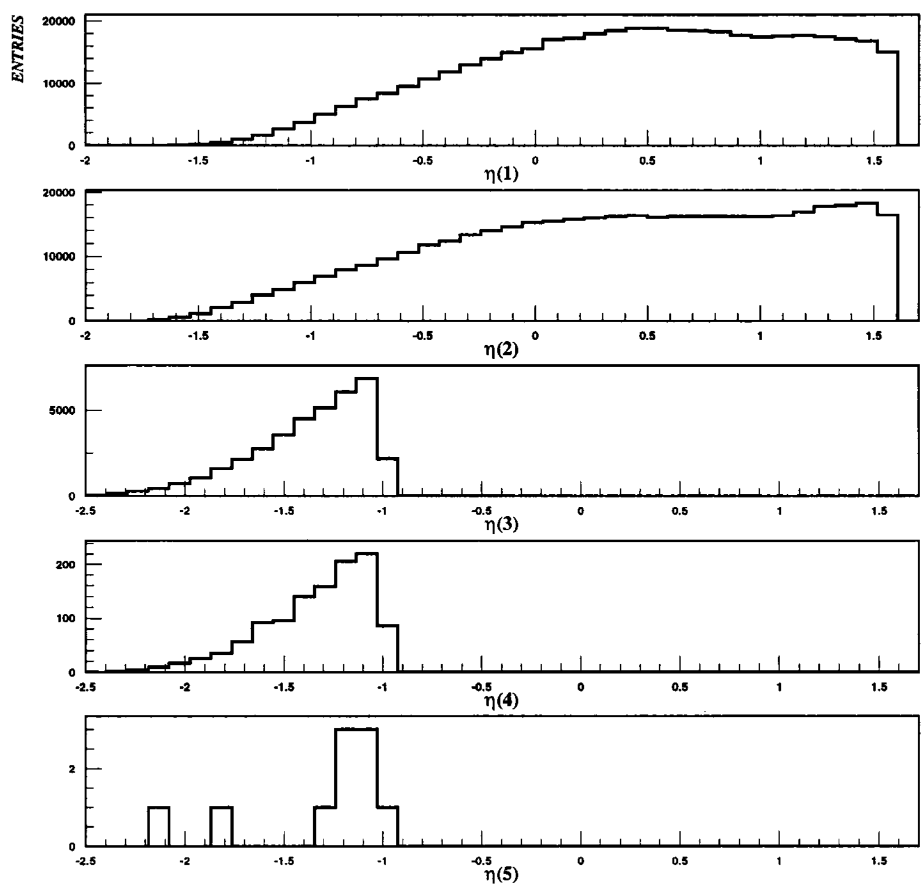

Figure 7.3: Pseudorapidity distribution. The pseudorapidity distribution of the *jet1, jet2, jet3, jet4, and jet5.* The first three plots are the dots in figure 5.4.

all events, while *jet3* is the third jet in all three and more jets events. The curves are spline curves on the eleven points. The solid dots represent data samples, while the hollow dots are for Monte Carlo. The dashed curves are the fits for the *jet3.* As the ψ variable describes the internal E_T densities of a jet, one can read this plots as follows: For any given radius, there are six points from the six curves, and the ones giving lower ψ values are actually 'broader' jets. This is because the lower energy density at same radius indicates that there is more E_T located outside of this radius, and thus it is 'broader'. One can see that the *jet1* and *jet2* distributions are very close to and even overlapping each other, and that the error bars cover each other also. This means that the ψ jet shape cannot be used to distinguish between the first two parton jets. Indeed, they are expected to be identical. But it clearly shows that the third jet, which is expected to be the photon remnant candidate, lies lower, for both DATA and MC, and its error bars do not cover *jet1*, nor *jet2*. This indicates that it has broader internal structure than the other two parton jets. A significant disagreement still exists between DATA and MC, and the data jets have broader structures than MC jets. This is mainly due to the detector (mostly CAL and CTD) resolution limitations. For example in CAL, one or a bunch of trans-passing particles can shower in the CAL and a jet is formed and detected by CAL cells. But the showering process may excite a wide range of neighboring CAL cells, as the cell is not ideally small enough, and the geometry limitations can cause this smearing effect. So the jet signals collected by the detector are broader than for the MC jets. The discrepancies can also be due to the poor Monte Carlo representation for the calorimeter. This behavior has also been observed in another analysis, which will be introduced below:

Another analysis ([17]) on the jet shape measurement in photoproduction will be compared with. This analysis was performed in the center-of-mass range of 134 - 277 GeV with the 1994 ZEUS data (E_p = 820 GeV). The jets were identified using a CONE algorithm in the $\eta - \phi$ plane with a cone radius of one unit. The inclusive dijet samples required transverse energies over 14 GeV. The PYTHIA Monte Carlo event simulator was used with the cut on the minimum E_T at 1.0 GeV, and the P_T of the two parton jets above 8 GeV.

Figure 7.5 is a plot taken from [17]. It shows the jet shape distributions for different η regions. The photon remnant jet should be included in the resolved processes, while only the parton jets are considered in the direct processes. One can tell from figure 7.5 that the resolved jet shape curves lie lower than the direct ones in all pseudorapidity ranges. This indicates that the jet shapes including the photon remnant jet are broader than without the photon remnant jet, which is in good agreement with the observed behaviors in figure 7.4. Another agreement between the two analyses is that the jet shapes measured from the DATA, especially at high η values, are broader than what are measured from the Monte Carlo (Resolved + Direct) in figure 7.5.

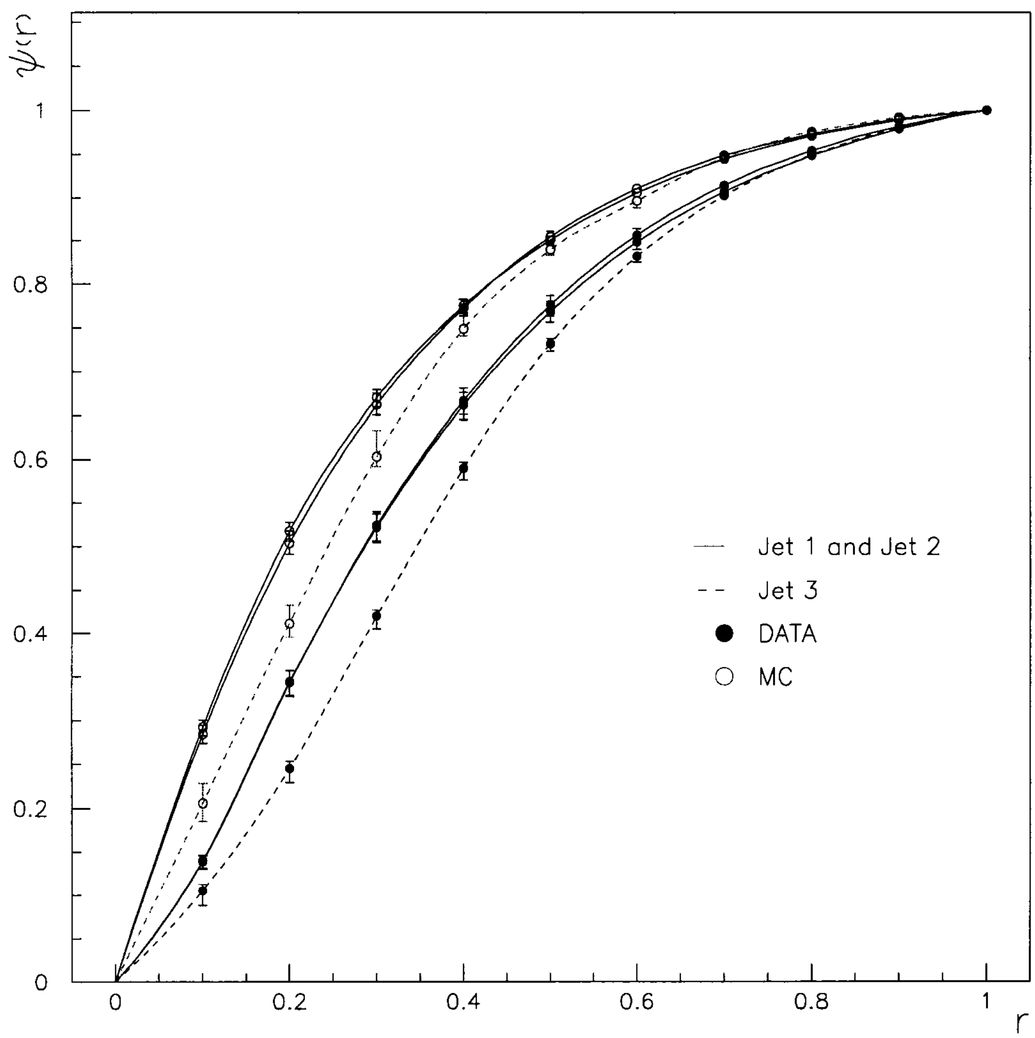

Figure 7.4: Jet shape $\psi(r)$ distribution. The X axis is radius variable from 0 to 1 unit. The Y axis is ψ, which is also from 0 to 1, and gives the average transverse energy density distribution inside a jet.

But the difference is much more obvious in figure 7.4, and this might indicate that the HERWIG Monte Carlo generator can not describe the DATA well in this case as the PYTHIA generator. The exact differences have not been investigated in this work.

Figure 7.6 is created by scaling the *jet1* and *jet2* from figure 7.4 of DATA and MC. After the two highest E_T jets are scaled together, one can compare the third jet

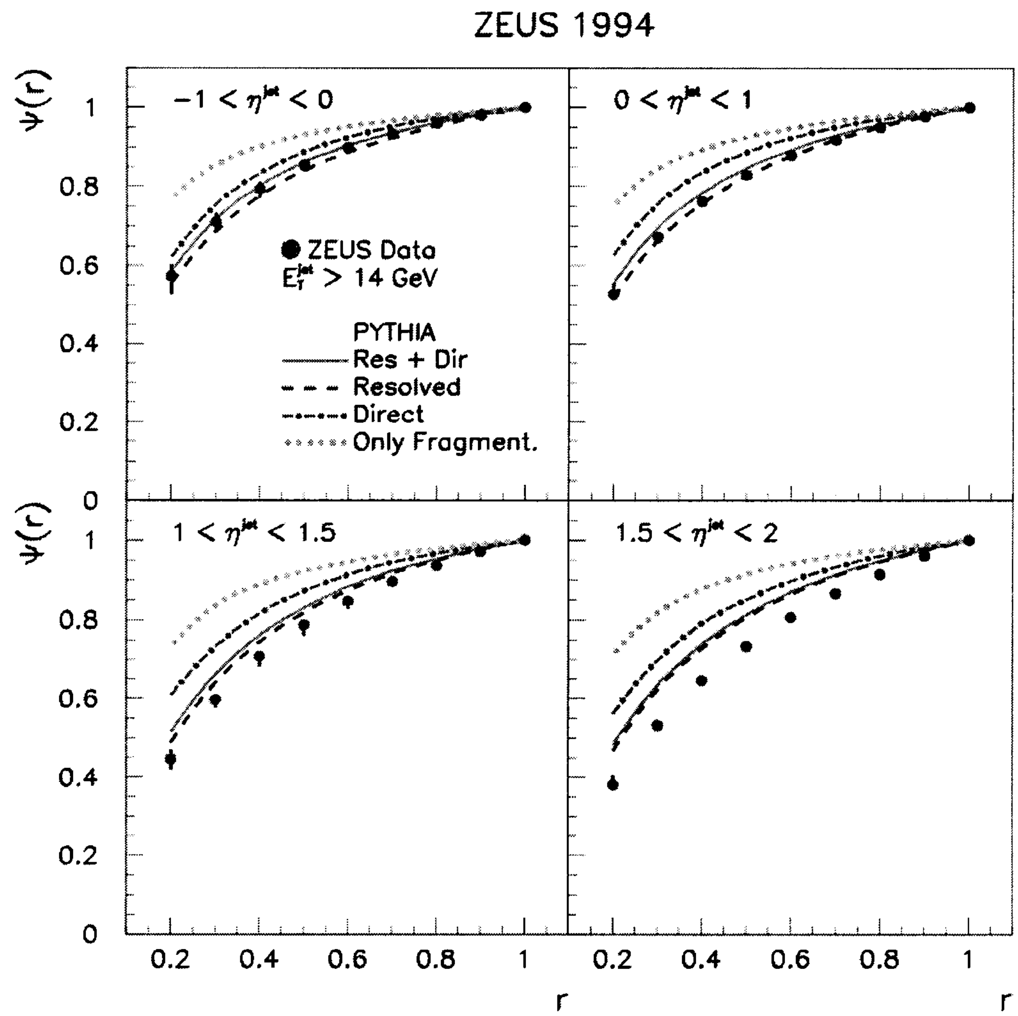

Figure 7.5: The jet shape measurement [17] is performed on jets in the E_T range above 14 GeV in different η regions. The error bars show both the statistical and systematic errors. The PYTHIA Monte Carlo simulates both resolved and direct photoproduction processes. The predictions of PYTHIA for resolved plus direct processes without initial and final state parton radiation are included and labelled as 'Only Fragmentation'.

between DATA and MC better. It can be seen that once the MC inadequacies are taken out, the agreement between DATA and MC for the third jet after the scaling is excellent, thus supporting the limitation assumption on the MC representation.

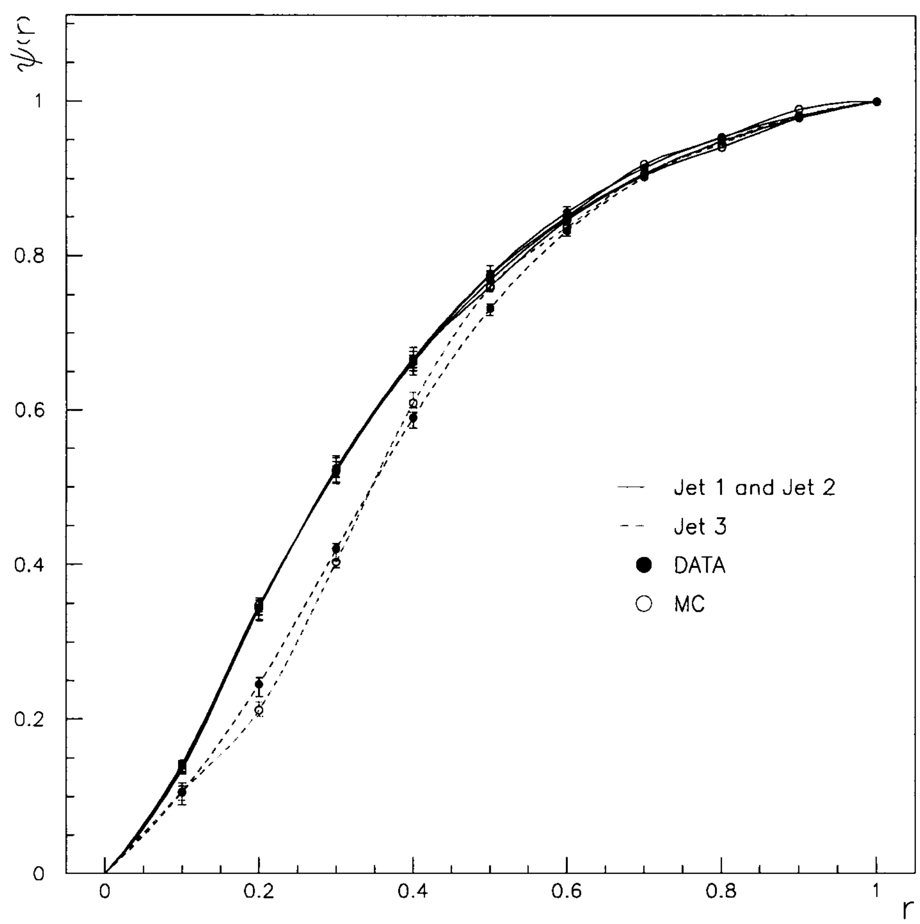

Figure 7.6: The scaled jet shape $\psi(r)$ distribution from figure 7.4. The X axis is radius variable from 0 to 1 unit. The Y axis is ψ, which is also from 0 to 1, and gives the average transverse energy density distribution inside a jet.

7.2.1 Uncertainty Estimations

To evaluate how accurate the jet shape information can be, the statistical and systematic uncertainties (error bars) shown in figure 7.4 were calculated as follows:

Statistical Uncertainties

The statistical uncertainties are calculated through the number of jets in each bin with the formula $\sigma_{statistical} = \frac{1}{\sqrt{N_{bin}}}$ which is derived from a Poisson distribution. So in the case of ψ, all shape points along the spline curve have the same numbers of entries behind them, which are the numbers of jets. The number of jets are: 893065 (2×427738+37589) for all first two jets, and 37589 for the third jets. So the relative statistical errors for two jets and for the third jets are 0.11% and 0.52%, respectively. They are essentially negligible compared to the systematic errors.

Systematic Uncertainties

The systematic uncertainties are calculated with the variation of the selection cuts. Those cuts include event selection and jet selection cuts, which have been carefully described in chapter 5. A rough estimation of these variations was obtained from studies of the type presented in figures 5.3 and 5.4. Although the studies were not extensive, they are believed to yield fair estimates of possible parameter variations to adequately represent most of the data over the whole kinematic range. So basically, the jet shape is calculated repeatedly, by the procedure illustrated in figure 2.6, with different cuts setups. The variation of each of the different results is then used to determine the size of the systematic errors. The nominal values and the varied values of the cuts are listed in table 7.1. The choices of the variation sizes are based on [10], or the resolution of the measurement variables.

After the repeated analysis done on the eighteen different cuts, the systematic fluctuations in the measurement of $< \psi >$ on *jet1*, *jet2* and *jet3* are given in figure 7.7 for DATA, and figure 7.8 for MC. *jet1*, *jet2* and *jet3* are separately shown in three rows, and in row, nine bins are divided for r from 0.1 to 0.9. In each bin, the 18 fluctuations from nominal are measured in percents, and from left to right, the 18 points are listed in table 7.1. One can see that errors tend to be larger in low radius regions. They are close to zero for radii close to one, since there ψ gets less sensitive anyway. More significant fluctuations are observed on point number 9, 10, 11, 12, 15 and 16. Points from 9 through 12 are the derivation cut on the first

No.	Relaxed Values	Nominal Values	No.	Tightened Values		Units
1	$0.15 < y_{JB} < 0.9$	$0.2 < y_{JB} < 0.85$	2	$0.25 < y_{JB} < 0.8$		
3	$Z_{vertex} < 80$	$Z_{vertex} < 60$	4	$Z_{vertex} < 40$		cm
5	$y_e(sinistra) > 0.7$	$y_e(sinistra) > 0.75$	6	$y_e(sinistra) > 0.8$		
7	$P_T/\sqrt{E_T} < 1.8$	$P_T/\sqrt{E_T} < 1.5$	8	$P_T/\sqrt{E_T} < 1.2$		$\sqrt{GeV}$
10	$E_T^1 > 7.5$	$E_T^1 > 8$	9	$E_T^1 > 8.5$		GeV
12	$E_T^2 > 5.5$	$E_T^2 > 6$	11	$E_T^2 > 6.5$		GeV
14	$E_T^3 > 1.8$	$E_T^3 > 2$	13	$E_T^3 > 2.2$		GeV
15	$\eta < 1.8$	$\eta < 1.6$	16	$\eta < 1.4$		GeV
18	$\eta_3 < -0.8$	$\eta_3 < -1.0$	17	$\eta_3 < -1.2$		GeV

Table 7.1: List of systematic checks included in the calculation of the systematic error bars. The No. refers to the points in figure 7.7 and 7.8.

two jets' E_T. Larger errors show that the E_T cut is critical to select hard scattering events from soft ones. Points 15 and 16 are the cuts on the pseudorapidities of all jets.

The systematic error for each r-bin would be calculated from all available points with the formula 7.1:

$$\sigma_{sys} = \sqrt{\Sigma_{i=1}(d_i - d_0)^2} \tag{7.1}$$

where $d_i - d_0$ is the relative error for each systematic point, from the nominal (d_0).

It should be noted that, since in formula 7.1, the square calculation of $(d_i - d_0)^2$ would cancel the sign of $(d_i - d_0)$, which means that the positive and negative errors would not be distinguishable. But in this analysis, positive and negative errors from the 18 points are summed up separately. There will be two systematic error bars assigned to each $\psi(r)$ as error-up (positive) and error-down (negative). This is also reflected in figure 7.4 when they are added up in quadrature with the statistical errors.

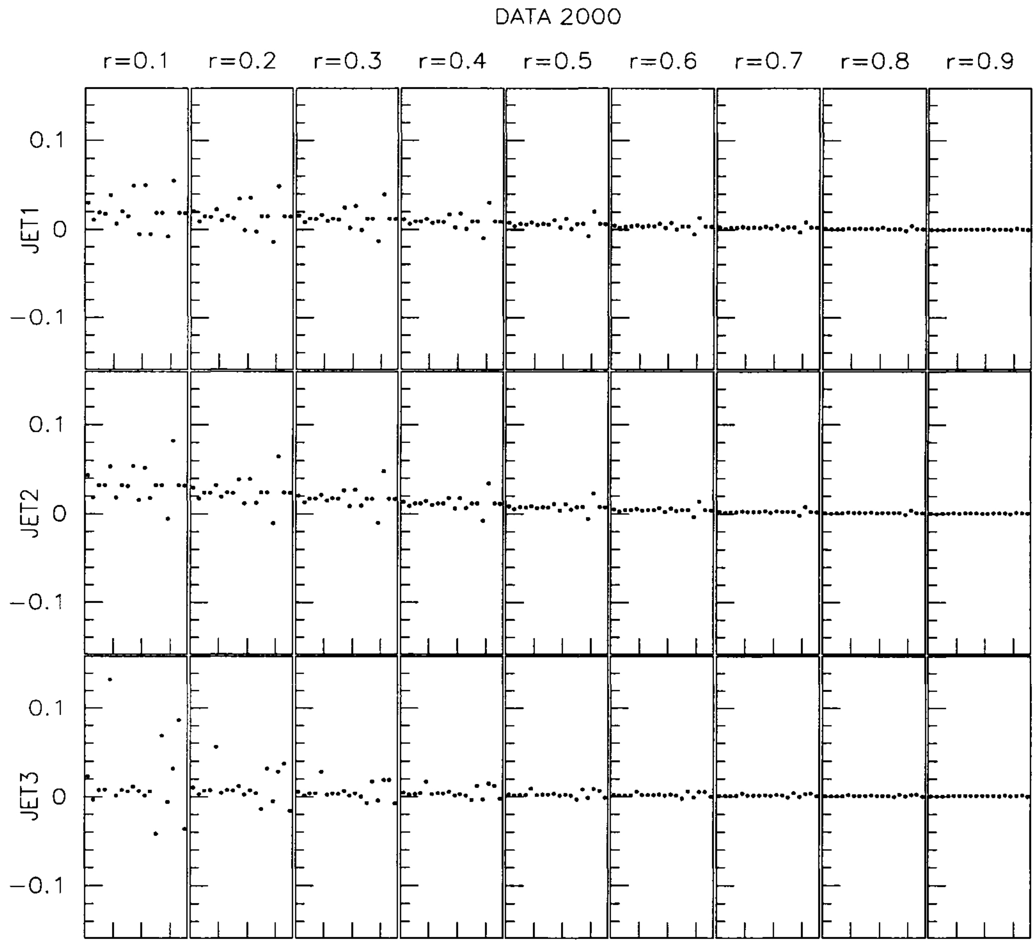

Figure 7.7: The relative effect of various systematic variations in the calculation of ψ for r from 0.1 to 0.9. (DATA)

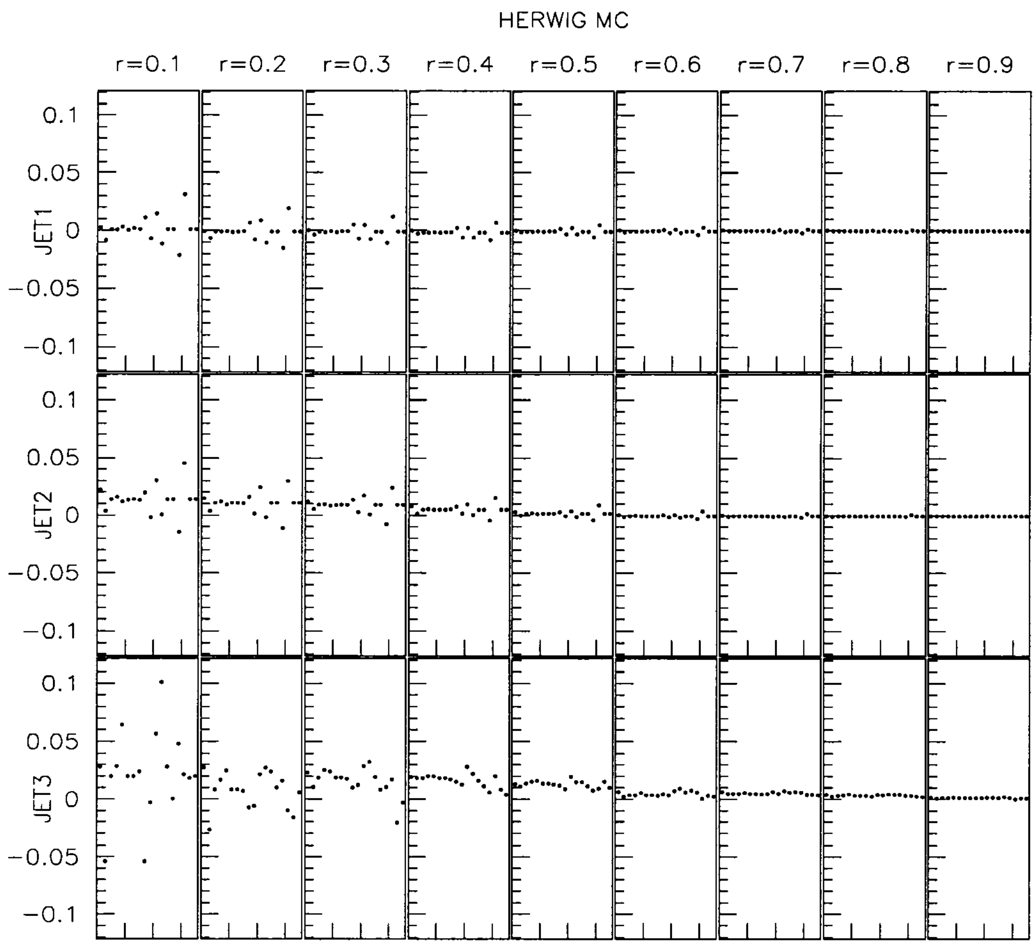

Figure 7.8: The relative effect of various systematic variations in the calculation of ψ for r from 0.1 to 0.9. (MC)

Chapter 8

Conclusion and Outlook

From the year 2000, 27.5 GeV positrons and 920 GeV proton collision data sample, jet reconstruction is performed with the k_T algorithm in the laboratory frame. Physics events with two or more jets are selected, with the requirement that all jet E_T's should be greater than 2 GeV, and their $\eta < 1.6$. With the help of the leading order HERWIG Monte Carlo simulation for comparisons, events are furthermore selected by applying cuts on the kinematic variables where the detector is fully understood. A dedicated cut, requiring that $E_T^1 > 8$ GeV, $E_T^2 > 6$ GeV, and $\eta^3 < -1$, removes more background jets or proton remnant jets contained inside the third jets, due to low E_T cut of the latter. With the HERWIG Monte Carlo simulation, the detector level jet energies on DATA are corrected back to their hadron level, compensating the detector effect and the energy lose. The jet shape variable $\psi(r)$ is constructed for each jet. It distinguishes, through inner transverse energy density, between parton initiated jets and photon remnant jets. The result, showing that photon remnant jets have broader jet shape than parton jets, is in good agreement with the QCD theoretical expectation.

By increasing the statistics, studies on the *jet4, jet5...* and their understanding would be much improved. Cutting at very low x_γ would furthermore purify the photon remnant jet selection. The jet background in the rear direction is however one of the main limitations of this type of analysis, which the improvements in statistics would not fix. Similar experiments like photo-photon collisions at LEP also provide information on the photon structure. The results from the two experiments could be compared. They were however beyond the scope of this work. More detailed jet shape studies on the quark originated jets and the gluon originated jets would be also an interesting topic.

Chapter 9

Acknowledgements

I would like to thank my supervisor François Corriveau, for providing the valuable opportunity to work in ZEUS, to explore the unknown of physics, for his kind help and instructions in my work and analysis. Many thanks should go to Mauricio Barbi, who got me started in ZEUS when I arrived, guided me to the right direction. I would also like to thank Roberval Walsh for the help on my analysis, thesis writing and Claudia Glasman for some helpful tips.

Chapter 10

Glossary

BCAL Barrel Calorimeter

CAL ZEUS main uranium calorimeter

CTD ZEUS Central Tracking Detector

DESY Deutsches Elektronen - Synchrotron

DIS Deep Inelastic Scattering

EMC Electromagnetic section of the CAL

FCAL Forward Calorimeter

FLT First Level Trigger

GeV Giga-electron-Volts

GFLT Global First Level Trigger

HAC Hadronic section of the CAL

HERA Hadron Electron Ring Anlage

HES Hadron Electron Separator in CAL

LO Leading Order

LUMI Luminosity Detector

MC Monte Carlo

NC DIS Neutral Current Deep Inelastic Scattering

CC DIS Charge Current Deep Inelastic Scattering

NLO Next-to-Leading-Order

PMT Photomultiplier Tube

QCD Quantum Chromodynamics

QED Quantum Electrodynamics

RCAL Rear Calorimeter

SLT Second Level Trigger

TLT Third Level Trigger

ZUFO ZEUS Unidentified Flow Objects, combined information both from tracking and calorimeter

Bibliography

[1] *Advanced Series on Directions in High Energy Physics* - Vol. 5. *Perturbative QCD*, Author: A. H. Mueller (Columbia), Published: Jul 1989. World Scientific Publishing Company.

[2] *Successive combination jet algorithm for hadron collisions* S.D. Ellis and D.E. Soper, Phys. Rev. D 48 (1993) 3160.

[3] *Dijet Cross Sections in Photoproduction at HERA*. ZEUS Collaboration, M. Derrick *et al.*, Phys.Lett. B 348. (1995) 665.

[4] B.R. Webber, *A QCD model for jet fragmentation including soft gluon interference*, Nucl. Phy. B. 238 (1984) 492.

[5] *Parton Fragmentation and String Dynamics*, B. Anderson *et al.*, Phys. Rep. 97 (1983) 31.

[6] *Jets in Photoproduction at HERA*. Dissertation for Doctor's degree. Sascha Caron, RWTH Aachen, 2002.

[7] *Measurement of Dijet Production in Neutral Current Deep Inelastic Scattering at High Q^2 and Determination of α_s*, ZEUS collaboration, J. Breitweg *et al.*, Phys Lett B 507 (2001) 70.

[8] *Rapidity Gaps Between Jets in Photoproduction at HERA*, ZEUS Collaboration, M. Derrick *et al.*, Phys. Lett. B 369, 55 (1996).

[9] D. E. Soper and J. C. Collins, *Issues in the determination of parton distribution functions,* CTEQ-NOTE-94-01, Nov 1994. 15pp. , arXiv:hep-ph/9411214.

[10] *Study of the Photon Remnant in Resolved Photoproduction at HERA.* B.H. Behrens (Wisconsin University), Ph.D. Thesis, DESY F35D-95-11, 1995.

[11] *Photon-hadron Interactions*, by R.P. Feynman, (1972), Publisher: Benjamin. Address: New York.

[12] *Measurement of the subjet multiplicity in neutral current deep inelastic scattering and determination of* α_s, O. González, J. Terrón, *et al.* [ZEUS Collaboration] Phys.Lett. B558 (2003) 41-58.

[13] *Jet Algorithms*, Sergei Chekanov, 14th Topical Conference on Hadron Collider Physics. 28 Sep. - 4 Oct. 2002.

[14] S. Ellis, D. Soper, *Successive combination jet algorithm for hadron collisions.* Phys. Rev. D 48 (1993) 3160.

[15] A. Hebecker, *Diffraction in deep inelastic scattering.* Phys. Rept. 331, 1 (2000) [arXiv:hep-ph/9905226].

[16] J. Breitweg *et al.* [ZEUS Collaboration], *Measurement of jet shapes in high-*Q^2 *deep inelastic scattering at HERA,* Eur. Phys. J. C 8, 367 (1999) [arXiv:hep-ex/9804001].

[17] J. Breitweg *et al.* [ZEUS Collaboration], *Measurement of jet shapes in photoproduction at HERA,* Eur. Phys. J. C 2, 61 (1998) [arXiv:hep-ex/9710002].

[18] J. Breitweg *et al.* [ZEUS Collaboration], *Measurement of dijet photoproduction at high transverse energies at HERA,* Eur. Phys. J. C 11, 35 (1999) [arXiv:hep-ex/9905046].

[19] J. Breitweg *et al.* [ZEUS Collaboration], *Dijet cross sections in photoproduction at HERA,* Eur. Phys. J. C 1, 109 (1998) [arXiv:hep-ex/9710018].

[20] C. Friberg and T. Sjostrand, *Jet production by virtual photons,* Eur. Phys. J. C 13, 151 (2000) [arXiv:hep-ph/9907245].

[21] M. Derrick *et al.* [ZEUS Collaboration], *Dijet Angular Distributions in Direct and Resolved Photoproduction at HERA,* Phys. Lett. B 384, 401 (1996) [arXiv:hep-ex/9605009].

[22] C. F. Berger *et al., Snowmass 2001: Jet energy flow project,* in *Proc. of the APS/DPF/DPB Summer Study on the Future of Particle Physics (Snowmass 2001)* ed. N. Graf, C010630, P512 (2001) [arXiv:hep-ph/0202207].

[23] S.D. Ellis and D.E. Soper, *Successive combination jet algorithm for hadron collisions,* Phys. Rev. D 48, 3160 (1993) [arXiv:hep-ph/9305266].

[24] M. Derrick *et al., Design and Construction of the ZEUS Barrel Calorimeter,* Nucl. Instr. and Meth., A (309): 77, 1991.

[25] W.H. Smith et al. *The ZEUS Calorimeter First Level Trigger,* Nucl. Instrum. Meth A355: 278, 1995.

[26] *ZEUS A Detector For HERA,* Bluebook, ZEUS collaboration, 1993.

[27] *On the Stopping of Fast Particles and on the Creation of Positive Electrons,* H. Bethe and W. Heitler, Proc. Roy. Soc. A 146 83(1934).

[28] The ZEUS offline analysis webpage:
`http://www-zeus.desy.de/components/offline/offline.html`
The ZEUS ORANGE webpage:
`http://www-zeus.desy.de/ZEUS_ONLY/analysis/orange/`

[29] *Precise determinations of the strong coupling constant at HERA.* Oscar Gonzalez Lopez (University Autonoma de Madrid), Doctor degree thesis, 2002.

[30] *General Overview of the ZEUS Calorimeter.* P.R.B. Saull. DESY report. January, 1998.

[31] *Calibration and monitoring of the ZEUS uranium scintillator calorimeter at HERA.* M. Barbi. The ZEUS Calorimeter Group, CALOR2002 paper, Beckman Institute, Caltech.

[32] *Longitudinal Positron Polarisation in HERA-II.* The HERA team, Proceedings of EPAC 2004, Lucerne, Switzerland.

[33] V. D. Barger, K. M. Cheung, K. Hagiwara and D. Zeppenfeld, *Global study of electron quark contact interactions,* Phys. Rev. D 57, 391 (1998) [arXiv:hep-ph/9707412].

[34] *The silicon strip detectors of the ZEUS microvertex detector*, Doctor Thesis, DESY-thesis-99-027, Dominik Dannheim (University of Hamburg), 1999.

[35] *First Measurements of HERA Luminosity by ZEUS Lumi Monitor, J. Andruszkow, et al.*,Preprint DESY-92-066, DESY, 1992.

[36] *Dijet Photoproduction at High Transverse Energies with the ZEUS Detector at HERA.* A. H. Ochs, Department of Physics, McGill University, Montreal, DESY - THESIS - 2003 - 005.

[37] *Vertex Triggering Using Time Difference Measurements in the ZEUS Central Tracking Detector*, N. Harnew, *et al.*, Nucl. Instrum. Methods A 279 (1989) 290.

[38] Niels Tuning, *ZUFOs: Hadronic final state reconstruction with calorimeter, tracking and backsplash correction*, ZEUS-01-021, June, 2001.

[39] *Les Houches guidebook to Monte Carlo generators for hadron collider physics.* M. A. Dobbs *et al.* FERMILAB-CONF-04-183-T, Mar 2004. [hep-ph/0403045]

[40] *HERWIG 6.5*, G. Corcella, I.G. Knowles, G. Marchesini, S. Moretti, K. Odagiri, P. Richardson, M.H. Seymour and B.R. Webber, JHEP 0101 (2001) 010 [hep-ph/0011363]; hep-ph/0210213.

[41] *An Approach to a Structure of the Virtual Photon using Dijet Events at HERA.* Doctor Dissertation, Harald Labes, University of Hamburg, 2003.

[42] *Isolated tau leptons in events with large missing transverse momentum at HERA.* B. Foster, et al., ZEUS Collaboration, Nucl. Phys. B (Proc. Suppl.) 32 (1993) 181.

[43] S. Frixione, M. L. Mangano, P. Nason and G. Ridolfi, *Improving the Weizsacker-Williams approximation in electron - proton collisions,* Phys. Lett. B 319, 339 (1993) [arXiv:hep-ph/9310350].

[44] F.Jacquet and A.Blondel, *Proc. of the Study for an ep Facility for Europe*, ed. U. Amaldi, DESY 79/48 (1979) 391.

[45] V.M. Budnev, I.F. Ginzburg, G.V. Meledin and V.G. Serbo, *The Two Photon Particle Production Mechanism. Physical Problems. Applications. Equivalent Photon Approximation*, Phys. Rept. 15 (1974) 181.

[46] R. Brun, F. Bruyant, M. Maire, A.C. McPherson and P. Zanarini, *GEANT3*, CERN-DD/EE/84-1, 1987.

[47] *The ZEUS Background Radiation Monitor.* W. Schott et al.,ZEUS Note 93-002 (1993).

[48] R. M. Godbole, *Resolved Photon Processes*, Pramana 51, 217 (1998) [arXiv:hep-ph/9807402].

[49] T. Kluge, *Measurements of event and jet shapes at HERA*, Eur. Phys. J. C 33, S416 (2004) [arXiv:hep-ex/0310063].